



THOMAS C. TAUCHER, BSc.

MODELING X-RAY PHOTOELECTRON SPECTRA USING
DENSITY FUNCTIONAL THEORY

MASTER'S THESIS

to achieve the university degree of
Diplom-Ingenieur

Master's degree programme:
Technical Physics

submitted to:
GRAZ UNIVERSITY OF TECHNOLOGY

SUPERVISOR:
Ao.Univ.-Prof. Dipl.-Ing. Dr.techn. Egbert Zojer
Institute of Solid State Physics

Graz, November 2016

AFFIDAVIT

I declare that I have authored this thesis independently, that I have not used other than the declared sources/resources, and that I have explicitly indicated all material which has been quoted either literally or by content from the sources used. The text document uploaded to TUGRAZonline is identical to the present master's thesis.

Date

Signature

EIDESSTATTLICHE ERKLÄRUNG

Ich erkläre an Eides statt, dass ich die vorliegende Arbeit selbstständig verfasst, andere als die angegebenen Quellen/Hilfsmittel nicht benutzt, und die den benutzten Quellen wörtlich und inhaltlich entnommenen Stellen als solche kenntlich gemacht habe. Das in TUGRAZonline hochgeladene Textdokument ist mit der vorliegenden Masterarbeit identisch.

Datum

Unterschrift

Nature isn't classical, dammit, and if you want to make a simulation of nature, you'd better make it quantum mechanical, and by golly it's a wonderful problem, because it doesn't look so easy.

— Richard Feynman, “Simulating Physics with Computers”,
Int. J. Theor. Phys., vol. 21, 467 (1982), at p. 486.

ABSTRACT

Computational modeling is becoming increasingly important in the highly active field of materials physics. Being able to reliably model systems quantum mechanically from first principles gives rise to novel possibilities for investigating material properties. Some of the most successful and widely used approaches are based on density functional theory (DFT).

In this thesis DFT-based band structure calculations were employed to model core-level shifts at metal-organic interfaces and were then compared to X-ray photoelectron spectroscopy (XPS)-experiments.

The Vienna Ab initio Simulation Package (VASP) was used. To do the geometry optimizations, VASP in conjunction with the special tool GADGET was applied, which bears significant advantages for finding the minimum on the potential energy surface.

As a first step, a suitable unit cell had to be created, which proved to be rather cumbersome in the case of partly fluorinated alkyl thiolates as investigated in this work, because experimental measurements suggested several quite different unit cells for these systems.

Furthermore, calculations without including van der Waals (vdW)-forces and with two different implementations of the vdW^{surf}-method were compared concerning the tilt angles of the long, upright standing molecules. As it turned out, considering vdW-interactions is very important in this case, because the resulting geometries differ significantly.

After determining the geometries, X-ray photoelectron (XP)-spectra were modeled using an initial state based approach. Additionally, electrostatic screening effects and the finite escape depth of the electrons were considered in post processing.

Moreover, the contribution of chemically induced shifts versus collective electrostatic effects to the overall shift was investigated. Even though often overlooked, the latter influence the electrostatic potential and, as a consequence, shift the measured core levels. Therefore, great care has to be taken when interpreting XPS-measurements and it is shown that DFT-based simulations provide highly valuable insights and are often necessary for a correct interpretation of XP-spectra.

ZUSAMMENFASSUNG

Im hochaktuellen Forschungsgebiet der Materialphysik spielen Computersimulationen eine immer wichtigere Rolle. Dies ist darauf zurück zu führen, dass mit quantenmechanischen ab-initio Simulationen auch komplexe Materialeigenschaften berechnet werden können. Einige der vielseitigsten und erfolgreichsten Methoden dafür beruhen auf der Dichtefunktionaltheorie (DFT).

In der vorliegenden Arbeit wurden auf der DFT basierende Bandstrukturrechnungen durchgeführt, um die Energie der inneren (kernnahen) Elektronen von organischen selbstorganisierten Monolagen [engl: self assembled monolayers (SAMs)] auf Metallsubstraten zu berechnen. Diese lassen sich experimentell mittels Röntgenphotoelektronenspektroskopie messen.

Die Berechnungen wurden mit dem Vienna Ab initio Simulation Package (VASP) unter Zuhilfenahme des Programms GADGET durchgeführt, welches enorme Vorteile bei der Bestimmung des Minimums auf der Potentialoberfläche des Systems mit sich bringt.

Um ab-initio Simulationen durchführen zu können, muss eine passende Einheitszelle für das System erstellt werden. Im Fall der in dieser Arbeit untersuchten teilweise fluorierten Alkylthiolate stellte sich dies als nicht trivial heraus.

Als nächster Schritt wurde auch der Einfluss von van der Waals (vdW)-Kräften untersucht. Dafür wurden Simulationen mit zwei verschiedenen Implementierungen der vdW^{surf} -Methode und Berechnungen ohne Berücksichtigung von vdW-Wechselwirkungen verglichen. Da sich die jeweils gefundenen Geometrien der langen, aufrecht stehenden Moleküle der SAM deutlich voneinander unterscheiden, ist in diesem Fall das Einbeziehen von vdW-Kräften essentiell.

Für die Simulation der Röntgenphotoemissionsspektren wurde eine auf dem *initial state* Zugang basierte Methode verwendet. Des Weiteren wurden zusätzlich elektrostatische Abschirmungseffekte und die begrenzte Austrittstiefe der Elektronen bei der Modellierung der Spektren berücksichtigt.

Schlussendlich wurde auch der Einfluss von kollektiven, elektrostatischen Effekten auf das Röntgenphotoemissionsspektrum untersucht. Dieser wird neben den chemischen Verschiebungen häufig vernachlässigt, ist aber gerade in geordneten, dicht gepackten Systemen von großer Bedeutung.

Zusammenfassend kann gesagt werden, dass für die korrekte Interpretation von gemessenen Röntgenphotoemissionsspektren die theoretischen Betrachtungen einen wertvollen Beitrag leisten und oftmals ohne diese eine korrekte Auswertung der experimentellen Daten nicht möglich ist.

ACKNOWLEDGMENTS

First of all, I want to thank my supervisor *Egbert Zojer* for his patient support and guidance during my Master's thesis, for teaching me how to do science and allowing me to be part of such an unrivaled group. Furthermore, I want to thank all former and current *EgbertInnen* for always being helpful and for discussions about everything under the sun. Enjoying their company during lunch and the occasional coffee break made working even more fun.

I would like to specifically mention Iris Hehn for working together on our joint paper. For doing all the [FHI-AIMS](#) calculations for the aforementioned paper and especially for fruitful discussions I want to thank Oliver Hofmann.

I also would like to thank Michael Zharnikov and the members of his group from Heidelberg University for the collaboration and for valuable experimental insights regarding [XPS](#)-measurements.

For providing computational resources and support I would like to thank the ZID of the TU Graz (icluster and dcluster) as well as the people from Vienna running the VSC2 and VSC3. I am grateful to Andreas Hirczy of the Institute of Theoretical and Computational Physics here at TU Graz for installing all the software I needed when I was a teaching assistant.

I would like to acknowledge financial support by the Austrian Science Fund (FWF), Projects P24666-N20 and I937-N19. Thanks to that I was able to attend the Spring Meeting of the Deutsche Physikalische Gesellschaft in Berlin and the Summerschool in Sønderborg. Finally, I want to gratefully acknowledge the Erasmus Program which gave me the opportunity to study a semester at Loughborough University, UK.

SPECIAL THANKS TO

Everyone I enjoy being with :)

CONTENTS

| | | |
|-----------|---|-----------|
| I | Fundamental aspects | 1 |
| 1 | INTRODUCTION AND MOTIVATION | 2 |
| 2 | THEORETICAL BASICS | 4 |
| 2.1 | From $3N$ to 3: Density Functional Theory | 5 |
| 2.1.1 | Hohenberg-Kohn theorem | 5 |
| 2.1.2 | Kohn-Sham equation | 6 |
| 2.1.3 | The exchange-correlation functional | 7 |
| 2.2 | The computational solid state's view of reality | 8 |
| 2.2.1 | Bloch theorem | 8 |
| 2.2.2 | K-points | 8 |
| 2.2.3 | Basis sets | 9 |
| 2.2.4 | Energy cutoff | 9 |
| 2.2.5 | Augmented reality: plane waves and projectors | 10 |
| 2.2.6 | Kohn-Sham eigenstates | 10 |
| 2.2.7 | Calculating core-level energies | 12 |
| II | Results | 16 |
| 3 | METHODOLOGY | 17 |
| 3.1 | Computational implementation | 17 |
| 3.1.1 | VASP and GADGET: a powercouple | 18 |
| 3.1.2 | Selected INCAR tags | 19 |
| 3.1.3 | Hands on notes | 20 |
| 3.1.4 | Putting atoms in a box | 20 |
| 3.1.5 | Optimizing the system | 21 |
| 3.2 | Screening effects | 23 |
| 3.3 | Broadening delta peaks | 24 |
| 3.4 | Damping | 25 |
| 3.5 | Creating the spectrum | 26 |
| 3.6 | Shifting and stretching | 27 |
| 4 | INVESTIGATED SYSTEMS | 28 |
| 4.1 | Full coverage systems | 31 |
| 4.2 | Low coverage systems | 32 |
| 5 | MODELING X-RAY PHOTOELECTRON SPECTRA OF PARTLY FLUORINATED ALKYL THIOLATES | 35 |

| | | |
|-------|---|----|
| 5.1 | Finding a suitable unit cell | 36 |
| 5.2 | A closer look at the fluorinated part | 40 |
| 5.3 | Impact of the length of the fluorinated segment | 42 |
| 5.4 | Residual attractive or repulsive: vdW-forces | 45 |
| 5.5 | Collective electrostatic effects | 48 |
| 5.6 | Hard, soft or somewhere inbetween: PAW-potentials | 51 |
| 5.7 | VASP vs. FHI-aims | 53 |
| 5.8 | Final state tests | 54 |
| 5.8.1 | Full core hole | 55 |
| 5.8.2 | Half-full core hole | 56 |
| 6 | CONCLUSIONS AND OUTLOOK | 58 |

III Appendix 59

| | | |
|-----|-----------------------------|----|
| A | TYPICAL INPUT FILES | 60 |
| A.1 | INCAR | 60 |
| A.2 | KPOINTS | 62 |
| A.3 | INPDAT | 62 |
| A.4 | control.in | 63 |
| B | SOFTWARE USED FOR THIS WORK | 72 |
| | BIBLIOGRAPHY | 73 |

ACRONYMS

| | |
|-----------------|--|
| DFT | density functional theory |
| DNA | desoxyribonucleic acid |
| F6H11SH | 12,12,13,13,14,14,15,15,16,16,17,17,17-tridecafluoroheptadecane-1-thiolate |
| F8H11SH | 12,12,13,13,14,14,15,15,16,16,17,17,18,18,19,19,19-heptadecafluorononadecane-1-thiolate |
| F10H11SH | 12,12,13,13,14,14,15,15,16,16,17,17,18,18,19,19,20,20,21,21,21-henicofluorohenicosane-1-thiolate |
| FHI-AIMS | Fritz Haber Institute ab initio molecular simulations package |
| GGA | general gradient approximation |
| HOMO | highest occupied molecular orbital |
| HRXPS | high resolution X-ray photoelectron spectroscopy |
| HRXP | high resolution X-ray photoelectron |
| IP | ionization potential |
| IUPAC | International Union of Pure and Applied Chemistry |
| LDA | local density approximation |
| NEXAFS | near edge X-ray absorption fine structure |
| PAW | projector augmented wave |
| PBE | Perdew-Burke-Ernzerhof |
| SAM | self assembled monolayer |
| UPS | ultraviolet photoelectron spectroscopy |
| VASP | Vienna Ab initio Simulation Package |
| vDW | van der Waals |
| XP | X-ray photoelectron |
| XPS | X-ray photoelectron spectroscopy |

Part I

Fundamental aspects

INTRODUCTION AND MOTIVATION

One of the greatest quests in science is to find a way to analytically solve the relativistic Schrödinger equation for an arbitrary system. Unfortunately, nowadays this is only possible for a few quite simple systems (for an up-to-date list see, e. g., wikipedia¹). So far the closest call for solving *real world problems* lies in numerical simulations, especially density functional theory (DFT) seems to be able to accomplish this - at least theoretically. In practice there is still the small detail of not knowing the analytical expression of the exchange-correlation potential. Non the less, it is the most promising technique for doing ab-initio calculations, being limited to (periodic) systems of a couple of hundred atoms in a unit cell at present computing power. One of the most advanced tools to do these kind of calculations is the Vienna Ab initio Simulation Package (VASP) [1-3].

This work models X-ray photoelectron (XP)-spectra of SAMs on a metal substrate by means of DFT calculations and explores the boundaries of this approach. Being able to simulate these kind of systems gives a convenient tool for testing different SAMs, which are covalently-bonded to a given substrate to tune its properties.[4-6] These interface-modifiers can control different aspects of a surface, e. g., its wettability [7-9] or work function [10, 11]. Especially tuning the work function is of vital importance for electronic applications, which can be done by using SAMs with a polar terminal part.[12-18] Even more versatile are SAMs with an embedded polar group [19-21], because in this case the terminal end of the molecule stays the same, even though the work function is modified, and, furthermore, the electronic states within the SAM and their alignment relative to the Fermi-level of the system change.[22, 23] These kind of modifications have been done for both electrode-semiconductor [12, 13, 19, 24-26] and dielectric-semiconductor interfaces [14, 27]. Furthermore, they have even been utilized for active layers in organic transistors.[28-30] Another important task of SAMs is to protect a given substrate from corrosion [31] or modify it to allow the adhesion of biological cells [32]. Nowadays, they are also used to build sensors [33, 34] and for nanopatterning [35-37].

To characterize such SAMs X-ray photoelectron spectroscopy (XPS), which is a surface sensitive technique, is used quite commonly.[38, 39] By analyzing XP-spectra it is possible to verify the chemical integrity of the SAM, because measured shifts of the core-level binding energies are greatly affected by the immediate chemical environment of an atom. Furthermore, it can enhance the understanding of the detailed composition of a SAM and also its homogeneity after deposition.[40] It should be noted that not only the chemical neighborhood influences the shifts of core-level binding energies of an atom, but also other factors should be taken into

¹ https://en.wikipedia.org/wiki/List_of_quantum-mechanical_systems_with_analytical_solutions

account, depending on the system under investigation.[20, 41–44] These are, among others, the Madelung energy if you are dealing with ionic crystals [45, 46], or the change of the local electrostatic energy due to potential shifts induced by polar groups incorporated into a SAM [20, 21]. The latter is especially important for this work, because it is crucial to consider these collective electrostatic effects when modeling long, upright standing SAMs on metal surfaces. These effects have been discussed quite thoroughly to describe the valence electronic structure of organic adsorbate layers [47–49], as well as to explain adsorbate-induced work function modifications [16, 47–51]. Quite recently it has been proposed to utilize collective electrostatic effects for designing monolayers with complex electronic properties.[22]

Due to the fact that with XPS said effects can be investigated, it is a valuable technique for characterizing the local electrostatic energy in complex adsorbate systems. However, it is absolutely vital, if one wants to utilize XPS for such a task, to thoroughly understand how chemical shifts and collective electrostatic effects influence each other to produce the finally measured XP-spectra.

There are different ways to simulate XP-spectra using DFT which will be presented in this work. To be more specific, the initial state and final state approach are investigated with particular attention being paid to effects arising when using SAMs consisting of long, upright standing molecules. The treatment of core-level shifts in these kind of systems differs quite a bit of the already extensively investigated surface core-level shifts. Correctly describing the interplay of chemically induced shifts and collective electrostatic effects by means of DFT lies at the center of this thesis, whose most interesting findings have already been published.[52] Being able to compare the theoretically produced results with experimentally obtained spectra provides means of validating the proposed hypotheses. Therefore, partly fluorinated alkyl thiolates were chosen to be investigated, more precisely the systems used in the work of Lu et al. [53], which were characterized using high resolution X-ray photoelectron spectroscopy (HRXPS) measurements, and, therefore, high quality data is available for comparison.

THEORETICAL BASICS

For the chapters dealing with fundamental aspects the following books served as reference: [54–56]. As already mentioned in the introduction, solving the Schrödinger equation for an arbitrary system has been a challenge of great interest in modern science. Even though, for complicated systems, as they occur in *real world*-problems, one is still limited to various numerical approximations to solve the Schrödinger equation, which in its most general form is given as:

$$i\hbar \frac{\partial}{\partial t} \psi(\mathbf{r}, t) = \hat{H} \psi(\mathbf{r}, t) \quad (1)$$

In solid state physics and quantum chemistry solving the non-relativistic, time-independent Schrödinger equation

$$\hat{H} \psi(\mathbf{r}_1, \dots, \mathbf{r}_N, \mathbf{R}_1, \dots, \mathbf{R}_M) = E \psi(\mathbf{r}_1, \dots, \mathbf{r}_N, \mathbf{R}_1, \dots, \mathbf{R}_M) \quad (2)$$

for the many-electron wave function ψ is the ultimate goal. In equation (2) \hat{H} denotes the Hamiltonian for a molecular system in the absence of a magnetic field containing M nuclei and N electrons, and \mathbf{r}_i and \mathbf{R}_I are the positions of the electrons and nuclei, respectively. A fundamental approximation goes back to Born and Oppenheimer [57], who suggested to separate the nuclear and the electronic part of the wave function:

$$\Psi_{total} = \Psi_{electrons} \cdot \Psi_{nuclei} \quad (3)$$

This can be justified because of the around 2000 times bigger mass of the nucleus compared to the electrons, which means that one can describe the latter moving in a fixed field of the former without influencing it in practice.

Keeping this in mind, the Schrödinger equation can be rewritten to describe the time-independent, many-electron problem as follows:

$$\begin{aligned} \hat{H} \psi &= \left[\hat{V} + \hat{T} + \hat{U} \right] \psi = \left[\sum_i^N V(\mathbf{r}_i) + \sum_i^N -\frac{\hbar^2}{2m} \nabla_i^2 + \sum_{i<j}^N U(\mathbf{r}_i, \mathbf{r}_j) \right] \psi \\ &= E \psi. \end{aligned} \quad (4)$$

Unfortunately, this equation is still not solvable in a direct manner, because it yields a very large number of variables, namely $3N$ per particle (only including the three spatial coordinates and neglecting, e. g., the N spin coordinates for electrons). Taking into account that interesting physical problems deal with systems which contain $N = \mathcal{O}(10^{24})$ particles, one can grasp quite easily that this is not a simple *pen and*

paper-problem. To conquer this challenge, there exist nowadays two widely used, but contrary approaches, namely wave function based methods and **DFT**.

2.1 FROM 3N TO 3: DENSITY FUNCTIONAL THEORY

The most successful method for modeling materials is **DFT**. It is a quantum mechanical modeling method, using a first-principles approach to calculate the wanted quantities, which is used in physics and chemistry to investigate the electronic structure of complex many-body systems. In the solid state world it is used to describe ground state properties of metals, semiconductors and insulators. Yet the success of **DFT** not only encompasses standard bulk materials, but also complex organic structures such as proteins and the recently famous carbon nanotubes. The main idea of **DFT** is to describe an interacting system of fermions via its electron density and not via its many-body wave function. This means, for N electrons in a solid, which obey the Pauli exclusion principle [58] and interact with each other via the Coulomb potential, the system depends only on *three* - the spatial coordinates x , y , and z - rather than $3N$ degrees of freedom.

2.1.1 Hohenberg-Kohn theorem

One of the fundamental ideas **DFT** relies on is the fact that it is possible to reformulate the energy of an atomic system as a functional of the ground state electron density instead of the electron wave function. This goes back to the ground breaking work of Pierre Hohenberg and Walter Kohn in 1964 [59], who built on the concept introduced by Llewellyn Thomas [60] and Enrico Fermi [61] known as the Thomas-Fermi model. The first Hohenberg-Kohn theorem asserts that there exists *one unique mapping* between the ground state electron density of a system and its ground-state wave function.

THEOREM 1. The ground state energy of a system of interacting electrons is a unique functional of the electron density.

$$\psi_0(\mathbf{r}_1, \dots, \mathbf{r}_N) \leftrightarrow n_0(\mathbf{r}) \quad (5)$$

This relationship shows that the ground-state electron density determines all ground-state properties of a system. The ground-state electron density $n_0(\mathbf{r})$ is a functional of the ground-state wave function $\psi_0(\mathbf{r}_1, \dots, \mathbf{r}_N)$:

$$n_0(\mathbf{r}) = n_0[\psi_0(\mathbf{r}_1, \dots, \mathbf{r}_N)] \leftrightarrow n_0(\mathbf{r}) = \langle \psi_0 | \sum_i^N \delta(\mathbf{r} - \mathbf{r}_i) | \psi_0 \rangle \quad (6)$$

This means, changing the external potential \hat{V} in equation (4) changes the wave function of the system, and, as a consequence, the electron density $n(\mathbf{r}_0)$. Obviously, the ground state energy E_0 is also a functional of the ground-state wave function:

$$E_0(\mathbf{r}) = E_0[\psi_0(\mathbf{r}_1, \dots, \mathbf{r}_N)] = \langle \psi_0 | \hat{H} | \psi_0 \rangle \quad (7)$$

As one can see, this allows us to calculate the ground-state energy with only three variables instead of $3N$.

The second theorem by Hohenberg and Kohn states that there exists a variational principle for the above mentioned energy density functional $E[n_0(\mathbf{r})]$, namely:

THEOREM 2. The electron density that minimizes the energy of the overall functional is the true ground-state electron density.

$$\left. \frac{\delta E[n(\mathbf{r})]}{\delta n} \right|_{n=n_0} = 0 \quad s.t. \quad \int d^3r n(r) = N \quad (8)$$

This variational problem can be solved using the so-called Ritz method [62] to finally get the ground-state electron density and, more importantly, the ground-state energy.

For actual calculations, the total ground-state energy can be written as

$$E[n(\mathbf{r})] = V[n(\mathbf{r})] + T[n(\mathbf{r})] + U[n(\mathbf{r})], \quad (9)$$

but is not known analytically; only the external potential can be written as

$$V[n(\mathbf{r})] = \int d\mathbf{r} v(\mathbf{r}) n(\mathbf{r}), \quad (10)$$

whereas the kinetic part $T[n_0]$ and the interaction part $U[n_0]$ cannot be determined exactly for an interacting system, yet. Finding these two functionals would mean solving any **DFT**-problem exactly.

2.1.2 Kohn-Sham equation

Walter Kohn and Lu Jeu Sham tackled the problem of not knowing the exact functionals and suggested to split the problem into exact, non-interacting terms for the kinetic and interaction functionals and putting everything that is not known analytically into the *exchange-correlation* functional E_{XC} . They used the standard kinetic energy operator for a Slater-determinant basis for the kinetic part $T[n(\mathbf{r})]$, i. e., the kinetic energy as if dealing with non-interacting particles. Furthermore, they split the interaction part $U[n(\mathbf{r})]$ up into a known part, derived from the Hartree-Fock approach (representing the exact local Coulomb interaction) and into an unknown, which is accounted for in the aforementioned exchange-correlation functional. These results in equation (11) and (12) for the kinetic part, where also

the unknown exchange-correlation functional is added, and the interaction part, respectively.

$$U[n(\mathbf{r})] = \frac{e^2}{2} \int d^3r \int d^3r' \frac{n(\mathbf{r})n(\mathbf{r}')}{|\mathbf{r}-\mathbf{r}'|} + E_{XC}[n(\mathbf{r})] \quad (11)$$

$$T[n(\mathbf{r})] = \sum_i^N \int d^3r \psi_i^*(\mathbf{r}) \left(-\frac{\hbar^2}{2m} \nabla^2 \right) \psi_i(\mathbf{r}) \quad (12)$$

Equation (12) is the kinetic term for *non-interacting* particles, the ψ_i are representing atomic orbitals which create the wave-function by a Slater-determinant. Using Slater-determinants ensures that the wave-function is anti-symmetric [63] and, hence, the Pauli exclusion principle [58] is honored. This approach can be used, because as stated above, everything beyond this model is already included in the exchange-correlation functional E_{XC} in equation (11). To finally arrive at the famous Kohn-Sham equation, one has to use Lagrange multipliers for the variational Ansatz, which yields

$$\epsilon_i \psi_i(\mathbf{r}) = \left[-\frac{\hbar^2}{2m} \nabla_i^2 + v(\mathbf{r}) + e^2 \int d^3r' \frac{n(\mathbf{r})n(\mathbf{r}')}{|\mathbf{r}-\mathbf{r}'|} + \frac{\delta E_{XC}[n(\mathbf{r})]}{\delta n(\mathbf{r})} \right] \psi_i(\mathbf{r}) \quad (13)$$

for equation (9). Now we are, in principal, able to exactly solve our problem if we would know E_{XC} , by calculating the ground-state electron density and, as a consequence, also the ground-state energy, as stated in THEOREM 1. This has to be done in a self-consistent manner, meaning that one has to start with an educated guess for the initial electron density $n(\mathbf{r})$ to solve the Kohn-Sham equation. Having the Kohn-Sham orbitals allows us to calculate a new electron density via

$$n(\mathbf{r}) = \sum_i^{occ} \|\psi_i(\mathbf{r})\|^2. \quad (14)$$

This cycle has to be repeated until convergence is reached and the true ground-state electron density is found as stated in THEOREM 2. Unfortunately, this only works exactly in theory, because the analytical expression for the exchange-correlation functional E_{XC} is not known, meaning that only an approximated solution is possible to obtain.

2.1.3 The exchange-correlation functional

Finding the most universal expression for the XC-functional is one of the major challenges in DFT and nowadays there exist several different approaches to tackle this obstacle. The most widely used approaches are the local density approximation (LDA) [64] and the semi-local general gradient approximation (GGA) [65], which builds on the former but also includes the gradient of the electron density to yield more accurate results. For this thesis the widely used and highly successful Perdew-Burke-Ernzerhof (PBE)-functional was used, which is a GGA based functional. A

comparison of different functionals can be found in [66] and, specifically focused on the ones included in VASP, in [67]. There is also another class of functionals, so-called hybrid functionals, which include a portion of exact exchange from Hartree–Fock theory and were introduced by Becke [68] in 1993. These, in a lot of cases semi-empirical, hybrid functionals can improve the modeled molecular properties like bond length and atomization energies, as well as vibrational frequencies compared to pure ab initio functionals.[69]

2.2 THE COMPUTATIONAL SOLID STATE'S VIEW OF REALITY

As the universe is infinite in every direction, so is the solid state physicist's view of any matter, i. e., a box with periodic boundary conditions in every spacial direction. This is quite handy for describing bulk-like systems of ideal crystals, but not for *real world*-systems, which, after all, have to end somewhere, and, therefore, bear a surface. If one wants to investigate surfaces, it is a necessity to somehow break out of this artificial box with periodic boundary conditions by using, e. g., the repeated slab approach as described in chapter 3.1.4 in detail.

2.2.1 Bloch theorem

To describe such a system (vide supra), one has to start with an ideal crystal without any surface, which can be described by *Bloch's theorem*. The concept thereof is nicely explained in chapter 12.2 of [70].

2.2.2 *K*-points

Building on the periodicity of crystal symmetry the first Brillouin zone is of utmost importance, because all key quantities such as the total energy, the charge density or the density of states require integrating over the first Brillouin zone only. Computationally this integration can be approximated by a weighted sum over a discrete set of points in the first Brillouin zone, the so-called *k*-points.

$$\frac{1}{\Omega_{BZ}} \int_{BZ} d\mathbf{k} f_{\mathbf{k}} \quad \rightarrow \quad \sum_{\mathbf{k}} \omega_{\mathbf{k}} f_{\mathbf{k}} \quad (15)$$

where Ω_{BZ} denotes the volume of the unit cell, i. e., the first Brillouin zone, and the weights $\omega_{\mathbf{k}}$ sum up to 1. The number of *k*-points in each direction should be inversely proportional to the length of the lattice vectors in this direction. Furthermore, if there are effective periodic boundary conditions only in two spatial directions, i. e. when using the repeated slab approach (see chapter 3.1.4), there should be only one *k*-point in the third spatial direction. Having more than one *k*-point in *z*-direction to integrate over would mean including interactions between the unit cells in this direction and introducing unwanted phase transitions.

The two most commonly used grids are the Monkhorst-Pack [71] and the Γ -centered mesh, which is just a shifted Monkhorst-Pack grid to include the Γ -point. Both grids can be generated automatically with the number of k-points per spatial direction as input parameter.

Furthermore, one has to find a compromise between accuracy and computational cost, because each additional k-point introduces a new Kohn-Sham system which needs to be solved self-consistently. Having an independent Kohn-Sham system to solve per k-point is only true for, e. g., LDA and GGA functionals, but does not hold for hybrid functionals - in this case all k-points are dependent on each other.

2.2.3 Basis sets

For actually solving the Kohn-Sham equation (13) the Kohn-Sham wave functions (14) have to be expanded into a set of well chosen basis functions. Principally, there are two different ways of doing so: an atomic-independent approach, typically plane waves, or atom-centered functions. A general, more exhausted explanation can be found in chapter 13 of [70]. For periodic systems as used in VASP a plane wave basis set is a logical choice, although a cutoff energy (vide infra) has to be defined, which crucially determines the accuracy and, of course, the computational cost. When using plane waves, all cell periodic functions, i. e., the periodic part $u_{n\mathbf{k}}(\mathbf{r}) = u_{n\mathbf{k}}(\mathbf{r} + \mathbf{R})$ of the wave functions $\psi_{n\mathbf{k}}(\mathbf{r}) = u_{n\mathbf{k}}(\mathbf{r})e^{i\mathbf{k}\mathbf{r}}$, can be written as a sum of plane waves:

$$\psi_{n\mathbf{k}}(\mathbf{r}) = \frac{1}{\sqrt{\Omega}} \sum_{\mathbf{G}} C_{\mathbf{G}n\mathbf{k}} e^{i(\mathbf{G}+\mathbf{k})\mathbf{r}} \quad (16)$$

with $C_{\mathbf{G}n\mathbf{k}} = \langle \mathbf{G} + \mathbf{k} | \psi_{n\mathbf{k}} \rangle$ and Ω denoting the volume of the first Brillouin zone.

2.2.4 Energy cutoff

In calculations a cutoff energy is defined which limits the number of plane waves $|\mathbf{G} + \mathbf{k}|$ included. The cutoff energy sets the maximum kinetic energy of a plane wave in the following way:

$$\frac{\hbar^2}{2m} |\mathbf{G} + \mathbf{k}|^2 < E_{cut} \quad (17)$$

This means that a set of plane waves is restricted to a sphere in reciprocal space with its radius being proportional to the square root of the cutoff energy.

2.2.5 Augmented reality: plane waves and projectors

Utilizing a simple plane wave basis set to express the Kohn-Sham wave functions (14) bears some obstacles to keep in mind, because dealing with the Schrödinger equation in a numerical manner poses several challenges to the basis set. Most notably two numerically fundamental different regimes have to be tackled, the core- and valence-region, respectively. In the former the electrons, having a large kinetic energy, are represented by a rapid oscillating wave function, which, as a result, requires an immensely fine grid and an extremely large set of plane waves to be solved accurately. In the latter region the kinetic energy of the valence electrons is comparably small, resulting in a wave function which strongly responds to the environment, but is much more smooth. This means a somewhat smaller cut off energy for the plane waves is sufficient for getting accurate results.

A clever way to solve this problem is to use the projector augmented wave (PAW) method as developed by Blöchl [72], which utilizes a muffin-tin approach 2. Using this scheme, the solution is principally constructed out of two parts, an atom centered, localized contribution evaluated by radial integration and an interstitial part, represented by smooth functions in a plane wave basis set. The core electrons are described using the so-called *frozen core approximation*. This means, the core electrons are pre-calculated in an atomic environment and kept frozen for the remaining calculations. The basic idea of the PAW-method lies in the use of a smooth projector function to deal with the non-smooth part of the wave function around the core of an atom by replacing the true potential by a smooth pseudo potential.

$$|\Psi\rangle = \hat{\mathcal{T}} |\tilde{\Psi}\rangle. \quad (18)$$

The resulting transformation operator $\hat{\mathcal{T}}$ transforms the aforementioned pseudo wave function $|\tilde{\Psi}_i\rangle$ into an all-electron wave function $|\Psi_i\rangle$. A schematic sketch of the all-electron wave function and its pseudo wave function is shown in figure 1.

One of the advantages of the PAW-approach compared to an all-electron method is that it is computationally much cheaper, because of the fact that not every electron, e. g., of a gold substrate atom has to be computed, but only the valence electrons are considered individually. Nonetheless, the results for a lot of different use cases are comparable in accuracy. For modeling XPS-measurements as done in this thesis, the acquired results utilizing different PAW-potentials (see chapter 5.6) were compared to all-electron calculations (cf., chapter 5.7) and good agreement was found.

An explanation of how the PAW-potentials as distributed by VASP are generated can be found in the work of Kresse and Joubert [73].

2.2.6 Kohn-Sham eigenstates

Since the beginning of Kohn-Sham-DFT there has been a debate about what physical meaning, if any at all, can be associated to Kohn-Sham-orbitals.[74]

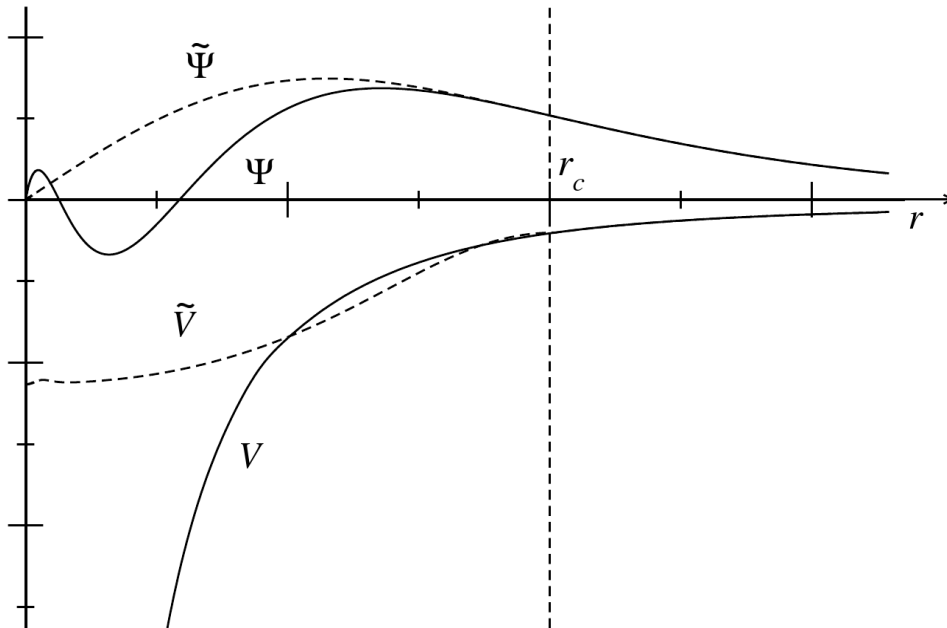


Figure 1: Schematic plot of a wave function (Ψ) and its pseudo wave function ($\tilde{\Psi}$) as used in the PAW framework. The dotted vertical line denotes the critical radius (r_c) where the pseudo wave function in the muffin tin equals the all-electron wave function which is used in the interstitial region (see text). The potential V and its pseudo-potential \tilde{V} is also shown. Figure taken from Martijn Marsman. VASP: Plane waves, the PAW method, and the Selfconsistency cycle. DFT and beyond, 14th July 2011, Berlin, Germany.

Quite recently the studies of Baerends et al. [75] and Bellafont et al. [76] showed that the interpretation of the Kohn-Sham-orbital energies is still a quite discussed topic nowadays, as it was ever since first introduced.[46, 77, 78]

What is undisputed, though, is the ionization potential (IP)-theorem[79], which is valid for the exact, however, unknown Kohn-Sham potential and states that the calculated Kohn-Sham highest occupied molecular orbital (HOMO) energy ϵ_{HOMO} equals the negative *relaxed* exact IP of the system:

$$\epsilon_{HOMO} = -\epsilon_{IP} = E(N-1) - E(N), \quad (19)$$

whereas $E(N-1)$ equals the energy of the system with one electron removed and $E(N)$ is the energy before ionization.

In this context *relaxed* means that relaxation effects due to the ionization of the orbitals are already considered in this Kohn-Sham energy. The IP-theorem is reminiscent of Koopman's theorem [80] in Hartree-Fock theory, which is only valid for the *unrelaxed* IP, though, and, therefore, does not consider any ionization-induced relaxation effects of the system. Another important theorem concerning the Kohn-Sham eigenstates is Janak's theorem [81], which states that the variation in total energy

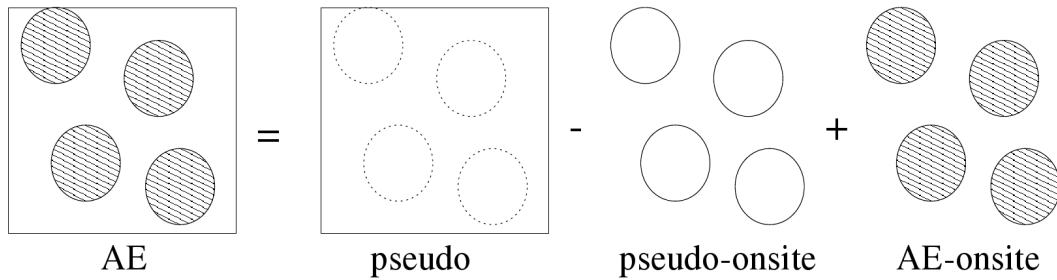


Figure 2: Principle of the [PAW](#) muffin-tin approach. The all-electron wave function (AE) is constructed out of a pseudo wave function (pseudo) minus the pseudo wave function onsite (pseudo-onsite) plus the all-electron wave function onsite (AE-onsite), where AE, pseudo-onsite and AE-onsite are atom centered localized functions and pseudo is a pseudo wave function expanded in plane waves. Figure taken from Martijn Marsman. VASP: Plane waves, the PAW method, and the Selfconsistency cycle. DFT and beyond, 14th July 2011, Berlin, Germany.

with respect to the orbital occupation n_i is equal to the corresponding Kohn-Sham eigenvalue of orbital i :

$$\delta E / \delta n_i = \epsilon_i. \quad (20)$$

Although, the validity of Janak's theorem was questioned by Valiev et al. in 1995 [82], this approach is widely in use nowadays.[83] Strictly speaking, Janak's Theorem can only be applied when adding or removing an electron from the [HOMO](#), but, nonetheless, it is successfully used also for other orbitals, in particular for calculating electron binding energies of core levels.[64, 84, 85] Being able to calculate core-level binding energies is especially important for modeling [XP](#)-spectra.

2.2.7 Calculating core-level energies

When calculating core-level energies in the [DFT](#)-framework, one can rely on several theorems (vide supra). Normally, in [DFT](#) the binding energy is calculated as the energy difference of two separate systems, namely one with the system in its ground state, and the second with one electron removed. In passing it is noted, that it is assumed that the core hole is entirely localized at one atom, which should be a sound approximation in most cases. This energy difference is a measure for the experimentally acquired core-level binding energy:

$$E_{CL} = E(N - 1) - E(N). \quad (21)$$

Utilizing [VASP](#) for this task, there are several strategies which one can apply.

2.2.7.1 *Initial state method*

The most straightforward option is to just use the so-called *initial state method*, which means the Kohn-Sham orbital energies are taken as the core-level binding energies. To get the (core-level) orbital energies, the Kohn-Sham orbitals are recalculated after the self-consistent field calculation of the valence charge density is converged. Then, the initial state binding energy can be reported with respect to the Fermi-energy:

$$E_{CL}^{initial} = \epsilon_{KS} - \epsilon_F. \quad (22)$$

This is computationally the cheapest way, because only a single calculation is needed to get the core-level energies of all atoms. Doing so neglects any relaxation effects due to the missing core electron, though, because no change of the potential is allowed after removing the electron. Therefore, electronic screening is entirely neglected. An overview of the implementation in [VASP](#) can be found in the work of Köhler et al. [86], which does not only cover the initial state method, but also the final state method.

2.2.7.2 *Final State Method*

The final state method is a priori a more sophisticated approach due to the fact that it considers quantum mechanical relaxation effects of the neighborhood of the hole due to the removed electron and also includes screening effects of the metal.

There are different ways to calculate final state effects, e. g., moving 1 or $\frac{1}{2}$ e^- to the valence band, the latter being known as the Slater-Janak transition state method [87]. This method states that the Kohn-Sham eigenvalue of a half-occupied state equals the binding energy of its electron on the assumption that the Kohn-Sham eigenvalues are linear functions of the occupation number of the orbitals. A thorough explanation and numerical investigation can be found in the work of Göransson et al. [83]. Another quite widely used approach is the so-called $(Z+1)$ - or *equivalent core* approximation, where it is assumed that the core hole is completely screened by the valence electrons, i. e., the core hole is assumed to act as an extra proton in the atom, and, hence, the atom is replaced by the next element in the periodic table.

As a matter of fact, final state effects are quite crucial for surface core level shifts [46, 88–90], because of the instant screening of the core hole by the electrons of the metal bulk, which acts as an infinite electron reservoir.

A mayor downside of employing the final state method to calculate [XP](#)-spectra is the fact that it is computationally way more costly. This is due to having to run a self consistent field-calculation for every single orbital which contributes to the spectrum, in contrast to just one calculation in the case of the initial state method.

Furthermore, a big enough unit cell has to be constructed to avoid an artificial dipole layer, which would be introduced due to the periodic boundary conditions.[47] As can be seen in figure 3, a periodic array of point dipoles forms a layer perpendicular to the surface if the unit cell is too small, which modifies the work function and electron affinity of the surface. The situation is even more instructively shown in

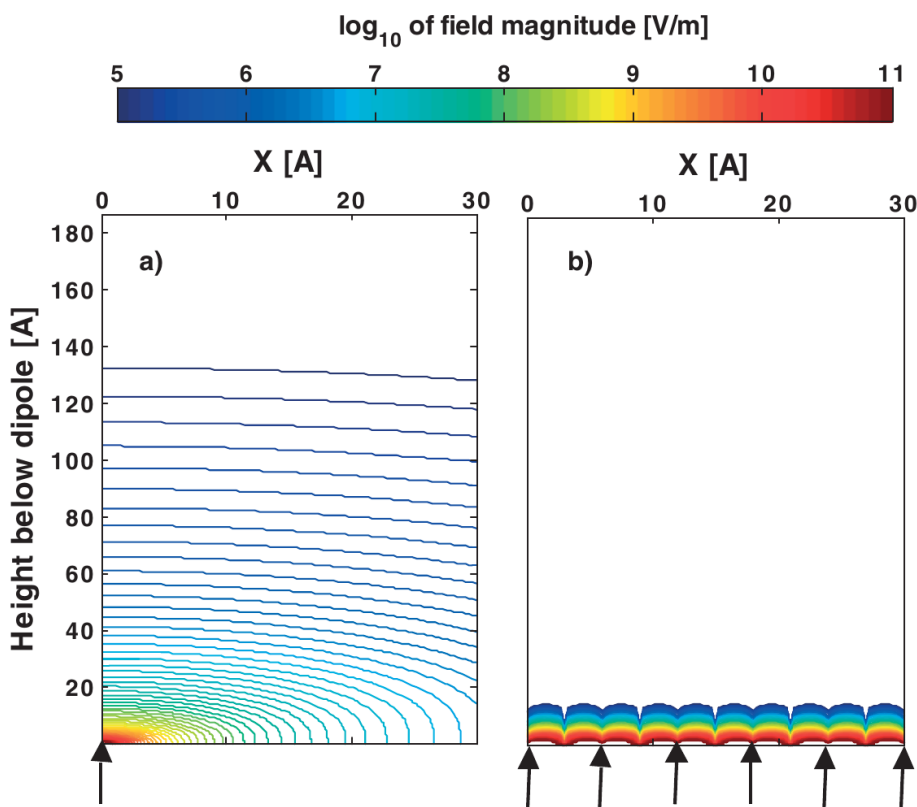


Figure 3: Distribution of the electric field magnitude, on a logarithmic scale, in the xz plane due to: a) A single dipole with $p = 4$ Debye and $d = 2$ Å; b) A square array of such dipoles with inter-dipole separation of $a = b = 6$ Å. Dipole positions are indicated on the figure as arrows. Reproduced with permission from [47].

figure 4, where a single molecule and a SAM of molecules with their respective potential energy, and, furthermore, the change of the work function due to the collective electrostatic effects, is plotted. This contrasts the picture during an XPS-measurement, which is more appropriately described by a single dipole, i. e., only one atom is excited and its core-level electron is measured at the same time. These point dipoles are generated due to the removal, i. e., excitation, of the core-level electron, which creates a positive charge in the SAM. The size of the point dipole depends on the distance from the metal substrate to the atom probed, i. e., the distance between the positive charge Looking at the systems investigated in this thesis, incorporating long, upright standing molecules, it would be practically infeasible to construct a big enough unit cell to actually deal with a single dipole and not a dipole layer. For further details, including some tests utilizing the final state method as implemented in VASP, please refer to chapter 5.8 of this work.

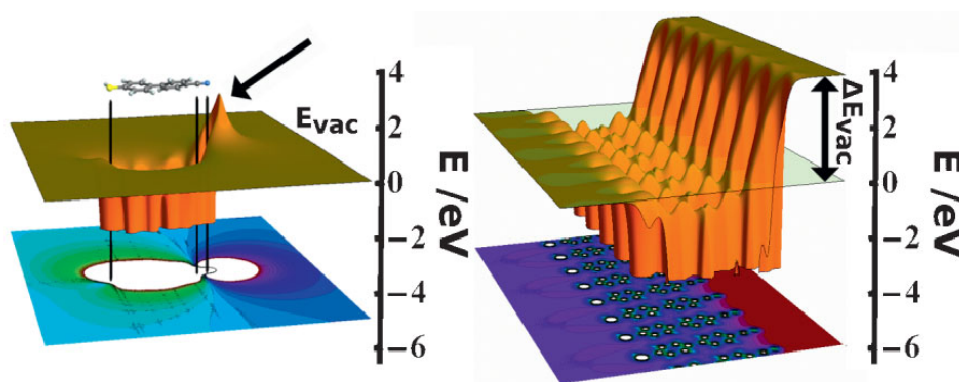


Figure 4: a) Electron potential energy in the plane of an isolated HS|2P|CN molecule and corresponding contour plot. The black vertical lines help locating the position of docking and head group in both plots. b) Equivalent plots for an infinitely extended 2D HS|2P|CN SAM, averaged over one dimension. A semi-transparent plane at the energy of the left-side vacuum level helps spotting the step ΔE_{vac} in the electron potential energy across the monolayer. Reproduced with permission from [48].

Part II

Results

METHODOLOGY

In this chapter the model systems used in the course of this work are explained and the methodology used for the simulations is outlined briefly. Doing ab-initio band-structure based **DFT**-calculations requires one to decide which exchange-correlation functional to use. Furthermore, one has to define certain input parameters beforehand, e. g., the size of the used unit cell and the arrangement of the atoms inside it. A crucial task when doing ab-initio calculations is finding the (global) minimum on the potential energy surface of the system. Finally, after the **DFT**-calculation of the geometrically optimized system is converged within a chosen uncertainty, one can extract all wanted quantities of the system.

3.1 COMPUTATIONAL IMPLEMENTATION

Most of the **DFT**-calculations were done using **VASP**, in our special version called *5.3.3-tomas_extension*, which is basically the official version 5.3.3 with a couple of enhancements done by Tomáš Bučko concerning mostly the treatment of van der Waals (**vdW**)-interactions (see chapter 5.4). For some calculations an older version of **VASP**, namely 5.3.2, was used to be able to do the simulations with another set of **PAW**-potentials, generated to be compatible with this earlier version. The reason was to be consistent with the calculations obtained by our group member Iris Hehn, and, eventually, being able to publish a joint paper [52]. All details concerning the **PAW**-potentials used in this work, and also for the results in, e. g., chapter 5.4, are discussed in the aforementioned paper and its supporting information. Even though different versions of **PAW**-potentials were used throughout this thesis the results obtained with both versions are equally valid. As already noted, all simulations were done using the **PBE**-exchange-correlation functional and most of the time the **PAW**-potentials distributed with **VASP** version 5.3.3 were utilized, whose exact names are shown in table 1.

Another point to keep in mind is the fact that the required computational resources scale roughly with the size of the unit cell (cf., chapter 3.1.4), even if it is just empty space and there are no additional atoms there, because of the plane wave approach (see chapter 2.2.3) **VASP** utilizes when using **PAW**-potentials. What is less relevant, though, in contrast to, e. g., full potential codes like the Fritz Haber Institute ab initio molecular simulations package (**FHI-AIMS**) [91], is what kind of atoms are in the unit cell, and, consequently, which **PAW**-potentials are used. This is due to the fact that **VASP** does not calculate every single electron, but rather uses the **PAW**-approach as explained above. What should be noted, though, is that different **PAW**-potentials do have slightly different recommended cutoff energies for the plane wave basis set.

Table 1: Element and its associated PAW-potential used for the calculations (names as found in VASP's POTCAR file, line starting with PAW_PBE). For most of the calculations the normal potentials were used, the soft (_s) and hard (_h) potentials were utilized only for benchmarking purposes (see chapter 5.6).

| Element | PAW-potential names: PAW_PBE... | | |
|---------|---------------------------------|---------------|---------------|
| | normal | hard | soft |
| Au | Au o6Sep2000 | | |
| S | S 17Jan2003 | S_h o8Apr2002 | |
| C | C o8Apr2002 | C_h o6Feb2004 | C_s o6Sep2000 |
| H | H 15Jun2001 | H_h o6Feb2004 | |
| F | F o8Apr2002 | F_h o6Feb2004 | F_s o6Sep2000 |

These cutoff energies highly depend on whether one uses soft, standard or hard PAW-potential for an element, going from low to high cutoff energy recommendation in this order. For a calculation the highest value of the cutoff energy of all used PAW-potentials needs to be used. Furthermore, only calculations for which the same cutoff energy was used are comparable. So the inevitable factor which affects the computational cost is the cutoff energy used for the plane wave basis set during the calculations.

What also does have quite an impact on the computational cost, especially the memory needed to do the calculations, is the number of k-points (see chapter 2.2.2) used for the calculations.

3.1.1 VASP and GADGET: a powercouple

For finding the minimum on the energy surface GADGET [92] was used, which is a python-based tool for geometry optimization. Using GADGET in conjunction with VASP bears significant advantages, most notably that it is possible to better optimize the geometry of long, upright standing molecules. This is due to GADGET using delocalized, internal coordinates instead of Cartesian coordinates, utilizing a geometrical direct inversion in the iterative subspace (DIIS) based method. Treating the atoms of the adsorbate molecule in these internal coordinates allows the atoms of the molecule to relax in a more realistic way, which would not happen in Cartesian coordinates because the absolute displacement of an atom would be too much to change, e. g., the tilt of the molecule. Furthermore, GADGET provides advanced algorithms for the initial guess of the Hesse matrix, which provides means to enhance the convergence of the geometry optimization a great deal. For this work, Fischer's model [93] was used for initializing the Hesse matrix. A complete summary and detailed explanation of how GADGET can be found in the work of Bučko et al. [92]. As GADGET is a tool for optimizing the geometry of a system, it hands the improved geometry file over to VASP, which does the DFT-calculations.

The principal process is as follows: First, a **DFT**-calculation is done by **VASP**. If this is converged, **GADGET** does a geometry optimization of the system and starts another **VASP**-calculation. This is repeated until convergence is reached.

3.1.2 Selected *INCAR* tags

In the following paragraphs a description of the most important **INCAR** tags for **XPS** calculations will be given; a complete **INCAR** file as used in the course of this thesis can be found in appendix [a.1](#). A nice explanation of the most important tags for setting up standard **VASP** calculations, as well as a short description of the needed input-files for **VASP** and **GADGET** can be found in, e. g., chapter 3.2 of Elisabeth Wruß's diploma thesis [94].

The following paragraphs are meant for readers who already have some basic understanding of how to do calculations with **VASP**, as the following information is of quite technical nature.

When doing **XPS**-calculations the **ICORELEVEL** tag is one of the most important ones. It is set to either 1 or 2, depending on whether one wants to utilize the initial or final state method, respectively.

Using the initial state method is rather straightforward and computationally not noticeably more costly compared to a standard **DFT** calculation done by **VASP**. This is due to the fact that it just recalculates the Kohn-Sham eigenvalues of the core levels after the self consistent field calculation is converged (see chapter [2.2.6](#)).

Doing final state calculations is a little bit trickier, because there some obstacles have to be overcome. When applying the final state method, selected electrons are moved from the core into the valence band, effectively increasing **NELECT**¹. Telling **VASP** to do a final state calculation is done by setting **ICORELEVEL** = 2 and, additionally, **CLNT**, **CLN**, **CLL**, and **CLZ** need to be defined correctly. **CLNT** specifies the number of the species to calculate the final state for as defined in the **POSCAR** file, i. e., the atom(s), whose electron should be excited, needs to be stated explicitly in the **POSCAR** file. The tag **CLN** is used to set the main quantum number of the electron to be excited, and **CLL** the *l* quantum number of it, e. g., setting **CLN** = 1 and **CLL** = 1 will treat the 1s orbital electron in the final state approach. Finally, the option **CLZ** provides the possibility to define how many electrons are excited, i. e., it is possible to also excite fractions of an electron to do a Slater-Janak transition state calculation (see chapter [2.2.7.2](#)), for example. Furthermore, a couple of caveats still apply to the final state method, to quote the **VASP** manual²:

Several caveats apply to this mode. First the excited electron is always spherical, multipole splitting are not available. Second, the other core electrons are not allowed to relax, which might cause a slight error in

¹ Total number of electrons, normally determined automatically by **VASP**, but can be set manually as well.

² <https://cms.mpi.univie.ac.at/vasp/vasp/vasp.html>

the calculated energies. Third, absolute energies are not meaning full, since VASP usually reports valence energies only. Only relative shifts of the core electron binding energy are relevant (in some cases, the VASP total energies might become even positive).

3.1.3 *Hands on notes*

This is another quite technical section, meant as some kind of checklist for VASP and GADGET users. If using these two programs, one should keep certain things in mind to produce meaningful results.

First of all, one should check all input files for consistency. Furthermore, when doing slab-type DFT-calculations, the POSCAR file of your starting geometry should be selective, i. e., most of the substrate atoms are fixed and only the two uppermost layers are movable. This strategy lets the two topmost layers relax to adapt to the SAM on top of it and the bottom three layers staying in place, representing the gold bulk. One has to do this to avoid spurious surface relaxations at the bottom side of the surface slab, which, due to periodic boundary conditions, is exposed to the vacuum gap (see chapter 3.1.4). Additionally, one should check the degrees of freedom during the calculation if using GADGET - this is done via commandline with `grep htest report`. The number shown has to be equal to the number of movable atoms (vide supra) times three (for translations along x, y and z axis). The correct degrees of freedom are important to ensure that the substrate detection of GADGET worked correctly. The aforementioned substrate detection is a routine GADGET uses to automatically determine which atoms of the unit cell are part of the substrate and which belong to the covalently bonded molecule. To correctly detect the molecule is important for the geometry optimization GADGET utilizes.

3.1.4 *Putting atoms in a box*

The first step to actually doing simulations is to define the system of interest in a way a computer program is able to understand it, i.e. to produce an appropriate input file containing the system's unit cell. There are some things to keep in mind when constructing a unit cell for simulating a SAM on a substrate using VASP.

First of all, VASP applies 3D periodic boundary conditions to the supplied unit cell, but when modeling a surface, only periodic boundary conditions in two spatial directions are applicable. The technique used to accomplish this is called repeated slab approach and the basic principal of it is shown in figure 5. Therefore, one has to decouple the system in z-direction to effectively get an infinite 2D-layer, which still gets repeated for the calculations in the third direction, but only interacts in two directions. To accomplish this, two steps are necessary: First, a vacuum gap has to be added to the top of the unit cell to prevent quantum mechanical interaction in z-direction. As a second step, the system needs to be decoupled electrostatically by

introducing a self-consistent dipole layer at the top of the unit cell to compensate for any induced dipole of the system.

Finally, for this work, the unit cell should be based on experimental findings, after all, we want our results to be as realistic as possible to provide new insights and to be able to fundamentally understand and better interpret experimentally measured data points. For reading more about the not always straightforward task of finding the right unit cell, please refer to chapter 5.1 of this thesis.

3.1.5 *Optimizing the system*

The first step when doing calculations containing a substrate, is to optimize its lattice constant with the chosen exchange-correlation functional and the PAW-potential which will be used for this element. Optimizing the lattice constant should be done to avoid spurious geometry relaxations at the surface. Furthermore, using the experimentally measured one for simulations will generally not produce the energetically most favorable system. This is due to the fact, that the optimal lattice constant for modeling a chosen crystal structure depends on the potentials used for the element(s) of the crystal. Finding the optimal lattice constant is done by starting with a unit cell of a bulk of the material used for the slab later on, built with the experimental lattice constant. The size of this unit cell is then gradually changed, calculating the system energy for each unit cell, fitting a parabola and finally choosing the lattice constant which yields the lowest energy. For this procedure, at least a two-step approach should be realized. It is advisable to start with a rather big step size and refine it to much smaller values in the vicinity of the probable optimum.

For the Au substrate used during the course of this theses, the optimization of the lattice constant was already done by one of our group members, Elisabeth Wruß, and was determined to be 4.141 Å, which fits the measured (4.062 Å) and calculated values (4.154 Å) reported in literature [95] quite well.

The next step is to create a metal surface using these optimized lattice constants. The substrate used in the course of this thesis consists of five layers of gold with a Au(111) surface, of which the topmost two layers were allowed to relax and the bottom most three layers were kept fixed, resembling the gold bulk.

On top of this substrate the molecule(s) of interest are placed, putting the docking atom at an appropriate place. In this case, the sulfur atom was placed at a fcc hollow site of the Au(111) surface, though during geometry optimization it moved towards the bridge position. The alkyl chain was set to a commonly observed tilt angle of around 35 °C. One of the main advantages about using VASP in conjunction with GADGET is the fact that it is possible to tilt and bend such long, upright standing molecules to find the energetically most favorable geometry during the simulations. Non the less, typically only a local minimum is found.

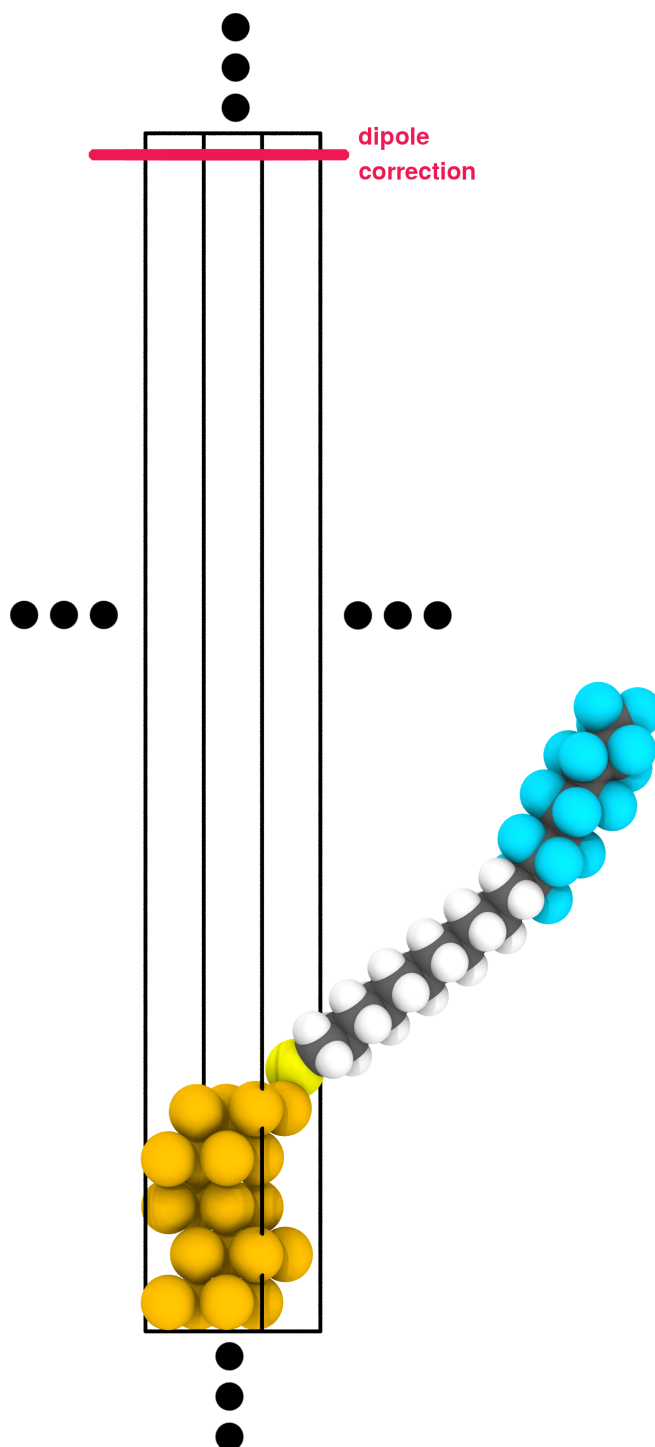


Figure 5: Schematic picture of a unit cell used for repeated slab approach calculations. One can see three dots next to the unit cell, which indicate the applied periodic boundary conditions in every spatial direction. The pink line at the top symbolizes the applied dipole correction by [VASP](#), which decouples the unit cell in z-direction electrostatically. The space on top of the molecule is added to introduce a vacuum gap, making sure that the system does not interact between unit cells quantum mechanically in z-direction, therefore completely separating the system in z-direction. This means, the periodic boundary conditions are effectively applied in two dimensions only, resulting in a repeated slab in the third dimension.

3.2 SCREENING EFFECTS

Due to fundamental electrostatics one has to take screening effects into account when the energy of an electron, which gets ejected next to a conducting solid is of interest. This means, when an electron is ejected from a core level, it needs to overcome two potentials: First, the potential of the SAM in its ground state as it is calculated in the combined system. Second, the mirror image potential which models the dielectric screening as explained above. This is schematically shown in figure 6. Classical screening can be described with the help of instantly created mirror charges in the metal, which influence the electron in question. For the initial state approach, a zeroth-order approximation of screening effects can be done via considering the Coulomb-screening of the metal. A quantum mechanical, non-classical treatment of screening would be explicitly considered in the final state approach, but this comes hand in hand with several drawbacks of this method as is explained in chapter 2.2.7.2.

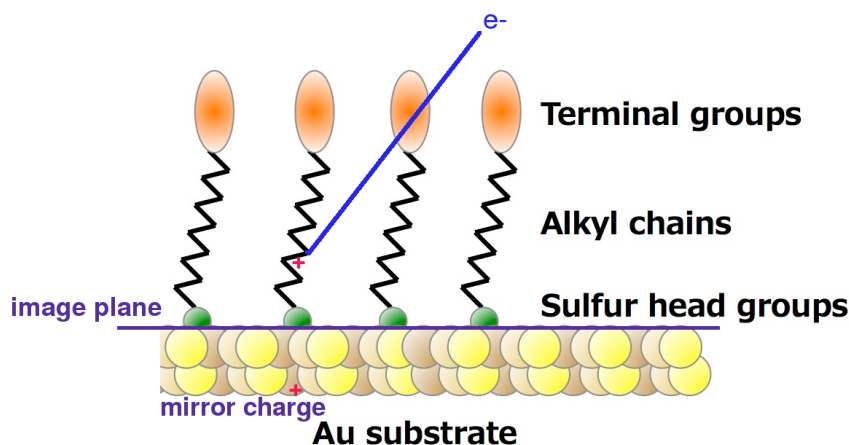


Figure 6: Schematic drawing of a SAM on a metal substrate in which an electron gets ejected. The positive hole created by this excitation process induces an instant mirror charge in the substrate. This is the principal process of an image charge creation in the metal upon excitation of an electron. Image modified from [96].

To take the polarization from the metal substrate into account, one has to calculate the energy of a point charge with respect to the image plane according to the Coulomb-interaction. The image potential affects the atoms closest to the substrate the most and shifts the core-level energies to less negative values,

$$\epsilon_{\text{Cl}s, \text{screened}} = \epsilon_{\text{Cl}s} + \frac{1}{4 \epsilon |z - z_0|} \quad (23)$$

where ϵ is the dielectric constant of the SAM and z_0 refers to the image plane position, which was set to 0.9 Å above the average z -position of the top gold layer [97, 98].

What should be mentioned, though, is the fact that, overall, electrostatic screening of the metal does not play an important role in the case of XPS-measurements of long, upright standing molecules. As can be seen in figure 7, only the core levels of the bottom most atoms are influenced by the electrostatic screening of the metal

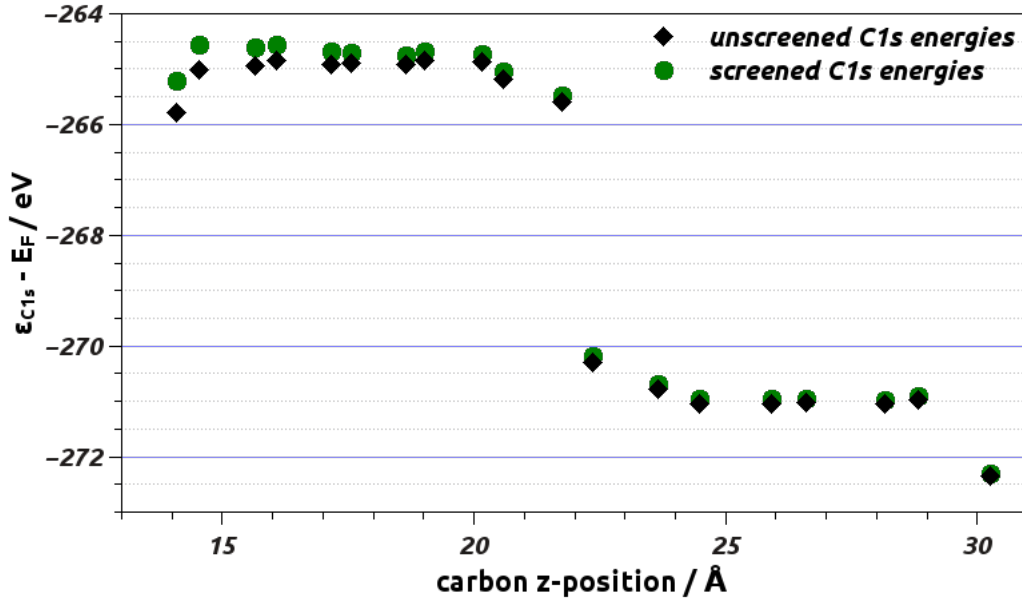


Figure 7: Core-level energies as calculated (C1s) in the initial state approach and with electrostatic screening effects (see main text) considered (C1s screened) of a F8H₁₁SH-SAM on a Au(111) substrate.

substrate. The further away an atom is situated in the molecule, the less it is affected by it. As a consequence, it does not have a great impact on the XP-spectrum, which is mostly shaped by the topmost atoms as XPS is a quite surface sensitive measurement technique.

3.3 BROADENING DELTA PEAKS

To compare theoretical orbital energies to experimentally acquired XP-spectra it is rather obvious that one has to find a way to generate a spectrum out of the individual core-level energies provided by DFT-simulations. This is done by broadening each delta peak with a Gaussian function - a Lorentzian or Voigt function would be equally suited for this kind of task, though.[99, 100] To generate the Gaussian curve a variance of $\sigma^2 = 0.1$ was chosen and the center of the function was set to the respective core-level energy, because the center of the Gaussian peak should coincide with the orbital energy calculated by VASP. This yields the following function:

$$g_i(x) = a \exp\left(-\frac{(x - \mu)^2}{2\sigma^2}\right) \quad \text{with} \quad a = \frac{1}{\sigma\sqrt{2\pi}}. \quad (24)$$

Subsequently, one has to sum over all the individual Gaussian curves of the contributing core levels (see chapter 3.5) to create a spectrum of the molecule under investigation. To illustrate this broadening, figure 8 shows the case for the F8H₁₁SH-

SAM on a Au(111)-surface; for the other two molecules a similar picture evolves - only the height of the peaks differ slightly.

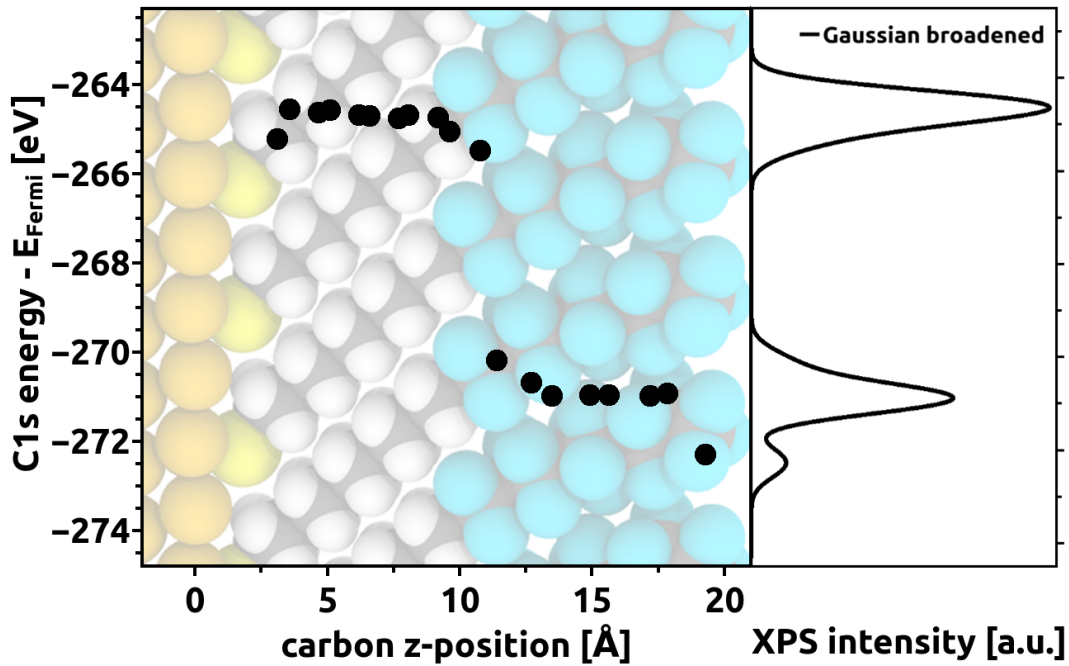


Figure 8: Preliminary spectrum (right) of a Au(111)/F8H11SH SAM generated out of calculated orbital energies (left) by utilizing a Gaussian function (see equation 24) for each orbital and summing over the individually created peaks. The spectrum was generated without any damping (cf., chapter 3.4) applied.

3.4 DAMPING

Another crucial point when creating a spectrum out of delta peaks is to consider the surface sensitive nature of XPS. This means, one has to take, i. a., inelastic collisions, recombinations or the trapping of the electron on its way out of the sample to the detector into account. This can be done by introducing an exponential attenuation function to account for the finite escape depth of the photoelectrons.[101] These exponential attenuation function acts as a weighting factor for each Gaussian peak of an atomic orbital contributing to the spectrum and, therefore, is multiplied by its intensity. The individual weighting factors w_i depend on the vertical distance d of atom i to the topmost layer of atoms in the SAM and the energy of the escaping electron E_{kin} , so the complete function to generate the individual damping factor for each Gaussian peak (see chapter 3.3) is:

$$w_i(d, \epsilon) = \exp\left(\frac{-d_i}{0.3 \cdot E_{kin}(\epsilon_i) \cdot e^\beta}\right), \quad (25)$$

where β is an empirical attenuation factor chosen to reproduce the experimentally acquired peak heights and E_{kin} depends on the energy of the incident photon minus the binding energy of atom i in question - in this thesis the C 1s orbital energy as

calculated by DFT. In the measurements [53] which are used to benchmark the modeled spectra against, an incident photon energy of $E_{inc} = 580$ eV was used in the synchrotron experiments.

To illustrate the damping a SAM consisting of long, upright standing molecules was taken as used throughout this thesis. A more detailed explanation of these systems can be found in chapter 4. The three peaks in figure 9 are due to the CF_3 -atom at the top of the molecule (left peak, not damped), a fluorinated carbon chain of eight atoms (middle peak) next to it, and, an alkyl chain consisting of eleven atoms (right peak). As one can see in the aforementioned figure the damping is, naturally, quite significant, reducing the peak intensity of the alkyl chain at the bottom of the molecule to about a third compared to its original height (right peak).

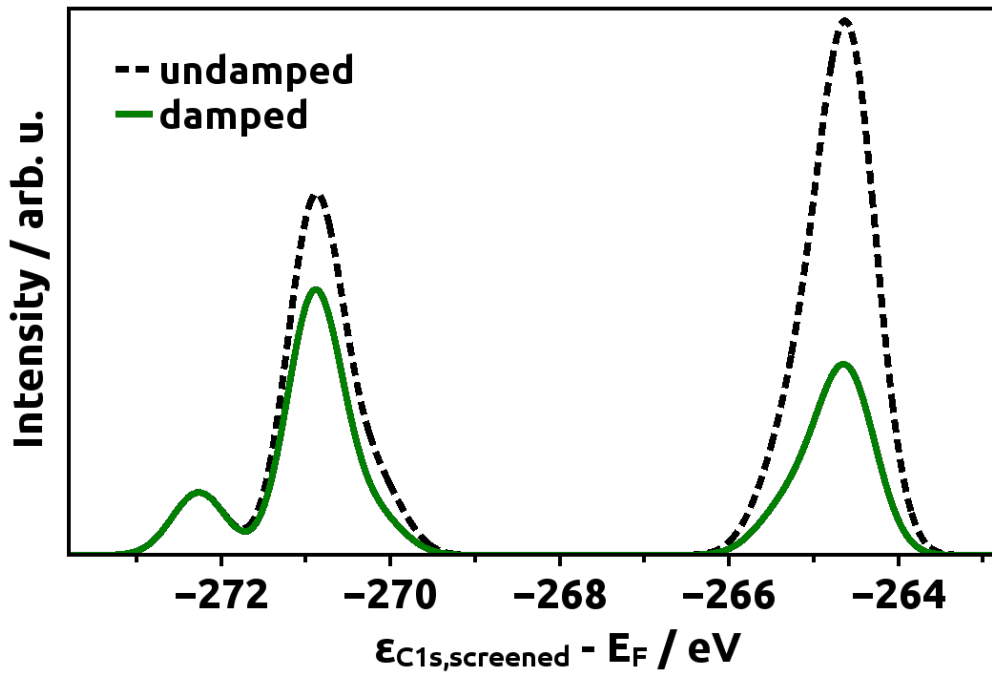


Figure 9: Damped (red, solid line) and undamped (black, dotted line) spectrum calculated utilizing the enhanced initial state approach of a full coverage $\text{F8H}_{11}\text{SH-SAM}$ on a $\text{Au}(111)$ -substrate.

3.5 CREATING THE SPECTRUM

To get the final spectrum, one has to sum over the individual contributions of each core level after being broadened (see chapter 3.3) and damped (see chapter 3.4) accordingly. This can be described by the following formula:

$$s = \sum_i w_i(d, \epsilon) \cdot g_i(\epsilon) \quad (26)$$

where s denotes the complete spectrum, w_i are the individual weighting factors as given in equation 25 with the distance to the surface of the SAM and the binding

energy of the core level as input and $g_i(\epsilon)$ denotes the Gaussian broadening as described in equation 24 depending on the energy of the core level.

3.6 SHIFTING AND STRETCHING

When looking at spectra created with DFT they look qualitatively the same as the ones measured via XPS. When showing both spectra in the same plot, they have to be shifted and stretched to lie on top of each other. This procedure does not change the results in a qualitative way by any means, but only makes them comparable quantitatively as well. In figure 10 a DFT-spectrum of the F8H11SH-system is shown, which is only rigidly shifted by 20.3 eV to lie on top of the experimentally measured one, but not stretched at all, and one can see that the same trends are observable.

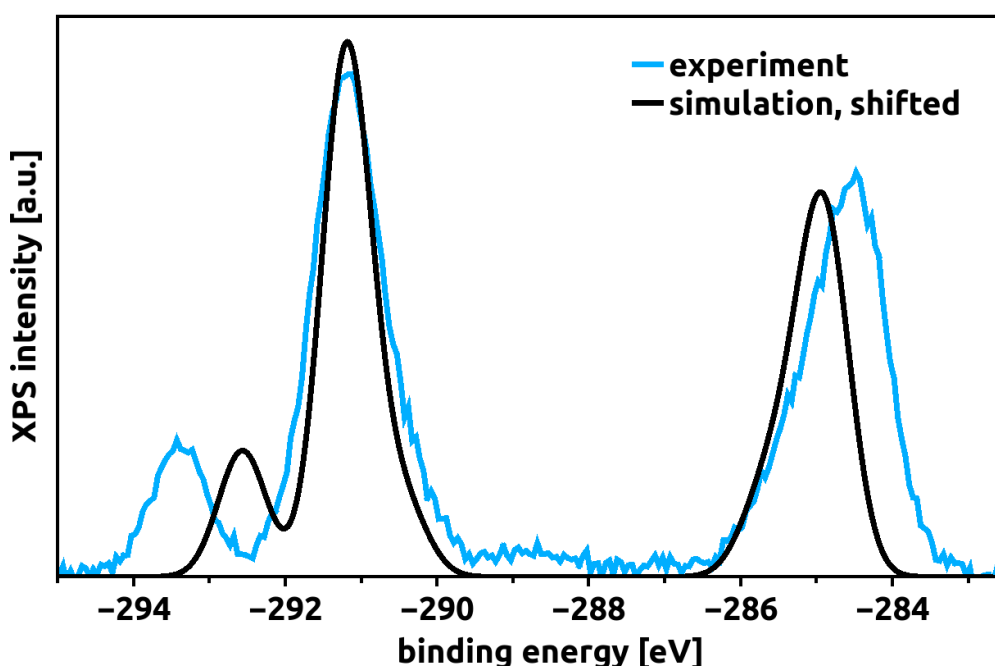


Figure 10: Experimentally measured HRXPS-spectrum of a F8H11SH-SAM on a Au(111) surface (blue) and the same system modeled with DFT on top of it (black). The calculated spectrum is shifted by -20.3 eV to align it to the main peak. The HRXPS-spectrum was acquired with an incident photon energy of 580 eV and is reprinted (adapted) with permission from [53]. Copyright (2013) American Chemical Society.

The shifting is done because the absolute Kohn-Sham orbital energy values calculated by DFT have only a limited significance, and, therefore, the calculated peaks of the core levels need to be shifted for better matching the experimental ones. Furthermore, to get an even better agreement with experiments, the spectrum needs to be stretched, which is also a common procedure when modeling ultraviolet photoelectron spectroscopy (UPS) measurements, i. e., comparing Kohn-Sham orbital energies close to the Fermi level to experimentally measured binding energies of valence electrons.[102]

INVESTIGATED SYSTEMS

When establishing a new approach it is always important to have reliable data to benchmark it against. In this case of the enhanced initial state method with which XPS spectra are modeled, it is crucial to have reliable XPS measurements of extensively characterized SAMs. Following the work of Lu et al. [53] I focused on three model systems for this thesis. The investigated SAMs belong to a very well established and thoroughly characterized type, namely substituted alkyl thiolates on Au(111). The molecules in question consist of an alkyl spacer of eleven carbon atoms, which is bonded via a sulfur atom to the substrate and is terminated with a fluorinated end group varying in length.

The IUPAC-names of the chosen molecules are 12,12,13,13,14,14,15,15,16,16,17,17,17-tridecafluoroheptadecane-1-thiolate (F6H11SH), 12,12,13,13,14,14,15,15,16,16,17,17,18,18,-19,19,19-heptadecafluorononadecane-1-thiolate (F8H11SH) and 12,12,13,13,14,14,15,15,-16,16,17,17,18,18,19,19,20,20,21,21,21-henicofluorohenicosane-1-thiolate (F10H11SH) and their lewis formulae are shown in figure 12, where it can easily be seen that the molecules differ only in having six, eight or ten fluorinated C atoms.

In figure 11 the experimentally acquired spectra (black line) of the F8H11SH system is shown, which is used to illustrate the following assignment of the five peaks to five different chemical neighborhoods of the molecule:

The terminal carbon atom, which bonds to three fluorine atoms gives rise to the most negative binding energy peak at approximately -293.43 eV (violet). Adjacent to it, the fluorinated alkyl chain with two fluorine atoms per carbon atom produces the most prominent peak at about -291.23 eV (green). This peak has a weak shoulder at around -290.68 eV, which is due to the very last carbon atom of the fluorinated part (yellow), located right next to the alkyl chain, which is, therefore, chemically shifted. The third clearly distinct peak, again with a slight broadening seen at one side (this time due to the very first carbon atom of the alkyl chain next to the fluorinated chain) is visible at -284.48 eV (red). The aforementioned broadening expands the peak to more negative values (at around -285.33 eV, dark blue). In passing it is noted that the bottom most carbon atom is also chemically shifted due to the influence of the docking sulfur atom, which can be seen in the calculated data, but is not detectable in experiments, because of the finite escape depth of the electrons.

A color coded chemical structure of all three used systems is given in figure 12. For a more detailed explanation of the experiments to which this theoretical work relates, the interested reader is referred to the paper of Lu et al. [53].

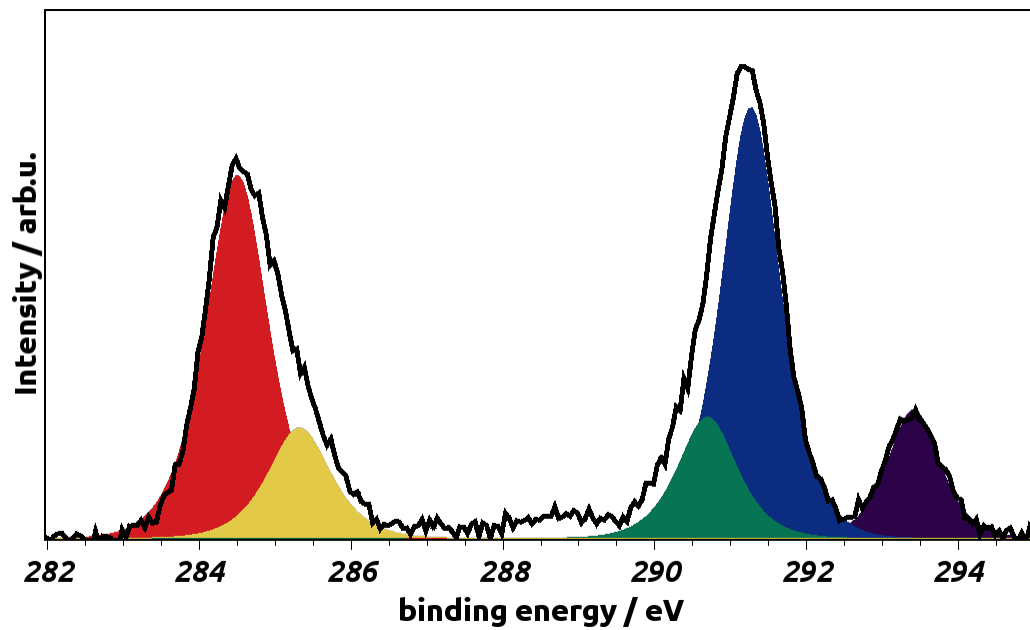


Figure 11: C1s HRXP-spectrum [53] (black line) of a full coverage F8H₁₁SH-SAM on Au(111) measured with an incident photon energy of 580 eV. The spectrum is decomposed into five Gaussian peaks within a fitting procedure. The assignment of these peaks is discussed in detail in the main text.

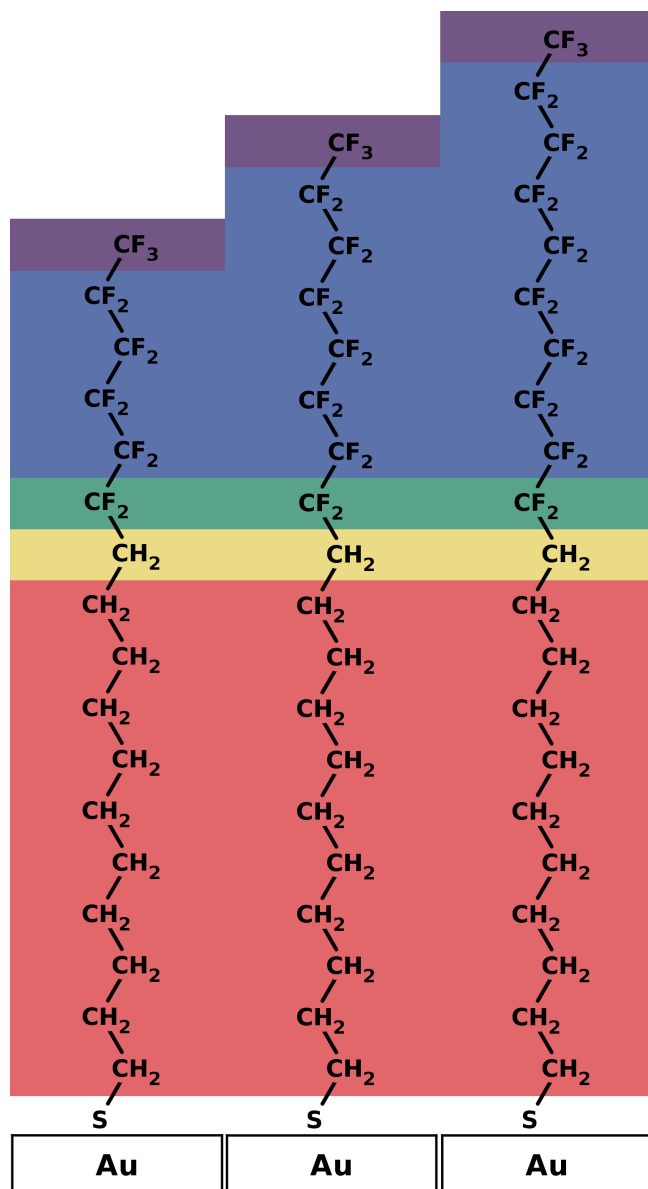


Figure 12: Chemical structures of F₆H₁₁SH (left), F₈H₁₁SH (middle) and F₁₀H₁₁SH (right). The different background colors refer to C atoms with chemically clearly distinct environments.

4.1 FULL COVERAGE SYSTEMS

For benchmarking the enhanced initial state approach, the full coverage $\text{F8H}_{11}\text{SH-SAM}$ -system was used. The unit cell for these simulations is depicted in figure 13.

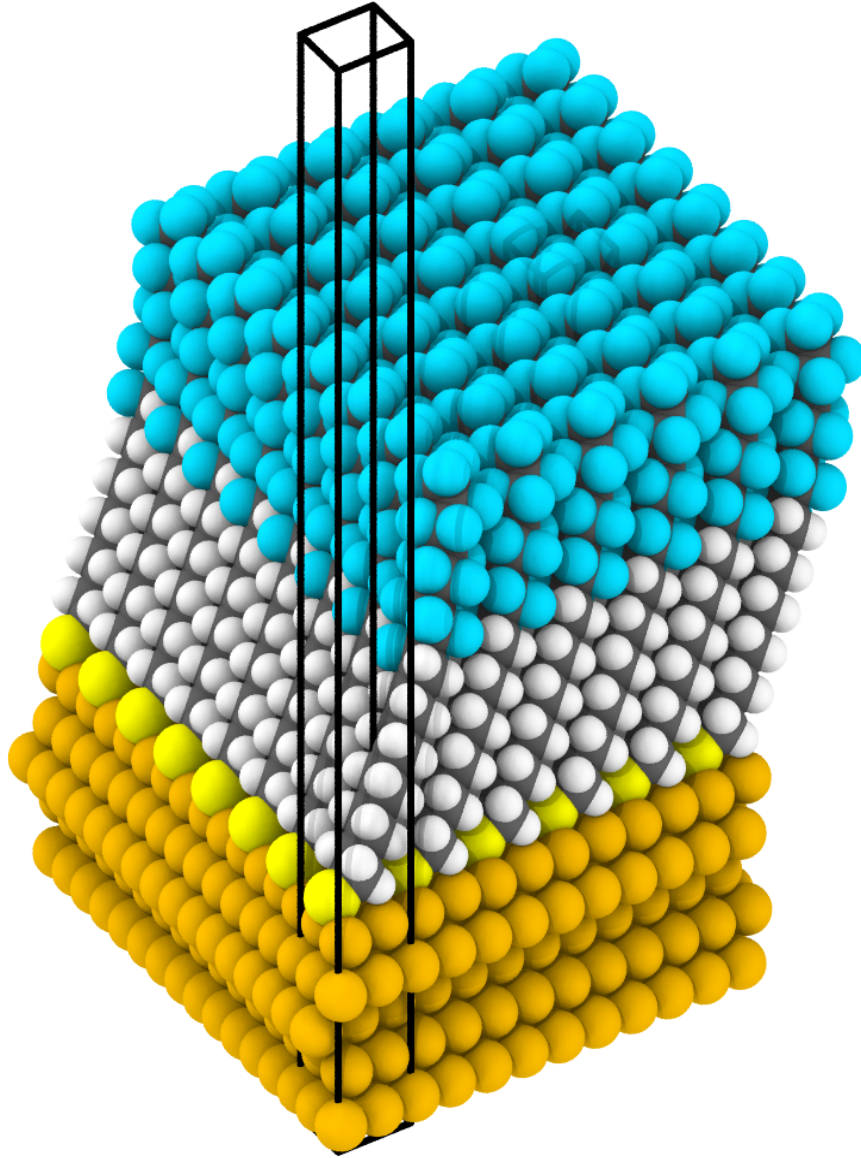


Figure 13: Schematic 3D view of the full coverage unit cell (depicted by the black parallelepiped) of the $\text{Au}(111)/\text{F8H}_{11}\text{SH}$ interface before optimization, indicating the applied periodic boundary conditions used in the simulations. Taken from [52].

As will be discussed in chapter 5.1, there are several experimentally proposed unit cells, a top view of the one chosen here is shown in figure 14. In the final calculations one molecule per unit cell was used, the hexagonal lattice introduced by the periodic boundary conditions can be seen in the aforementioned figure. This can be explained when looking at the molecule, where several parts prefer a different structure. First of all, the thiols used as a docking group prefer to adsorb in a hexagonal lattice on a $\text{Au}(111)$ surface. In contrast to that, alkyl molecules normally assemble in a

herringbone structure. The fluorinated segment prefers again a hexagonal lattice due to its helical structure.

The 3D view of the unit cell shown in figure 13 belongs to the $F8H_{11}SH/Au(111)$ system, the one for the $F6H_{11}SH$ - and $F_{10}H_{11}SH/Au(111)$ system look almost identical, though, because only the length of the upper, fluorinated alkyl chain is extended. A more thorough discussion concerning the used unit cell can be found in chapter 5.1.

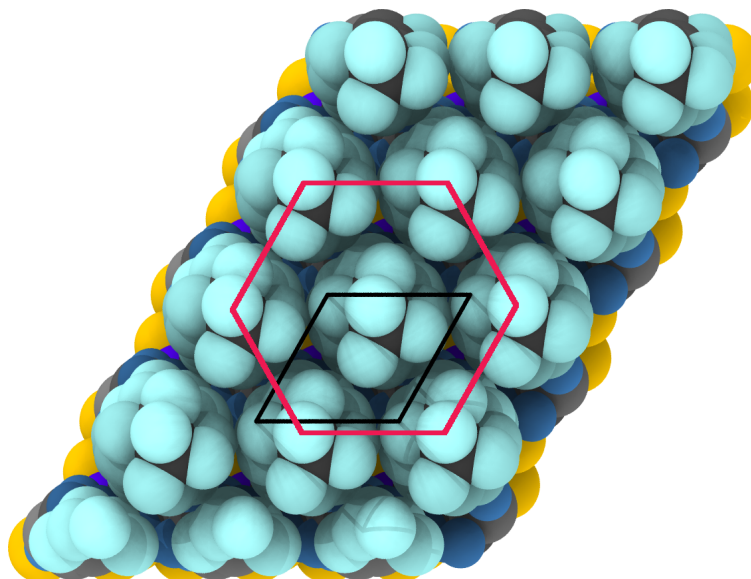


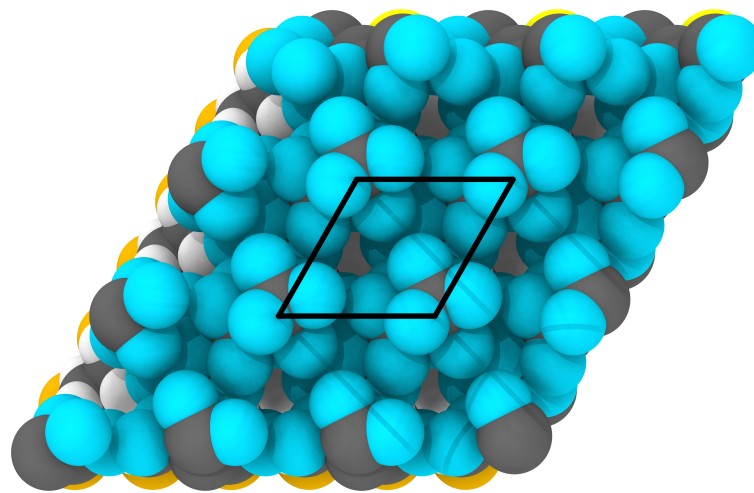
Figure 14: Top view of the used unit cell (black) with applied periodic boundary conditions in x- and y-direction. The pink overlay depicts the hexagonal symmetry found in experimental analysis.

4.2 LOW COVERAGE SYSTEMS

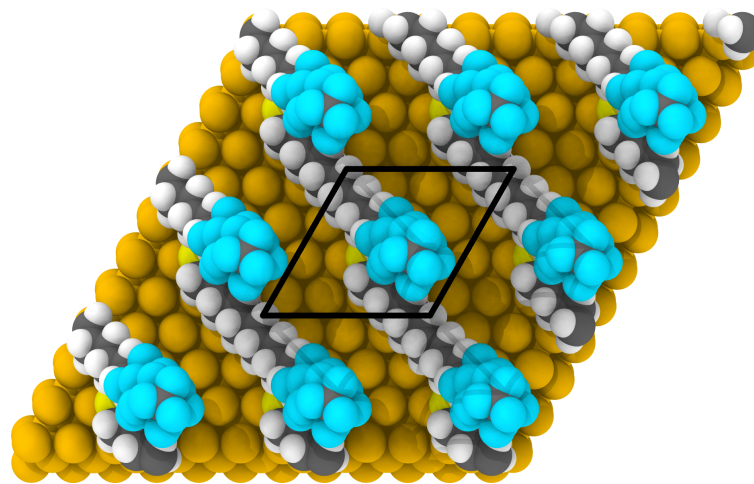
To show the influence of collective electrostatic effects (cf, chapter 5.5), low coverage systems were calculated and the shifts of the energy peaks were compared to the full coverage situation.

What should be noted is that for all the low coverage calculations the simulation process was adapted to fit the somewhat more theoretical assumption of the SAM in these cases. During these simulations the position of the molecule had to be fixed and the atoms were not allowed to move, because otherwise the whole molecule would have fallen down, creating a qualitatively completely different SAM compared to the full coverage case. Experimentally these kind of systems can be achieved only up to a certain degree by mixing non-substituted and partly fluorinated alkyl thiolates as, e. g., Ballav et al. [103] have done. Doing this still introduces an additional dipole layer due to the bond dipole, which arises because the electrons want to be localized more around the more electronegative of the two bonding atoms. This dipole layer is not present in the simulated system representing the single molecule limit (see chapter 5.5). To model the different low coverage systems, one molecule with the optimized geometry of the full coverage SAM was taken as-is and was put

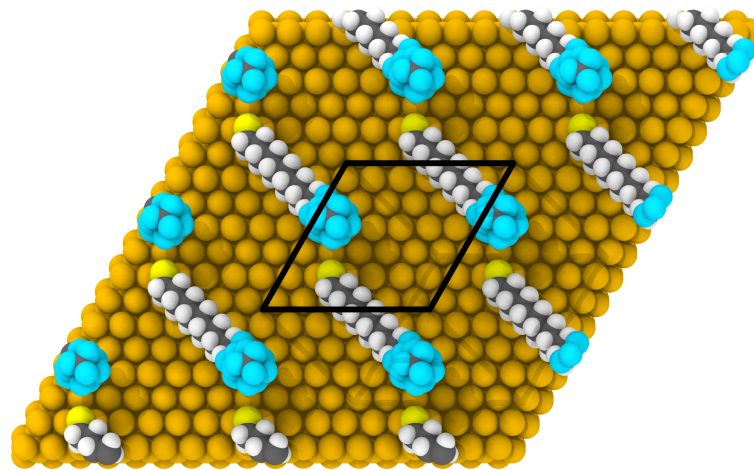
on a gold slab doubled, e. g., in x- and y-direction, i.e. being four times the size and, therefore, creating a unit cell with a coverage of a quarter. The same procedure was used to create the unit cell with a coverage of $1/9$, i. e., one molecule was put on a gold slab being three times the size in x- and y-direction compared to the full coverage slab. The number of k-points was adapted accordingly when changing the size of the unit cell to keep the k-point density the same. For the full coverage system a Γ -centered k-point grid of $8 \times 8 \times 1$ in x-, y-, and z-direction, respectively, was used (cf., chapter 2.2.2). For the coverage of a quarter the k-point grid was adjusted to $4 \times 4 \times 1$ kpoints in x-, y-, and z-direction, respectively. For the single molecule limit, i. e., a coverage of $1/9$ two k-points were used in the x- and y- direction and one in z-direction. The unit cells created for different coverages, starting from full coverage to the single molecule limit, are shown in figure 15.



(a) Full coverage.



(b) 1/4 coverage.



(c) 1/9 coverage.

Figure 15: Top view of the four unit cells with different coverages with applied periodic boundary conditions in x - and y -direction (three times each), starting with full coverage (a), a coverage of $1/4$ (b) and a coverage of $1/9$, which represents the single molecule limit (c). The black box indicates the actual unit cell and is created by doubling the full coverage unit cell in x - and y -direction, respectively and subsequently deleting all but one molecules in it.

MODELING X-RAY PHOTOELECTRON SPECTRA OF PARTLY FLUORINATED ALKYL THIOLATES

Modeling X-ray photoelectron spectra of partly fluorinated alkyl thiolates In the course of this thesis it is shown that **DFT** based methods can not only be of enormous use to interpret **XP**-spectra, but also provide new insights, which can not be accessed experimentally.

Overall, a quite good agreement is achieved between simulation and experiment which shows that the presented methodology for modeling **XP**-spectra is capable of describing photo-emission shifts of chemical and electrostatic nature in **SAMs**, and, therefore, is a valuable tool for the scientific community.

The theoretically acquired results match the experimentally measured data quite well as one can see in figure 16, where the calculated core-level energies are displayed alongside the modeled spectrum and the data obtained via **HRXPS**-measurements. What should be noted is that the absolute values of the calculated core-level energies via **DFT** do not fit quantitatively very well to experiments, but rather the core-level energy shifts do.[45, 84, 104, 105] Therefore, the core-level energies are reported in the left scatter plot as calculated, but the spectrum in the right panel was stretched by a factor of 1.15 and, subsequently, shifted by 20.1 eV to align it with the **XP**-spectra. Doing so only improves the quantitative agreement with experiments (see chapter 3.6), but is by no means necessary for producing results which represent the experimentally measured trends.

If one wants to better understand the experimentally acquired data, a smart way is to do some modeling and compare these results to the measured ones. The results acquired in the course of this thesis show that shifts in **XP**-spectra of **SAMs** are not only due to atoms in a chemically different neighborhood, but also collective electrostatic effects in the adsorbate layer have to be taken into account. These electrostatic effects arise on one hand from arrays of dipoles, originating from interfacial charge rearrangements between the substrate and the adsorbate layer due to the bonding group. On the other hand, they are due to polar segments in the adsorbate molecule itself in the case of an ordered, densely packed film.

Looking at the presented system (see chapter 4) one can see that there are some details in the simulation, which are not resolved in experiments, e. g., the shifted core-level energy of the carbon atom bonded to the sulfur atom. Furthermore, it is possible to reveal a slight shift to less negative core-level energies of the carbon atoms as they get closer to the metal substrate due to screening effects (see chapter 3.2). These two effects can not be seen in experiments because of the limited resolution and the strong surface sensitivity of **XPS**-measurements due to the strong attenuation (see chapter 3.4) of photo-electrons probing atoms far from the surface.

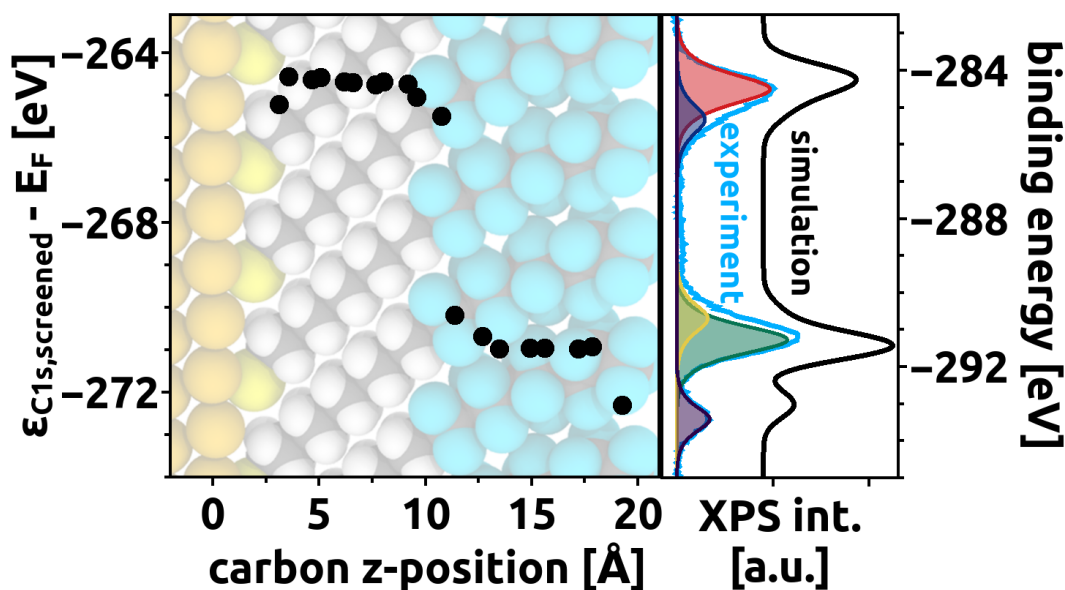


Figure 16: DFT-calculated (screened) C 1s core-level energies relative to the Fermi energy for each carbon atom in a full coverage F8H11SH-SAM (left panel). The right panel shows the XP-spectrum calculated from the individual C 1s energies of the SAM (black). Additionally, the measured HRXP-spectrum [53] of a full coverage F8H11SH-SAM on Au(111) is shown (light blue). The measurements were performed with an incident photon energy of 580 eV. Five Gaussian peaks are fitted to the measured spectrum; the assignment of these peaks is discussed in chapter 4. While the core-level energies in the left panel are reported as calculated, the simulated spectrum has been stretched by a factor of 1.15 and subsequently shifted by 20.1 eV (binding energy = $1.15 \cdot [\epsilon_{C1s,screened} - E_F] + 20.1$ eV). As a consequence of that the left and right scales do not cover the same range of values. Taken from [52].

In the following chapters the aforementioned effects as well as various other interesting aspects for modeling the systems discussed in chapter 4 and XP-spectra in general are presented. Several aspects of the different SAMs are investigated, the physical theories applicable for modeling thin layers on metal substrates are explained and, finally, also computational problems arising are discussed.

5.1 FINDING A SUITABLE UNIT CELL

Literature suggests different types of suitable unit cells for SAMs of fluorinated alkyl thioliates on gold, namely, $p(2 \times 2)$, $c(7 \times 7)$ or even incommensurate ones.[53, 106–109] Because the reported experimental unit cells for partly fluorinated alkyl thioliates were not consistent, quite a lot of different unit cells were tested in the course of this thesis. For this, various unit cell sizes (with different unit cell vectors, and, consequently, also a different number of surface atoms) were tested, meaning different areas per molecule were probed to find the correct one. Starting from unit cells which were reported for alkyl thioliates on gold to ones suggested for fluorinated alkyl thioliates

specifically (vide infra), various unit cells were tested in the course of this thesis. Furthermore, several different configurations with one, four and even nine molecules in one unit cell were tested, using slightly different packing densities of the SAM, i. e., different areas per molecule. This task proved to be rather cumbersome, because quite a lot of calculations did not converge, but a suitable unit cell (vide infra) was found in the end.

An overview of the different unit cells tested is given in table 2 and they are discussed from top to bottom in the following paragraphs. First, a $\sqrt{3} \times \sqrt{3}R30^\circ$ unit cell as is normally used with alkyl thiolates on a Au(111) surface was created with a lattice spacing of ca. 5 Å, which has three surface gold atoms per unit cell. This unit cell did not converge, probably because of the bigger fluorine atoms present in these molecules in contrast to the smaller hydrogen atoms in pure alkyl systems, having only a surface area per molecule of 22.27 Å².

Therefore, as a next step, four molecules were placed in a herringbone like structure, so they can arrange differently and pack more efficiently. Furthermore, herringbone like structures were also experimentally suggested for similar molecules. Unfortunately, these calculations did not converge at all. In one simulation the molecules did not even form a nice SAM but rather fell over and create some kind of *Gordian knot* as can be seen in figure 17.

As a next step, a unit cell was created where the lattice spacing was increased to 5.9 Å, resulting in a surface area per molecule of around 30 Å² to account for the bulkier fluorinated part of the molecule. This means instead of three surface gold atoms per molecule in the case of the small *alkyl* unit cell, four surface gold atoms per molecule were present in this unit cell.

Also a supercell consisting of nine molecules, arranged in a herringbone like structure, was tested, but again, VASP did not converge within several runs as started by GADGET. Furthermore, the size of this unit cell was on the edge of what was, computationally speaking, sensible to calculate.

Additionally, also tests at a sub monolayer coverage were done. For this, unit cells with a surface area of 89.03 Å² and even 120.77 Å² per molecule were constructed. In these cases the molecules assemble rather flat lying on the Au(111)-substrate and, therefore, are not comparable to the full coverage situation when probing them with surface sensitive techniques like XPS.

After several tests (with, i. a., differently created fluorine segments, cf., table 2) and careful considerations of all of the aforementioned unit cells and extended discussions [110] with our experimental collaborator Michael Zharnikov from University of Heidelberg and my supervisor Egbert Zojer we came to the conclusion to use the primitive 2x2 unit cell for this work.

The finally chosen p(2x2)-unit cell contains only one molecule - in contrast to 17 molecules in the case of the also experimentally proposed c(7x7) structure - which, additionally, has the advantage of being computationally way less demanding. The used unit cell has a molecular footprint of 29.70 Å² per molecule - the same was

used for the **F6H₁₁SH**-, **F8H₁₁SH**- and **F10H₁₁SH**-system - which means the packing density is a little bit reduced compared to an alkyl-**SAM** due to the more bulkier fluorine atoms. The slight variations of the surface area per molecule as reported in table 2 are due to slightly different lattice constants, because the optimized one was not used from the beginning (vide supra). As already noted in chapter 3.1.5, the optimized lattice constant for the Au(111)-substrate modeled with **VASP** is $a=4.141$ Å. The unit cell as such was created with the atomic simulation environment [111] by selecting a Au(111)-surface slab and providing the lattice constants.

Table 2: Different unit cells containing one, two, four and nine molecules. The third vector z points always 50 Å in z -direction. Only the ones marked with an asterisk converged, though. The one marked with \times is the unit cell finally used (p2x2-final). It utilizes an optimized gold lattice spacing as discussed in 3.1.5. The ones marked with greek letters are various unit cells which were tested, but not used in the end for certain reasons (see main text). α unit cell created with a **F6H₁₁SH** and **F8H₁₁SH** molecule, respectively, each with a 10 and 20 degree helix, respectively; β unit cell with **F6H₁₁SH** and **F8H₁₁SH** molecules oriented differently on the surface (carbon chain tilted along x -axes and diagonally, respectively); γ only the **F6H₁₁SH** molecule was tested with this one, but with a 10 and 20 degree helix like structure, respectively; δ unit cells containing one **F6H₁₁SH**, **F8H₁₁SH** and **F10H₁₁SH** molecule, respectively, using the already optimized structure and placed in two different directions in the unit cell.

| unit cell | x / Å | y / Å | surface area per molecule | number of molecules |
|---|-------------|----------------|---------------------------|---------------------|
| $\sqrt{3}x\sqrt{3}R30\gamma$ | (5.07/0/0) | (2.54/4.39/0) | 22.27 Å ² | 1 |
| heringbone ^{*,α} | (8.78/0/0) | (0/10.14/0) | 22.27 Å ² | 4 |
| $\sqrt{3}x\sqrt{3}R30^{*,\alpha,\beta}$ | (5.90/0/0) | (2.95/5.11/0) | 30.15 Å ² | 1 |
| $\sqrt{3}x\sqrt{3}R30^{*,\alpha}$ | (11.81/0/0) | (5.90/10.23/0) | 30.20 Å ² | 4 |
| $\sqrt{3}x\sqrt{3}R30^\alpha$ | (17.71/0/0) | (8.86/15.34/0) | 30.19 Å ² | 9 |
| $\sqrt{3}x\sqrt{3}R30\gamma$ | (10.14/0/0) | (5.07/8.78/0) | 89.03 Å ² | 1 |
| $\sqrt{3}x\sqrt{3}R30^{*,\alpha}$ | (11.81/0/0) | (5.90/10.23/0) | 120.77 Å ² | 1 |
| p(2x2) ^{*,δ} | (5.77/0/0) | (2.88/5.00/0) | 28.85 Å ² | 1 |
| p(2x2)-final ^{*,\times} | (5.86/0/0) | (2.93/5.07/0) | 29.71 Å ² | 1 |

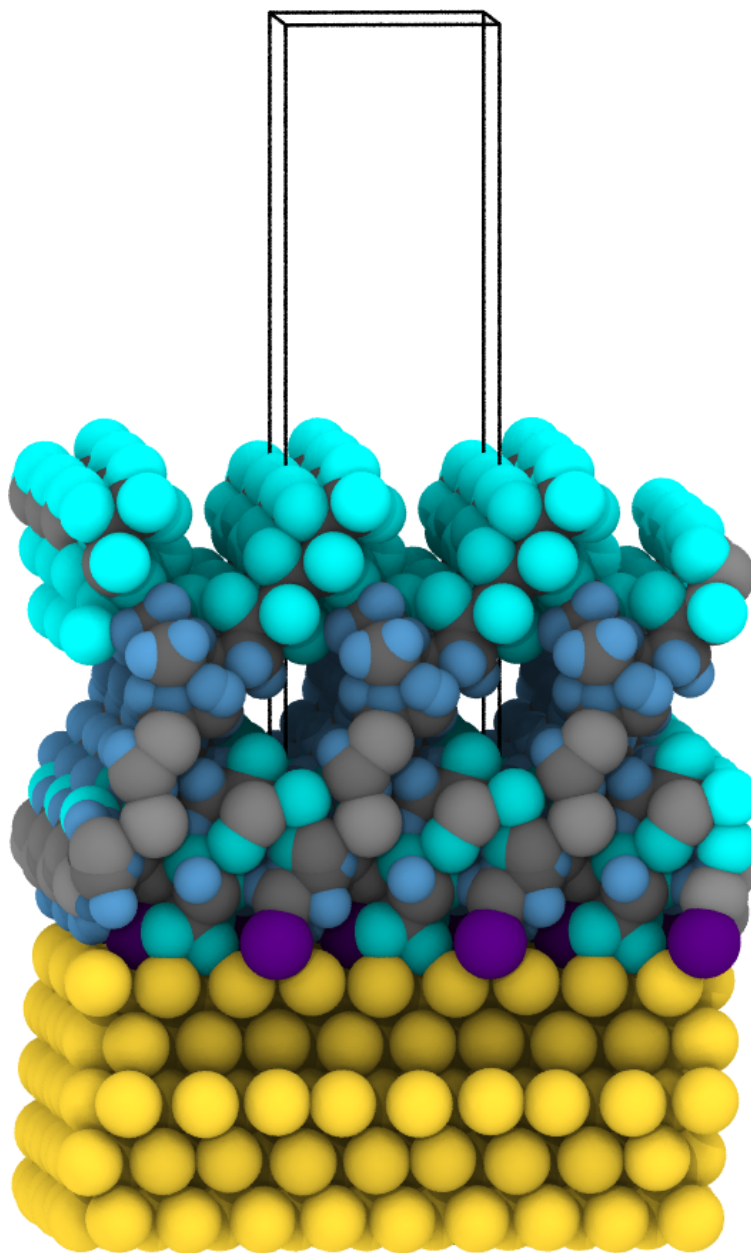


Figure 17: 3D view with periodic boundary conditions applied of a failed geometry optimization of two $F_6H_{11}SH$ molecules arranged in a pseudo-herringbone pattern on a $Au(111)$ -surface. One of the molecules fell down and, therefore, no ordered SAM of upright standing molecules was created.

5.2 A CLOSER LOOK AT THE FLUORINATED PART

Another point investigated was the helix like structure of the fluorinated part, which resembles the commonly known desoxyribonucleic acid (DNA) structure in some way, although it is not a double-helix, but rather one single rotated chain. To find the most probable structure, several starting geometries were prepared by hand with different degrees of rotation from one fluorinated C atom to the next. The systems compared were constructed with an initial rotation of ten and twenty degrees, respectively, and were then optimized with GADGET.

The starting geometry was set up as follows: The rotational axes was defined as the direction in which the zig-zag carbon chain points. This was achieved by creating a vector from the first carbon atom of the chain and the last odd c-atom in the chain, i. e., the last one at the same side of the zig-zag pattern. First, each carbon atom to be fluorinated was rotated with respect to this axes and the carbon atom right before it in the chain. Subsequently, all but the lowest carbon atom from the previous step were rotated until only the carbon atom at the top of the chain was rotated. This way, a helix like structure could be achieved.

The final geometry of the two system is shown in figure 18. What can be deduced from the aforementioned figure is, that the two systems most likely ended up in two different local minima, because of the quite different geometry that was produced during the optimization procedure. But as it turned out, there was neither a significant difference in total energy, which was basically identical differing only by 0.04 eV, nor in the core-level shifts, which were practically the same (with a difference of max. 0.09 eV). All calculated values of interest are given in table 3 and 4, respectively. This means, that the detailed geometry of the molecules in the SAM does not matter a great deal in this case for the specific properties investigated in this thesis.

Table 3: Total energy of systems calculated with a starting geometry created with a rotated fluorinated part by 10 and 20 degrees, respectively. Besides that, the exact same unit cell was used as a starting input for the geometry optimization. What should be noted is, though, that this was not the finally used unit cell, but the one called C11C6F13-10/20grad-buc. The conclusion drawn hold anyway, as further tests showed.

| molecule | rotation / ° | total energy / eV | difference /eV |
|----------|--------------|-------------------|----------------|
| F6H11SH | 10 | -352.32 | 0.04 |
| F6H11SH | 20 | -352.36 | |

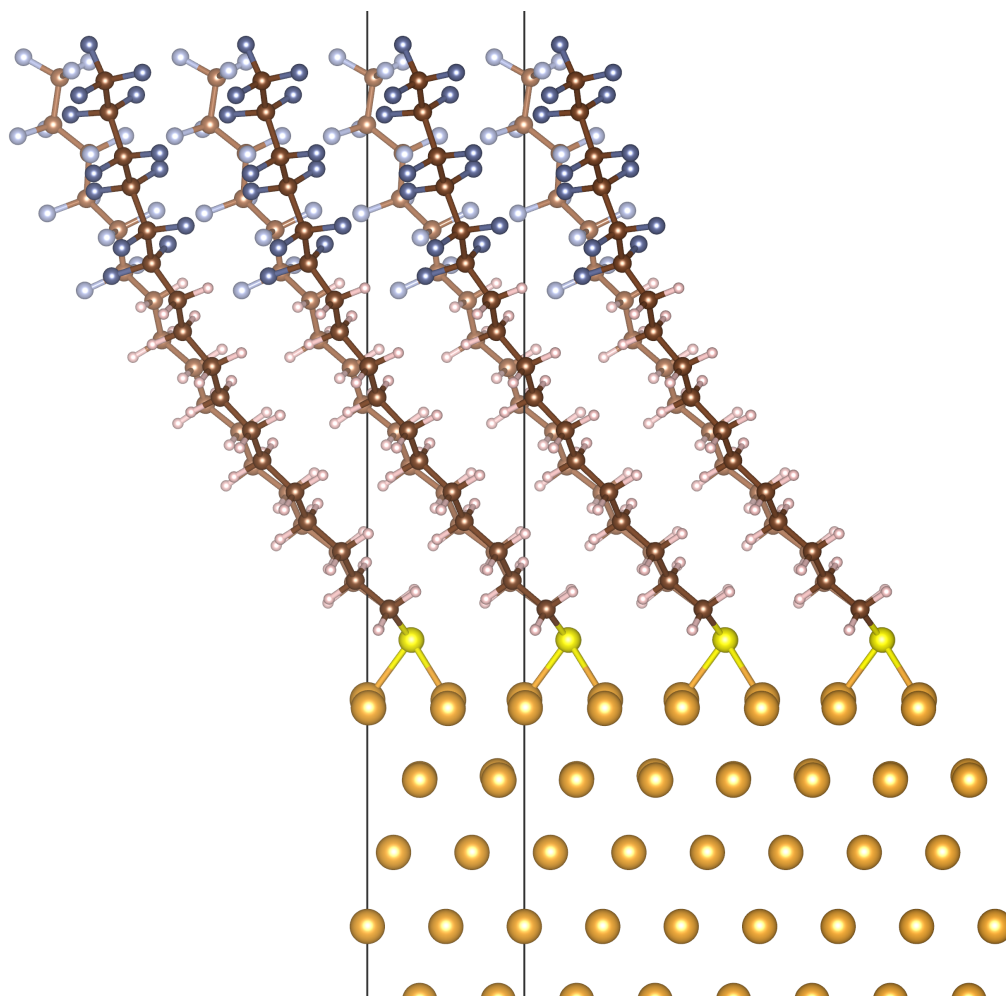


Figure 18: Ball-and-stick figure of the $F_6H_{11}SH$ -SAM on a Au(111)-substrate. The systems are shown after geometry optimization. The molecule drawn in darker colors was started with the fluorinated part rotated by 10 degrees, whereas the molecule shown in brighter colors was generated with a fluorinated part being rotated by 20 degrees (see text). The final geometries after optimization of the two systems do not look the same, especially the fluorinated segments differ quite a lot, whereas the alkyl parts look more alike.

Table 4: Core level shifts of systems calculated with a starting geometry created with a rotated fluorinated part by 10 and 20 degrees, respectively. What should be noted is, though, that this was not the finally used unit cell, but the one called C11C6F13-10/20grad-buc. The conclusion drawn hold anyway, as further tests showed.

| rotation / ° | relative shifts of C 1s peaks of different carbon atoms /eV | | | |
|--------------|---|--|--|--|
| | CF ₃ -CF ₂ | CF ₂ -CF ₂ CH ₂ | CF ₂ CH ₂ -CH ₂ CF ₂ | CH ₂ CF ₂ -CH ₂ |
| 10 | -1.42 | -0.58 | -4.69 | -0.47 |
| 20 | -1.38 | -0.54 | -4.60 | -0.38 |

5.3 IMPACT OF THE LENGTH OF THE FLUORINATED SEGMENT

Not only the impact of the geometrical structure of the fluorinated part was investigated, but also how the spectrum changes if the length of the fluorinated part is modified. For this, three different molecules were compared, namely one with six, eight and ten fluorinated carbon atoms, each of which with the same alkyl spacer consisting of eleven carbon atoms. Furthermore, it was possible to compare the experimental measurements, which are shown in figure 19, to the theoretical results, which are shown in figure 20. The experimental spectra are color-coded the same way as the modeled results for easier comparison.

When changing the length of the fluorinated carbon chain, the position of the peaks does not shift greatly, but the intensity of each but the CF_3 peak changes significantly. All spectra in figure 20 are normalized to the intensity of the CF_3 -peak (left peak), which means that the different spectra can be compared not only by looking at the core hole energies, but also the relative intensities of each peak compared to the CF_3 peak changes significantly. The different intensities of the two other peaks can be explained compellingly by the increased damping the electrons originating from the alkyl chain (rightmost peak) undergo due to the fluorinated part getting longer. This goes hand in hand with more carbon atoms contributing to the peak originating from the CF_2 atoms (middle peak). In figure 20 the different spectra of a $\text{F}_6\text{H}_{11}\text{SH}$ -, $\text{F}_8\text{H}_{11}\text{SH}$ - and $\text{F}_{10}\text{H}_{11}\text{SH}$ -SAM are shown on top of each other. The spectra were rigidly shifted for easier comparison so that each CF_3 -peak matches the one from the $\text{F}_8\text{H}_{11}\text{SH}$ *new UC* calculation. What should be noted is that for the curve denoted with $\text{F}_8\text{H}_{11}\text{SH}$ *new UC* a slightly different lattice constant for the gold slab was used compared to the other three unit cells. This geometrically further optimized unit cell changes the spectrum quantitatively a bit by moving the CH-peak to less negative binding energy values, which, as a result, resembles the experimental data better. The reason for showing this $\text{F}_8\text{H}_{11}\text{SH}$ *new UC* spectra alongside the other three, calculated with a different unit cell, is, that this *new* unit cell was found in the course of this thesis to be the one resembling the experimental findings the best (cf., chapter 5.1), but the calculations presented in this chapter had already been done before. Because the spectra of the $\text{F}_8\text{H}_{11}\text{SH}$ systems do look the same for both unit cells, the computationally intensive geometry optimization was not done again for the $\text{F}_6\text{H}_{11}\text{SH}$ - and $\text{F}_{10}\text{H}_{11}\text{SH}$ -systems, but the already optimized systems were used for comparison.

Looking at the differences when changing the length of the fluorinated carbon chain, the theoretical and experimental results show exactly the same trend, namely, that the intensity ratio of the upper to the lower chain decreases with the upper chain getting longer. This behavior is due to the surface sensitive nature of XPS-measurements, which means, that the atoms at the top of the SAM influence the spectrum more than the ones at the bottom. The spectra belonging to the $\text{F}_6\text{H}_{11}\text{SH}$ -SAM has two almost identically intensive peaks originating from the upper, fluorinated, and lower, hydrogenated, chain, even though there are almost twice as many carbon atoms in the lower chain compared to the upper one. Again, when looking at the $\text{F}_{10}\text{H}_{11}\text{SH}$ -SAM one can see quite nicely the surface sensitive nature of XPS, i. e., the CF_2 -peak is

by far the most prominent peak, even though the CH_2 -chain consists of two more carbon atoms. The height of the peaks is strongly influenced by the damping the electrons undergo, which is explained in more detail in chapter 3.4 of this thesis.

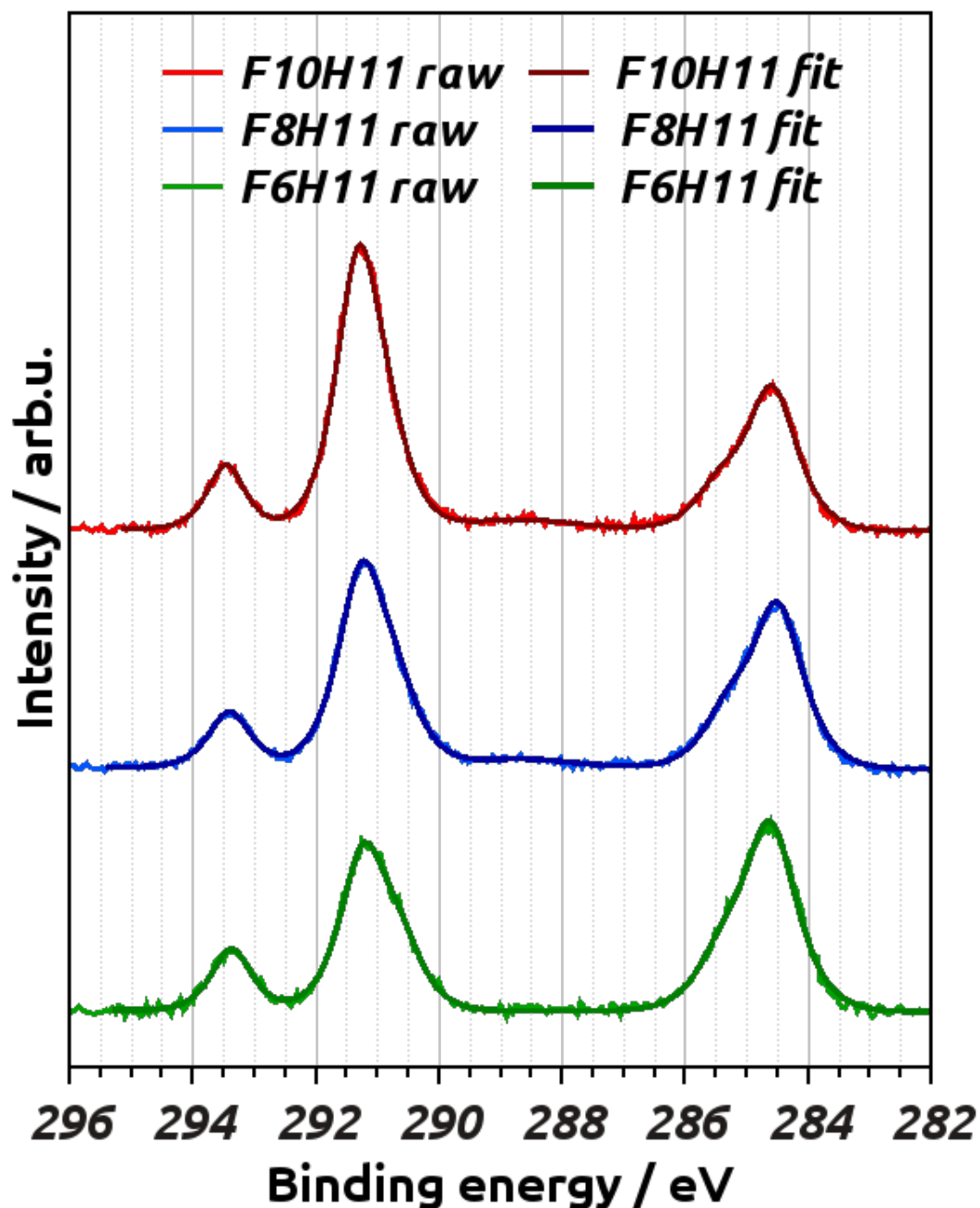


Figure 19: C 1s HRXPS spectra of F6H11SH-, F8H11SH- and F10H11SH-SAMs acquired at a photon energy of 508 eV. The lighter colored curve shows the actual experimental data, the darker one on top of it is the resulting fitting curve composed of gaussian peaks for each individual emission. Experimental HRXPS measurements were done by the group of Zharnikov and the data was published in the paper of Lu et al. [53]. Reprinted (adapted) with permission from [53]. Copyright (2013) American Chemical Society.

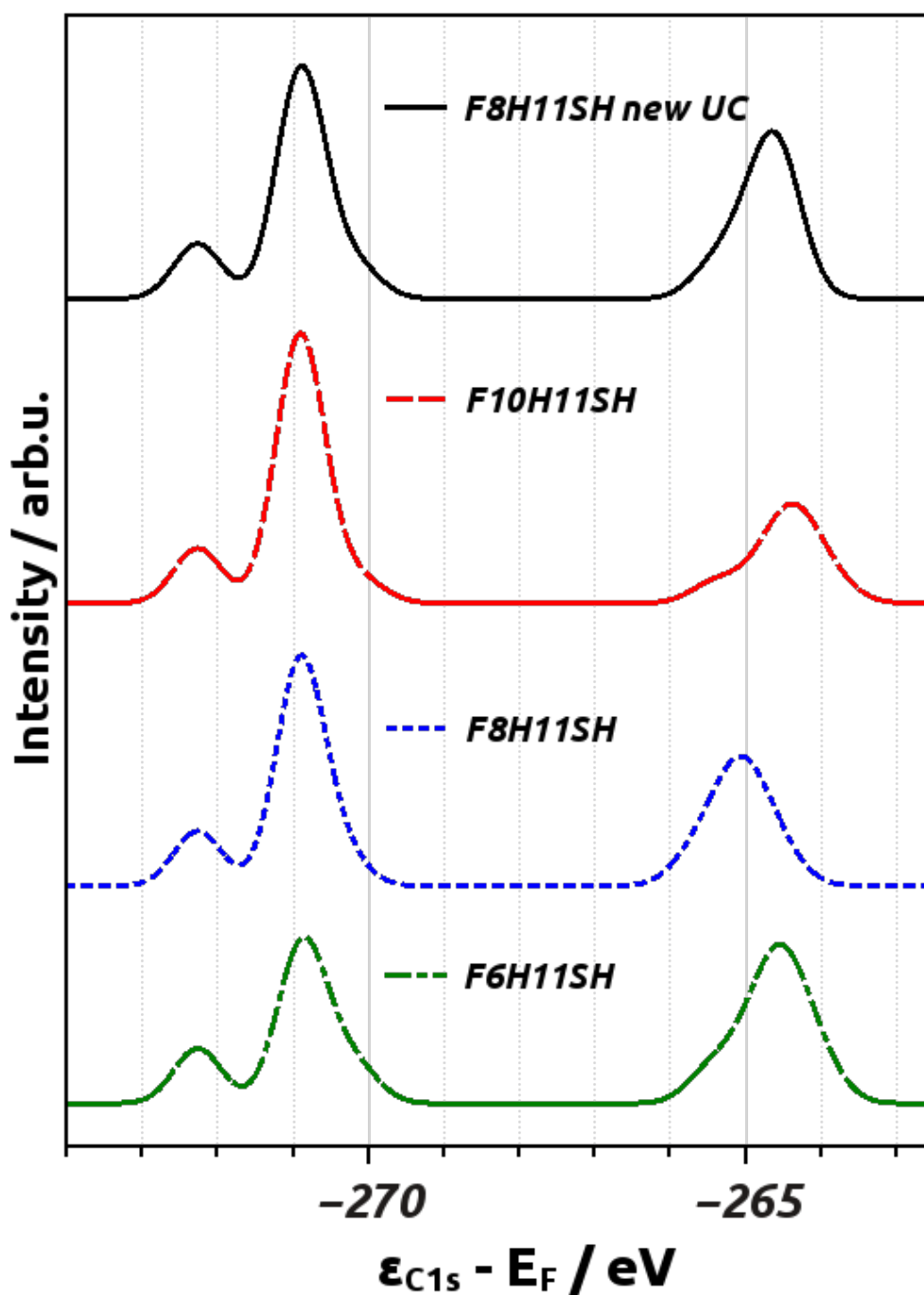


Figure 20: Spectra of (from top to bottom): $F_{8H_{11}SH}$ with an optimized gold slab (black, solid line), $F_{10H_{11}SH}$ (red, dashed line), $F_{8H_{11}SH}$ (blue, dotted line) and $F_{6H_{11}SH}$ (green, alternating dots and dashes). All spectra are shifted so the CF_3 -peaks (left peak) align with the one from the calculation of the $F_{8H_{11}SH-SAM}$ build with the further optimized unit cell at the very top. The peaks representing the CF_2 -chain (middle peak) lie above each other, but the peak for the lower lying CH_2 -chain (right peak) are slightly shifted. The intensity ratio of the upper to the lower chain decreases with the upper chain getting longer.

5.4 RESIDUAL ATTRACTIVE OR REPULSIVE: VDW-FORCES

To correctly model systems, which form a SAM consisting of long, upright standing molecules, considering vDW-forces is of utmost importance. Therefore, several calculations were done including vDW-forces, i. e., residual attractive or repulsive forces [112], and also entirely neglecting them.

For this the vdW^{surf} method by Ruiz et al. [113] was used, which is based on the vDW-TS scheme [114, 115] but also honors the Lifshitz-Zaremba-Kohn theory [116, 117] for vDW-interactions between an atom and a solid surface. Two different implementations of this method were used, namely one by Wissam Saidi et al. [118] in VASP version 5.3.2 (denoted as *vdW^{surf}S* in the following) and the other one implemented by Tomáš Bučko in VASP version 5.3.3-*tomas_extension* (denoted as *vdW^{surf}R*).

The calculations entirely without any vdW-forces for comparison were done with VASP version 5.3.3-*tomas_extension*. All three methods yielded quite different tilt angles θ for the alkyl part and also the fluorinated segment. A comparison of the different geometries resulting from calculations done with vdW^{surf}S, vdW^{surf}R and without any vDW-corrections can be seen in figure 21. There one can see that the structures are quite different, meaning that most probably the calculations ended up in different local minima of the potential energy surface.

The experimental values are given in figure 22 and are taken from the paper of Lu et al. [53]. The theoretical values are given in tables 5, 6 and 7 for three different optimization processes. What should be noted is that the reported tilt angles θ are measured as well as possible, but do not always give a comprehensive view of the molecule, because the chain itself is bent a little bit. The tilt angles are given as the angle between the vector pointing from the first to the last atom of the alkyl and from the first to the last but one atom of the fluorinated part, respectively, and the z-axis. This is done using the following formula:

$$\theta = \cos^{-1} \left(\frac{R_z}{\sqrt{R_x^2 + R_y^2 + R_z^2}} \right) \quad (27)$$

The last but one carbon atom in case of the fluorinated part was used to create the vector instead of the very last one at the top, because calculating the tilt angle using the terminating atom would not represent the overall direction of the chain, but rather point into quite another direction. This is because of the zig-zag like structure of the carbon backbone, so for the start and end point of the vector an odd (or even) numbered atom should be used. In this case the twelfth and the eighteenth carbon atom (counting from the sulfur atom) were taken to determine the tilt angle of the fluorinated part.

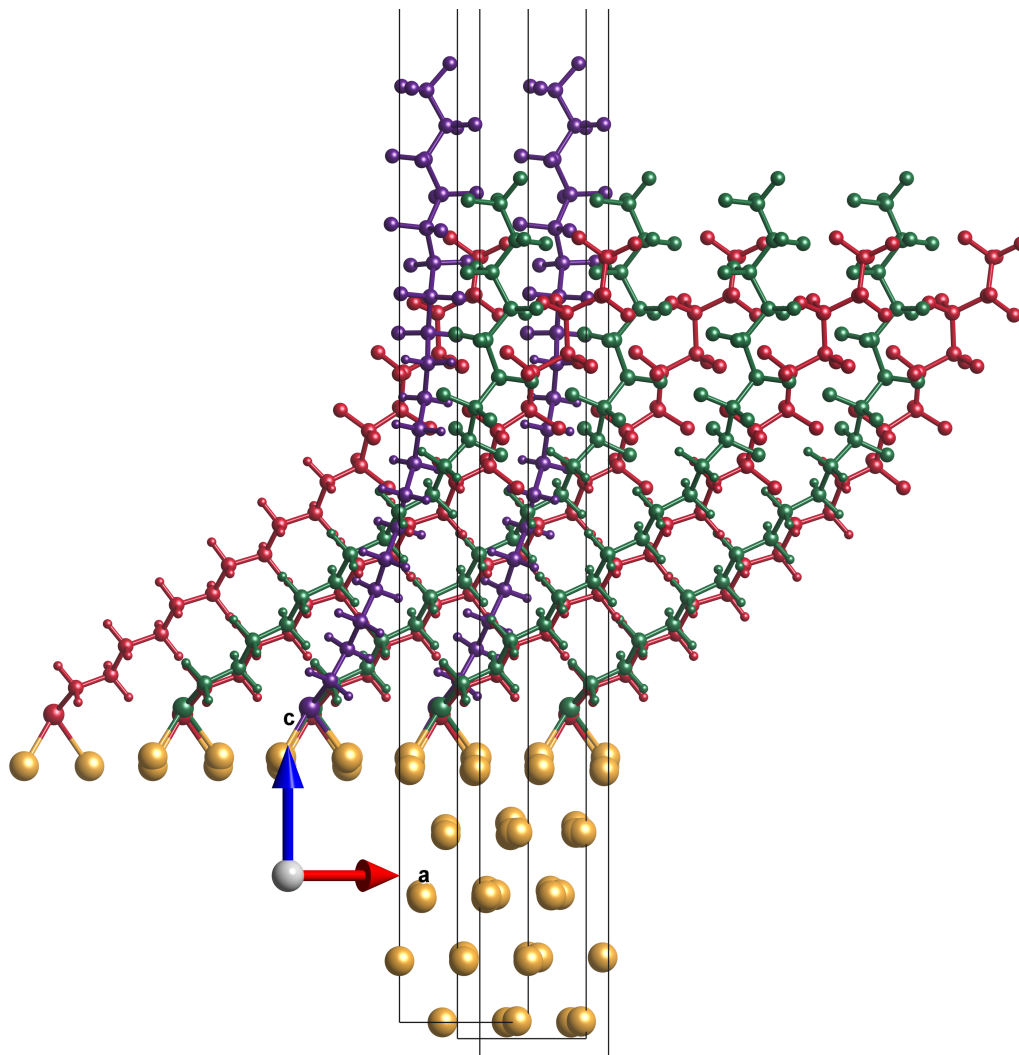


Figure 21: Balls-and-stick model of the **F10H11SH-SAM** on a Au(111) surface calculated with **VASP** considering **vdW**-corrections with the $\text{vdW}^{\text{surfS}}$ (red) and $\text{vdW}^{\text{surfR}}$ (green) scheme and also entirely neglecting any **vdW** contributions (violet).

Table 5: Tilt angles of the alkyl and fluorinated part of a **F10H11SH-SAM** calculated with different implementations of **vdW**-forces and entirely neglecting them. The most recent version, named $\text{vdW}^{\text{surfR}}$ yields values closest to the experimental findings (see figure 22 and main text), but they still do not match perfectly.

| vdW version | tilt angle alkyl / ° | tilt angle fluorinated / ° |
|-----------------------------|----------------------|----------------------------|
| no vdW | 20 | 1 |
| $\text{vdW}^{\text{surfS}}$ | 51 | 34 |
| $\text{vdW}^{\text{surfR}}$ | 49 | 7 |

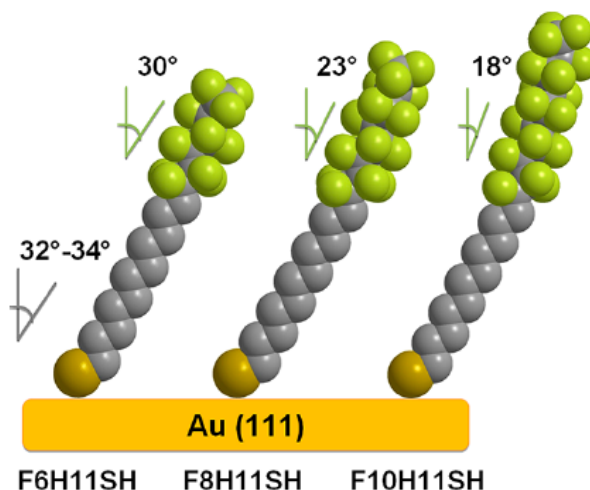


Figure 22: Schematic drawing of the molecular orientation in the $F_nH_{11}SH$ SAMs. The average tilt angles of the fluorinated part and alkyl segment are marked. The reported tilt angles were derived from NEXAFS measurements and the given uncertainty is $\pm 3^\circ$. Reprinted (adapted) with permission from [53]. Copyright (2013) American Chemical Society.

Table 6: Tilt angles of the alkyl and fluorinated part of a $F8H_{11}SH$ -SAM calculated with different implementations of vdW -forces and entirely neglecting them. The most recent version, named vdW^{surfR} yields values closest to the experimental findings (see figure 22 and main text), but they still do not match perfectly.

| vdW version | tilt angle alkyl / $^\circ$ | tilt angle fluorinated / $^\circ$ |
|---------------|-----------------------------|-----------------------------------|
| no vdW | 17 | 5 |
| vdW^{surfS} | 51 | 34 |
| vdW^{surfR} | 49 | 15 |

Table 7: Comparison of tilt angles of the alkyl and fluorinated part of a $F6H_{11}SH$, $F8H_{11}SH$ and $F_{10}H_{11}SH$ -SAM calculated with the latest, most advanced implementation of vdW -forces, i. e., vdW^{surfR} . For a SAM with $F8H_{11}SH$ and $F_{10}H_{11}SH$ the values obtained with vdW^{surfS} are also given for comparison. The trend is the same as observed in experiments (see figure 22 and main text), but the values do not match very well.

| SAM | tilt angle alkyl part / $^\circ$ | | tilt angle fluorinated part / $^\circ$ | |
|------------------|----------------------------------|---------------|--|---------------|
| | vdW^{surfS} | vdW^{surfR} | vdW^{surfS} | vdW^{surfR} |
| $F6H_{11}SH$ | n/a | 49 | n/a | 33 |
| $F8H_{11}SH$ | 51 | 49 | 34 | 15 |
| $F_{10}H_{11}SH$ | 51 | 49 | 34 | 7 |

5.5 COLLECTIVE ELECTROSTATIC EFFECTS

Another aspect investigated, which depends on the geometry of the molecules of the SAMs, was the influence of collective electrostatic effects. When lowering the coverage down to the single molecule limit (vide infra) and comparing the calculations with the full coverage situation, it can be shown that collective electrostatic effects can play an important role in densely packed SAMs. This is a quite obvious but rather overlooked effect.

The principle situation of how collective electrostatic effects in a SAM with an embedded dipole layer influence XPS-measurements is shown in figure 24. As can be deduced from the aforementioned figure, when a molecule with a polar group is assembled in an ordered fashion, a dipole layer is introduced, which affects the energy level alignment. This induced dipole layer is created by densely packed molecular dipoles and vanishes if the distance to the neighbor molecules gets big enough. This effect has to be considered when analyzing samples with, i. a., XPS. What has to be stressed is the fact that even chemically identical atoms are shifted in a spectrum if, e. g., a dipole layer is present in the SAM. In other words, e. g., a double-peak can appear instead of just a single peak for chemically identical atoms, which only differ in being arranged before and after a dipole layer introducing collective electrostatic effects.

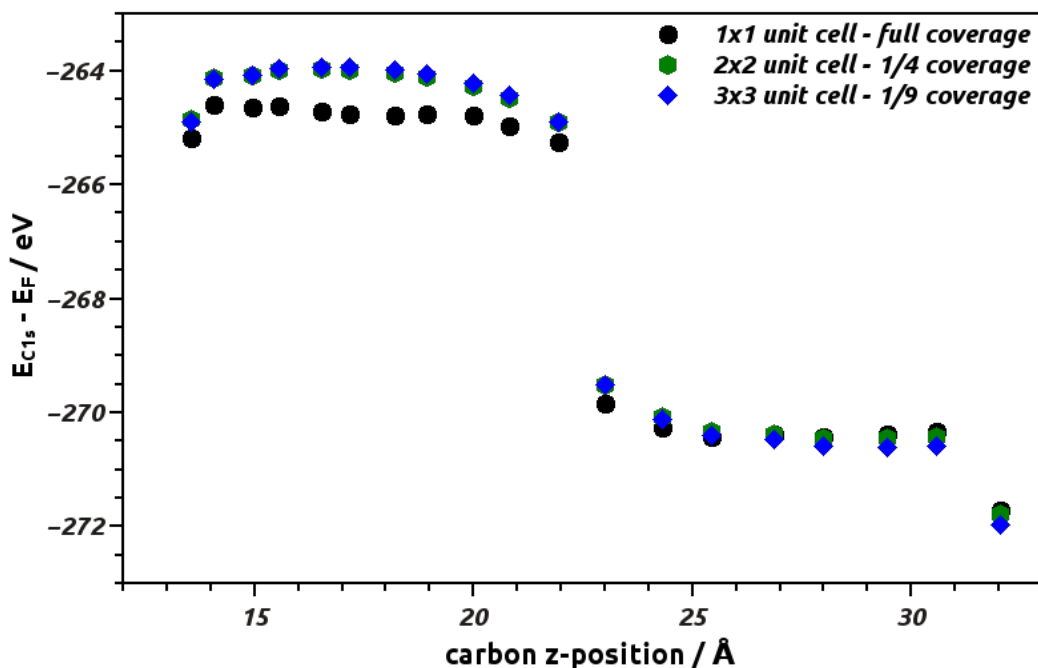


Figure 23: Core level energies for different coverages. The 1x1 resembles a full coverage system, whereas 2x2 shows a system with the unit cell doubled in x- and y-direction, resulting in a coverage of a quarter and 3x3 means that the SAM only has a coverage of 1/9 compared to the full coverage situation.

This effect leads to qualitatively completely different spectra, e. g., whether you are probing an alkyl chain only or one with an embedded dipolar group.[52] As a consequence, this allows creating surfaces with specific properties not only by changing the head group, but also by embedding dipolar elements into the molecule and, therefore, saving the active head group.

As already mentioned, these collective electrostatic effects arise because of a densely packed, ordered layer of dipoles. What is now interesting, is the limit at which these collective effects do not play a role anymore. To find this so called single molecule limit, different unit cells were produced with different coverages of the SAM by multiplying the full coverage unit cell in x- and y-direction, respectively, and, subsequently deleting all but one molecule on the gold substrate. This way a 2x2 and 3x3 unit cell was created, resulting in a system with containing a SAM with a coverage of 1/4 and 1/9, respectively. Creating the unit cell in this way (cf., 4.2) ensures that the distance between each molecule is the same in x- and y-direction when periodic boundary conditions are applied. The results for each coverage are shown in figure 23 and it can be seen that the Carbon 1s core-level energies are basically the same for a coverage of 1/4 and 1/9. Because the core level orbital energies do not change significantly any more when reducing the coverage from 1/4 to 1/9, this was defined as the single molecule limit for this system.

Looking specifically at the investigated systems, one can see that the step in the electrostatic energy due to the thiolat-bond diminishes at low coverages, and the shift compared to the full coverage situation is about 1.0 eV. Another interesting result, when comparing the full coverage system to the low coverage one, is that the core-level energies of the fluorinated carbon atoms are shifted way less compared to the hydrogenated carbon atoms. This can be explained by a small dipole pointing towards the metal surface which is localized at the interface between the alkyl segment of the molecule and the fluorinated part. This dipole layer gives rise to a small shift of the core-level energies to less negative values.[119] As already mentioned, one can see in figure 23 the collective electrostatic effects are in the range of 1 eV for the investigated systems and depend on the incorporated polar group as well as on charge rearrangement due to the bonding situation.

Overall, these electrostatic shifts are rather small compared to chemically induced shifts in the case of the systems investigated in the course of this thesis, but, nonetheless, do play a role, and, therefore, need to be considered when interpreting XPS-measurements.

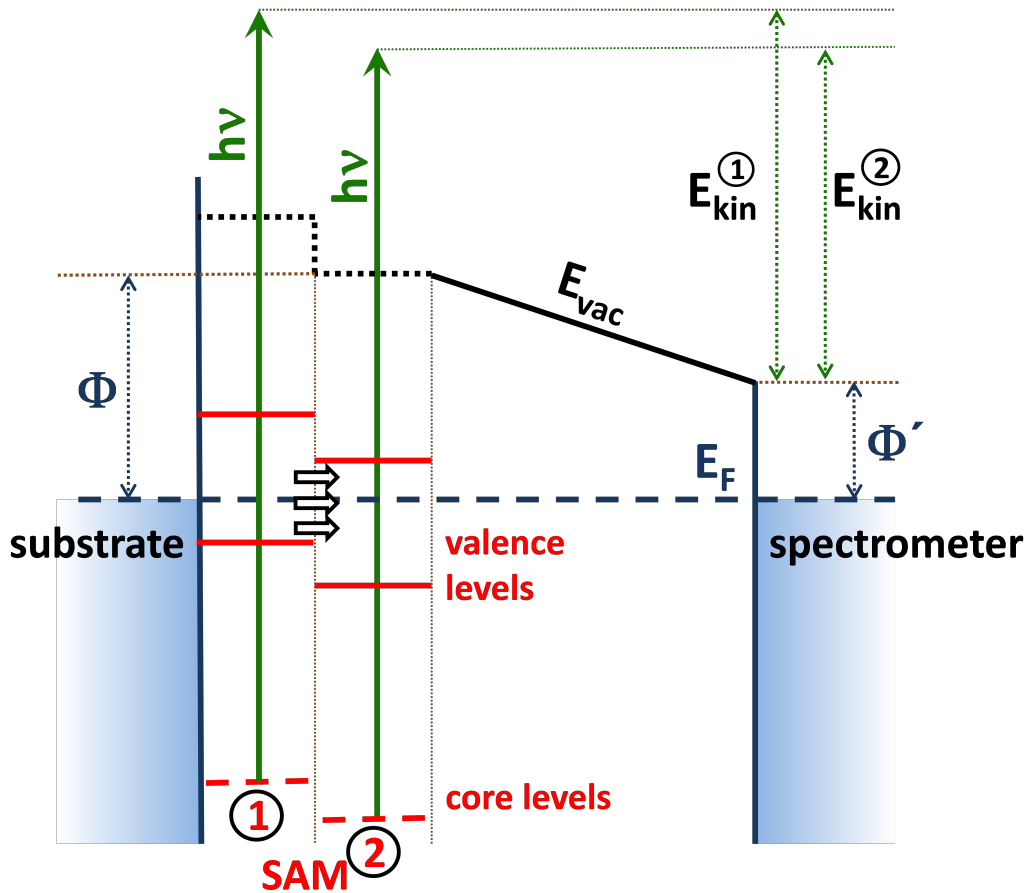


Figure 24: Schematic illustration of the energy level alignment in a SAM with an embedded dipole layer. The core and valence levels of the bottom segment (1) and top segment (2) of the molecules are separated by an ordered two-dimensional array of dipoles. The associated shift in energy results in two different measured electron kinetic energies at the detector (E_{kin}^1 and E_{kin}^2). The green arrows symbolize the XPS measurement process with the incident photon energy $h\nu$. E_F denotes the Fermi energy, which for zero bias is the same at the sample and detector sides of the setup [38] in contrast to the vacuum energy E_{vac} . The work function of the clean gold substrate is modified by the applied SAM to the resulting value Φ . For the sake of clarity, we assume an infinitely extended sample and detector; i. e., no distinction between the vacuum level directly above the sample and at a distance much larger than the sample dimensions is made, as this would not affect the differences in the kinetic energies of the photoelectrons. Figure and figure caption produced by E. Zojer and taken from [52].

5.6 HARD, SOFT OR SOMEWHERE INBETWEEN: PAW-POTENTIALS

For each element there are several PAW-potentials distributed with VASP, namely *soft*, *normal* and *hard* ones. The normal potentials come without any extension in the name, the soft potentials end with an *_s* and the hard potentials are postfixed with an *_h*.

All tests in this chapter were done utilizing the initial state method as described in chapter 2.2.7.1. As can be deduced from figure 25 and seen quite nicely in figure 26 the potentials do not give fundamentally different results when comparing the spectra, but only the alkyl chain is slightly shifted with respect to the fluorinated part.

The harder the potential, the larger the cutoff energy needs to be, because the potential utilizes smaller core radii. Taking the fact into account that the cutoff energy for the hard potential is almost twice as high as the one for the normal potential, the latter one was chosen for all further calculations.

In figure 25 the carbon 1s core-level energies are shown as calculated by VASP without any additional post processing like screening or broadening, only corrected by the Fermi energy of the calculation. As one can see, the various potentials give rise to slightly different energies for the same core levels. The normal potentials represent the experimental values the best by producing the biggest shift between the CH₂- and CF₂-chain, because the calculated energy shift between these two peaks is generally underestimated compared to experimental XPS data. This trend can be seen with all three, i. e., F6H11SH-, F8H11SH- and F10H11SH-SAMs investigated in this work.

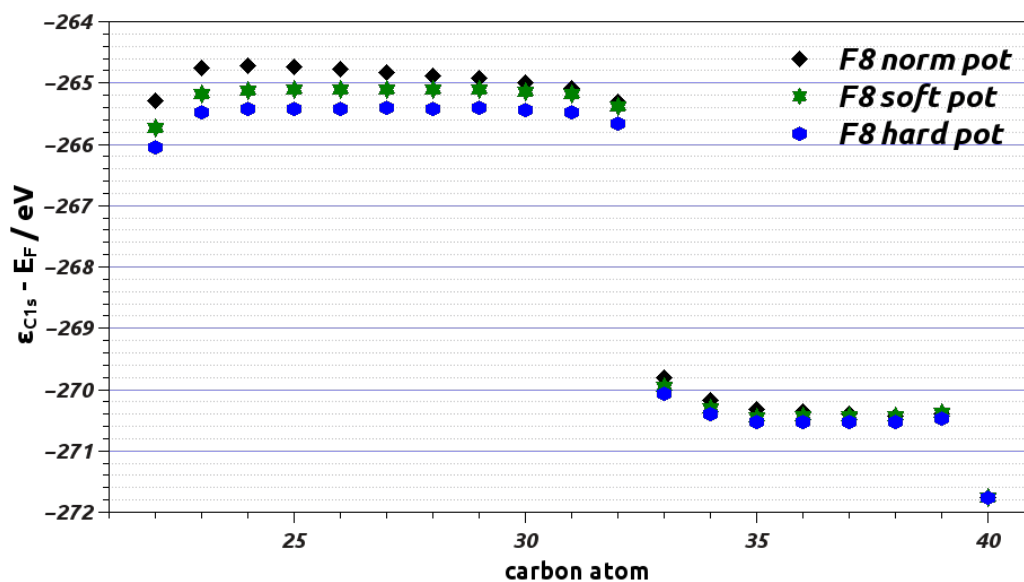


Figure 25: Scatter plot of the carbon 1s core-level energies calculated with VASP using different potentials, namely normal, hard and soft ones. All core-level energies are shifted for easier comparison in a way that the 1s core-level energy of the CF₃ atom of all calculations are identical.

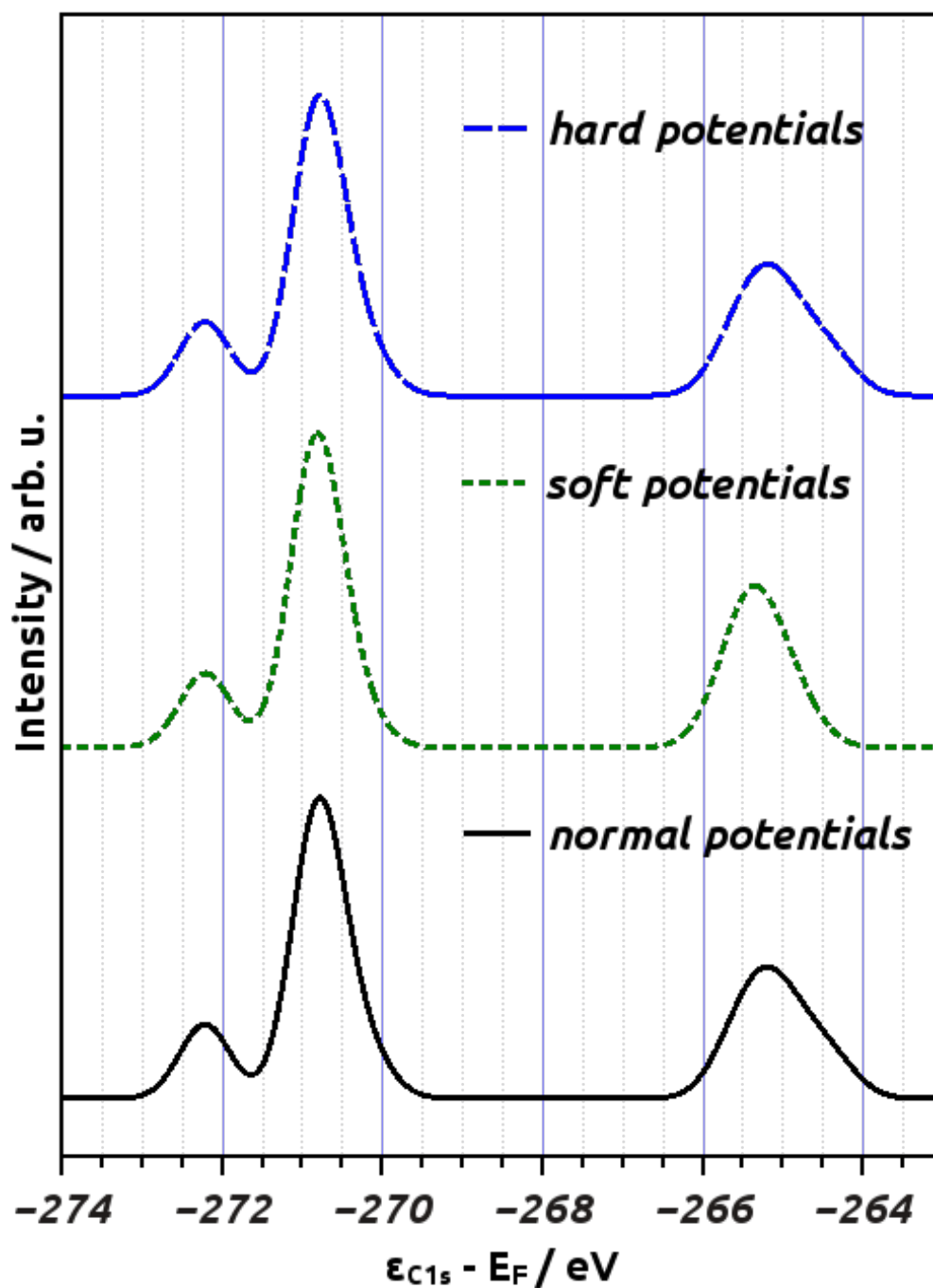


Figure 26: Spectrum of F8H11SH calculated with different PAW-potentials, aligned to the CF₃-peak. The leftmost peak is due to the CF₃-atom, the middle peak originates from the rest of the fluorinated atoms and the peak at the right stems from the alkyl chain. The relative shift is practically the same, differing by around 0.2 eV for the alkyl chain with respect to the other two peaks which are basically identical.

5.7 VASP VS. FHI-AIMS

The full potential code **FHI-AIMS** was used to benchmark the **PAW**-based results acquired with **VASP** using different cutoff energies. **FHI-AIMS** is an all-electron code based on numeric, atom-centered orbitals, this means, in contrast to **VASP** (cf., 2.2.5) it calculates the full (core) wave function for every electron in the system.

The **FHI-AIMS** calculations were done by our group member Oliver T. Hofmann, and were **PBE**-based, Gamma-Point only calculations with the energy convergence criterion set to 10×10^{-6} eV and the sum of all eigenvalues was converged to 0.01 eV. The complete input file named `control.in` used for this calculation can be found in appendix a.4.

Additionally, for **VASP** quite a lot of different cutoff energies (see chapter 2.2.4) were benchmarked, starting from the suggested 400 eV for the carbon and fluorine atoms up to almost doubling it to 700 eV. All other settings were kept the same in all calculations to achieve the best level of comparability.

As one can see quite nicely in figure 27, the absolute values of the core level orbital energies are basically the same with all chosen cutoff energies and are essentially rigid shifted compared to the results obtained with **FHI-AIMS**. The relative shift between the two different codes does not invalidate either of the results, but rather is a consequence of the underlying principle of these kind of **DFT** simulations. As is widely known, only relative energies bear any meaning - and the shown values are pretty much the same if shifted by a constant.

This means, using a higher cutoff energy for the calculations done with **VASP** does not change the core-level energy shifts, i. e., the cutoff energy is converged already at 400 eV. In line with the results acquired during this benchmarking, it was chosen to use **VASP** with a cutoff energy of 400 eV, because it offers by far the most superior cost-to-performance ratio.

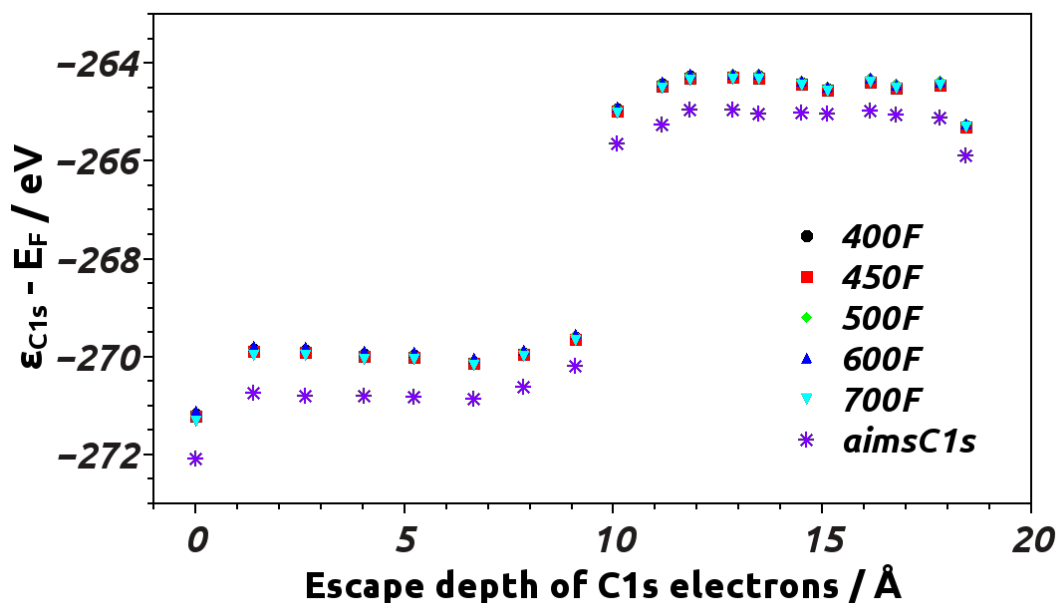


Figure 27: Absolute C 1s orbital energies calculated with VASP using different cutoff energies, and FHI-AIMS differ quite a bit, but if shifted by a constant, the so to speak relative energies obtained with VASP and FHI-AIMS are basically the same.

5.8 FINAL STATE TESTS

For reasons already mentioned in chapter 2.2.7.2, the results shown in this section are only presented as a test case, because the utilized methodology includes some fundamental obstacles which can not be tackled with today's computer resources.

First of all, what should be mentioned is the fact that one has to carry out a single point calculation for each and every core level in the molecule contributing to the XP-spectrum. On contrary, for the tests done in this chapter, only the 1s core level of selected carbon atoms were modeled using the final state approach to reduce the number of computational resources needed. To get sensible results, great care has to be taken when selecting which core levels to calculate. For being able to reproduce the experimental spectrum one has to do the simulation at least for each prototypical carbon atom in the molecule. In this case, this means only the very top carbon atom, attached to three fluorine atoms, the one next to this and the fifth one from the top (representing the CF₂-chain) were calculated, as well as the very last fluorinated carbon atom and the very first alkyl carbon, and the eighth carbon atom from the bottom (representing all carbon atoms from the alkyl chain). These carbon atoms were selected due to the initial state results, trying to include all important features and, therefore, model the actual spectrum of the full coverage SAM most accurately. This reduced the number of single point calculations needed from 21 to only six.

Keeping this in mind, the atoms as shown in table 8 were used to create the spectrum using the final state calculations.

Table 8: Carbon atoms of the [F10H11SH-SAM](#) which were used for the final state calculations utilizing the full core hole (FCH)- and half full core hole(HCH)-method (Slater's transition state). The numbers depict the position in the chain starting at the carbon atom at the very top, bonded to three fluor atoms.

| number | name | energy HCH / eV | energy FCH / eV |
|--------|---------------------------------|-----------------|-----------------|
| 1 | CF ₃ | -300.56 | -320.90 |
| 2 | CF ₂ CF ₃ | -298.36 | -319.14 |
| 6 | CF ₂ | -298.25 | -319.14 |
| 10 | CF ₂ CH ₂ | -298.13 | -318.71 |
| 11 | CH ₂ CF ₂ | -294.54 | -317.31 |
| 14 | CH ₂ | -293.53 | -316.20 |

5.8.1 Full core hole

In the full core hole method one electron e^- is moved from a 1s core level of a carbon atom to the valence band, i. e., the Fermi level of the metal, and, therefore, the simulation can include quantum mechanical relaxation effects, which are neglected when using the initial state method. A more detailed explanation can be found in chapter [2.2.7.2](#), where also some fundamental aspects are discussed.

In figure [28](#) a scatter plot of the core hole energies of such a calculation is shown. What one could deduce comparing these results to the one acquired using the initial state method is that in this case at least two more calculations should have been done to get more conclusive results; namely the nearest and next-nearest neighbors (carbon atom number 12 and 13) of the carbon atoms at the end of the alkyl chain. The energy shift of more than 1 eV between the alkyl chain and atom number eleven (which is also part of the alkyl chain, but next to the fluorinated chain) is quite significant. This jump in energy is noteworthy, because it is the only one that is quite off when comparing the final and initial state results, so this might be an artifact of the final state calculations.

Furthermore, the core level energy shift of the alkyl chain compared to the fluorinated segment is even smaller than in the initial state calculations. This too small shift between the alkyl and the fluorinated segment might be due to an artificial dipole layer introduced in the final state calculations as done in this work (cf., chapter [2.2.7.2](#)). This explanation also fits the results of the calculations with a half-full core hole (vide infra), because there the artifact is smaller due to only removing half of an electron from the core.

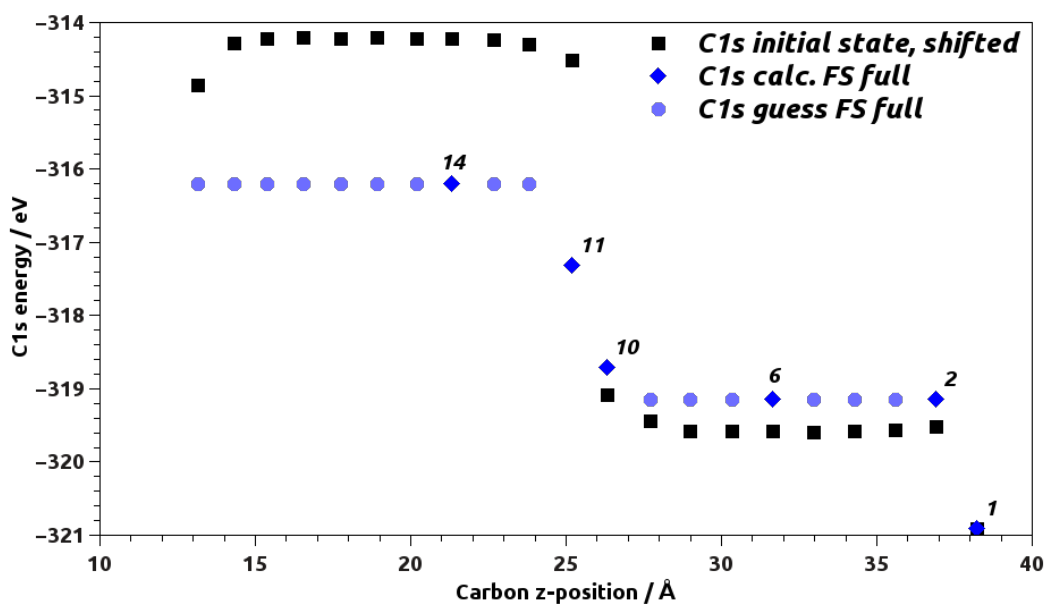


Figure 28: Scatter plot of C 1s energies aligned at the Fermi level acquired using the final state method with a full core hole ($1e^-$) moved to the valence band. The diamonds indicate the atoms actually calculated, whereas in contrast the round data points shown are only assumed values due to the chemical nature of the carbon atoms. The black squares show the core-level energies calculated in the initial state approach shifted so that the 1s core-level energy of the CF_3 -atom (lowest energy point) match. All points do not include screening effects due to the metal substrate as described in chapter 3.2 in more detail.

5.8.2 Half-full core hole

If only moving half of an electron ($0.5e^-$) to the valence band, i.e. applying Slater's transition state theory (see chapter 2.2.7.2), the theoretically acquired core level energies fit the experimental measured ones better in comparison to the full core hole method. This can be explained by the fact that the electrostatic artifacts are only half as big in the half-full core hole method. What is worth noting is that the core level energy of the last alkyl chain atom is not shifted as much away from the rest of the alkyl-chain compared to the full core hole calculations, but still the shift is more pronounced than in the case of the initial state calculations. Furthermore, here it seems that at least the second carbon atom of the alkyl-chain would have been of interest, to get a better understanding of the chemical influence of the fluorine atoms on the alkyl chain, especially, how long their influence ranges.

From Figure 29 can be deduced that the final state results acquired using Slater's transition state, i. e., moving half of an electron ($0.5e^-$) to the valence band, produces quantitatively a priori the best results, even though it still needs to be shifted by around 5 eV to best fit the experimental results. As already seen in the full core hole results, either the CF - or the CH -core-level energies are off, because the relative shift between the fluorinated part and the alkyl part of the molecule does not fit as nicely

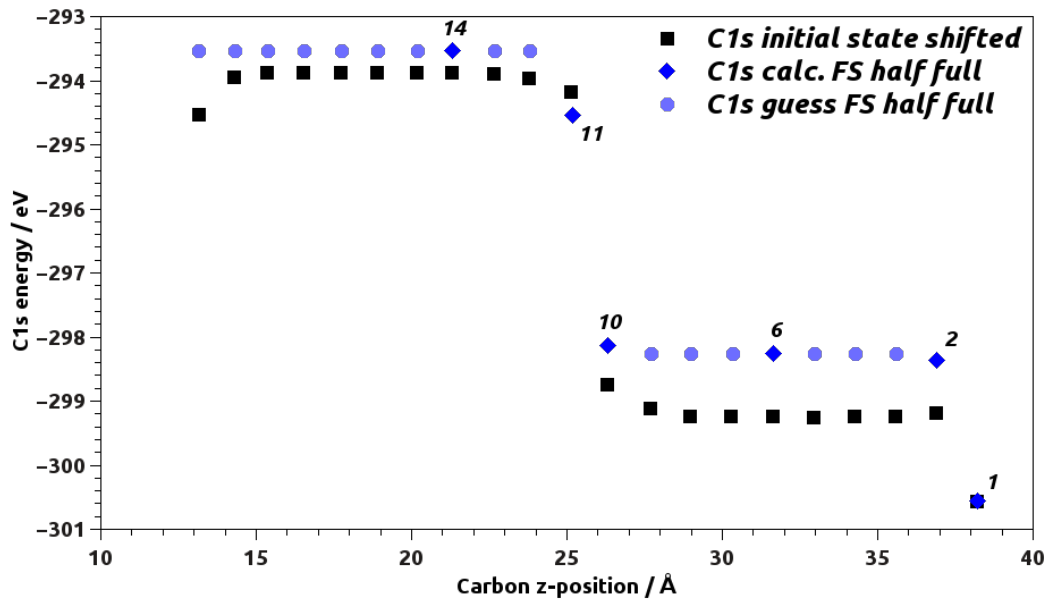


Figure 29: Scatter plot of C 1s energies aligned at the Fermi level acquired using the final state method with a half-full core hole, i. e., half of an electron ($0.5e^-$) moved to the valence band. The diamonds indicate the atoms actually calculated, whereas in contrast the round data points shown are only assumed values due to the chemical nature of the carbon atoms. The black squares show the core-level energies as calculated in the initial state approach shifted so that the 1s core-level energy of the CF_3 -atom (lowest energy point) match. All points do not include screening effects due to the metal substrate as described in chapter 3.2 in more detail.

as the shift between the two peaks originating from the CF_3 atom and the fluorinated segment. As in the case of the full core hole calculations (vide supra), this might be due to the artifacts introduced because of the too small unit cell which was used for the calculations.

Furthermore, what also has a minor influence on the position of the individual core-level energies is which PAW-potential is used for the calculations. This is discussed in more detail in chapter 5.6.

CONCLUSIONS AND OUTLOOK

As explained in chapter 5 the results acquired in the course of this thesis do fit the experimental spectra quite well, but are not perfect, yet. Furthermore, it was shown that the shifts of core-level energies as measured in XPS-experiments are not only due to the chemical environment of the probed atom, but also collective electrostatic effects can play an important role. These effects arise, e. g., due to charge rearrangements at the substrate/adsorbate interface or are introduced by embedded polar groups in the molecules forming a SAM. Even though these collective electrostatic effects are often overlooked, they do influence the electrostatic potential, and, as a consequence, shift the measured core levels of electrons. This means, great care has to be taken when interpreting XPS measurements and in most cases additional DFT-calculations can provide highly valuable insights.

To improve the theoretical predictions of core-level shifts of thin organic films on metal substrates even further, one has to tackle the challenges not mastered in this thesis. One big question concerns the obstacles which need to be overcome when using final state methods for adsorbate layers on a metal substrate (cf., chapter 2.2.7.2). Being able to utilize final state methods for such systems would provide the benefit of including quantum mechanical relaxation effects which are neglected in the initial state approach. This should improve the modeled spectra even further and, therefore, would be certainly worthwhile doing.

Part III
Appendix

TYPICAL INPUT FILES

VASP needs four input files to be able to start a calculation: INCAR, KPOINTS, POSCAR and POTCAR. Via the INCAR file all settings for **VASP** are provided. The KPOINTS file defines the k-point grid. In the POSCAR file the geometry of the system to calculate is stored. The POTCAR file consists of all the **PBE**-potentials used in the calculations, which must be given in the same order as in the POSCAR file specified.

A.1 INCAR

The INCAR file holds all settings for **VASP** so it knows how to do your calculations and is, therefore, quite important.

Listing 1: A standard INCAR file as used for single point calculations (mostly in conjunction with GADGET). As shown here the initial state method for calculating the orbital energies is enabled and **vdW**-forces are considered in the $\text{vdW}^{\text{surf}}\text{R}$ implementation.

```

1 SYSTEM = descriptive name for the system to be calculated
2
3 ISTART = 1 #use WAVECAR if exists
4 ICHARG = 1 #use CHGCAR if exists
5 ISPIN = 1 #non polarized 0 for polarized
6 NWRITE = 2 #what to write when out
7 PREC = Accurate #Normal or Accurate
8 ALGO = normal #Fast normal ist konservativer beim mischen
9
10 ENCUT = 400 #overwrite cutoff en from POTCAR because MASTER'S VOICE
    told me so
11 AMIN = 0.01 #hear your MASTER'S VOICE
12
13 NELM = 500 #max nr of electronic self-cons. steps
14 NELMIN = 8 #min nr of steps
15 EDIFF = 1E-06 #break condition for the electronic self-consistency
    cycle
16 EDIFFG = -1E-04 #break condition for ionic loop
17 NSW = 0 #max nr of ionic steps 0 for no geometry opt
18 IBRION = -1 #singlepoint, ions not moved
19 # IBRION = 2 #for conjugate gradient
20 ISIF = 2 #relax ions
21 # ISIF = 0 #do not relax ions
22

```

```
23 ICORELEVEL = 1 #core lvl en
24 # CLNT = 4 #which species is the one to treat differently (in POTCAR
    file)
25 # CLN = 1 #main quantum number of excited core electron
26 # CLL = 1 #l quantum number of excited core electron
27 # CLZ = 1 #electron count - how many electrons are excited (e.g. 1
    or 0.5)
28
29 LORBIT = 11 #write DOSCAR and PROCAR file with phase factors
30 EMIN = 20. #lowest KS eigenvalue, set >EMAX if you are not sure
    where the region of interest lies
31 EMAX = 10. #highest KS eigenvalue
32 NEDOS = 5001 #nr of grid points in DOS
33
34 ISMEAR = 0 #smearing 1 Methfessel-Paxton
35 SIGMA = 0.1 #smearing width
36 LREAL = A #False for bulk, set to TRUE for molecules, Auto suggested
37
38 LWAVE = .TRUE. #write WAVECAR
39 LCHARG = .TRUE. #write CHGCAR
40 LVTOT = .TRUE. #write total local potential
41 LVHAR = .TRUE. #write total local potential in LOCPOT, set to TRUE
    for only ionic and Hartree potential, set to FALSE to include
    exchange-correlation energy
42
43 IDIPOL = 3 #direction of the dipol moment
44 LDIPOL = .TRUE. #enable potential correction - use with IDIPOL
45
46 LDIPOLECONV = .TRUE.
47 DCONV = 10E-04
48
49 ## parallelisation parameters
50 LPLANE = .TRUE. #reduces communication bandwidth
51 LSCALU = .FALSE. #should be set like that ac. manual
52 ## these settings are set according to our group wiki
53 NSIM = 4 #should be set like that ac. manual
54 NCORE = 16
55 # NPAR = 8 #nr of cores - should not be used on VSC3
56
57 ## vdW-TS: for old vasp:
58 # LVDWTS = .TRUE.
59 # aeden_dir=/home/lv70706/elsiver/Src/aeden_vasp_vdw_TS
60
61 ## vdW: for new vasp
62 ## vdW_surf-Parameter - Au S C H F
63 IVDW = 2
64 VDW_alpha = 15.600 19.600 12.000 4.500 3.800
65 VDW_C6 = 7.725 7.725 2.687 0.375 0.549
66 VDW_R0 = 1.539 2.040 1.900 1.640 1.610
67 LVDW_SAMETYPE = F T T T T
```

A.2 KPOINTS

The KPOINTS file states the k-points to be calculated during a simulation.

Listing 2: A standard KPOINTS file as used for most of the calculations. The capital letters define the way the k-point mesh is created. In this example there are eight k-points in x- and y-direction and one (as it should always be the case when using the repeated slab approach) in z-direction.

```

1 Automatic Mesh
2 0
3 Gamma
4 8 8 1
5 0 0 0

```

A.3 INPDAT

The INPDAT file contains all options for GADGET and the options therein are, obviously, quite important if doing geometry optimizations.

Listing 3: A standard INPDAT file as used for most of the calculations. Only a couple of tags need to be adjusted if convergence is a problem, i. e., ASCALE, BSCALE, OPTENGINE. If the substrate detection fails, the parameter SUBST has to be changed until it succeeds.

```

1 Input file, check inputer.py for all available tags!!!
2
3 HESSIAN=3      # hessian initialised as a diag. matrix in cartesian
4               # internal coord.(1) space or as a model hessian
5               # (2,3) - 3: fischer's
6 HUPDATE=1     # hessian-update formula, 0-no update, 1-BFGS,
7               # 2-BFGS-TS, 3-SR1, 4-PSB,
8               # 5-SR1/PSB, 6-SR1/BFGS
9 CART=0        # optimization in cartesians (1) or in delocalized
10              # internals (0)
11 GCRITER=0.000194469 # convergence criterion - maximal gradient in
12              # Hartree/Bohr radius
13 SCRITER=5.02   # convergence criterion for geometry step - in Bohr,
14              # disabled because it does not make much sense, at least in our case
15 ECRITER=1     # convergence criterion - maximal energy change in
16              # Hartree, disabled because it does not make much sense, at least in
17              # our case
18 ASCALE=1.3    # scaling short range; factor for automatic
19              # coordinate identification
20 BSCALE=1.6    # long range scaling; additional scaling factor for
21              # covalent radii - only if more fragments are found
22 FRAGCOORD=2   # 2: add inverse-power distances 1/R ('IR1')
23 RELAX=0       # gitter vektoren optimieren
24 OPTENGINE=0   # engine for optimization (0-DIIS, 1-RFO)

```

```

16 NFREE=5          # higher than 5, more previous steps of calculation
    for current steps
17 NSW=1000        # maximal number of relaxation steps
18 SUBST=8          # set to your nearest neighbours, but check because
    it does not really work, you might have to increase this number
19 POTIM=100

```

A.4 CONTROL.IN

The control.in file holds all settings for [FHI-AIMS](#) so it knows how to do your calculations and is, therefore, quite important.

Listing 4: The control.in file shown here is the one used for the [FHI-AIMS](#)-calculations done by Oliver T. Hofmann described in chapter 5.7. It uses the [PBE](#)-potentials and is a Gamma-point only calculation.

```

1 xc pbe
2 charge 0
3 spin none
4 relativistic atomic_zora scalar
5
6 sc_accuracy_rho 1e-2
7 sc_accuracy_eev 1e-2
8 sc_accuracy_etot 1e-5
9
10 k_grid 1 1 1
11
12 use_dipole_correction .true.
13 compensate_multipole_errors .true.
14 distributed_spline_storage .true.
15 collect_eigenvectors .false.
16 use_local_index .true.
17
18
19
20 #output atom_proj_dos -20 10 3001 0.1
21
22
23 #####
24 #
25 # FHI-aims code project
26 # Volker Blum, Fritz Haber Institute Berlin, 2009
27 #
28 # Suggested "tight" defaults for S atom (to be pasted into
    control.in file)
29 #
30 # Revised Jan 04, 2011, following tests (SiC) done by Lydia Nemeč:
31 #   d and g functions of tier 2 now enabled by default.
32 #

```

```
33 #####
34 species          S
35 #   global species definitions
36   nucleus          16
37   mass             32.065
38 #
39   l_hartree        6
40 #
41   cut_pot          4.0          2.0  1.0
42   basis_dep_cutoff 1e-4
43 #
44   radial_base      44 7.0
45   radial_multiplier 2
46   angular_grids    specified
47     division 0.4665 110
48     division 0.5810 194
49     division 0.7139 302
50     division 0.8274 434
51 #     division 0.9105 590
52 #     division 1.0975 770
53 #     division 1.2028 974
54 #   outer_grid 974
55     outer_grid 434
56 #####
57 #
58 # Definition of "minimal" basis
59 #
60 #####
61 #   valence basis states
62   valence 3 s 2.
63   valence 3 p 4.
64 #   ion occupancy
65   ion_occ 3 s 1.
66   ion_occ 3 p 3.
67 #####
68 #
69 # Suggested additional basis functions. For production calculations,
70 # uncomment them one after another (the most important basis
71 # functions are
72 # listed first).
73 #
74 # Constructed for dimers: 1.6 A, 1.9 A, 2.5 A, 3.25 A, 4.0 A
75 #
76 #####
77 # "First tier" - improvements: -652.81 meV to -45.53 meV
78   ionic 3 d auto
79   hydro 2 p 1.8
80   hydro 4 f 7
81   ionic 3 s auto
82 # "Second tier" - improvements: -30.20 meV to -1.74 meV
83   hydro 4 d 6.2
```

```

83     hydro 5 g 10.8
84 #     hydro 4 p 4.9
85 #     hydro 5 f 10
86 #     hydro 1 s 0.8
87 # "Third tier" - improvements: -1.04 meV to -0.20 meV
88 #     hydro 3 d 3.9
89 #     hydro 3 d 2.7
90 #     hydro 5 g 12
91 #     hydro 4 p 10.4
92 #     hydro 5 f 12.4
93 #     hydro 2 s 1.9
94 # "Fourth tier" - improvements: -0.35 meV to -0.06 meV
95 #     hydro 4 d 10.4
96 #     hydro 4 p 7.2
97 #     hydro 4 d 10
98 #     hydro 5 g 19.2
99 #     hydro 4 s 12
100
101 #####
102 #
103 # FHI-aims code project
104 # Volker Blum, Fritz Haber Institute Berlin, 2009
105 #
106 # Suggested "tight" defaults for C atom (to be pasted into
107 #     control.in file)
108 #####
109 species      C
110 #   global species definitions
111   nucleus          6
112   mass             12.0107
113 #
114   l_hartree        6
115 #
116   cut_pot          4.0  2.0  1.0
117   basis_dep_cutoff 1e-4
118 #
119   radial_base      34 7.0
120   radial_multiplier 2
121   angular_grids specified
122     division    0.2187  50
123     division    0.4416 110
124     division    0.6335 194
125     division    0.7727 302
126     division    0.8772 434
127 #     division    0.9334 590
128 #     division    0.9924 770
129 #     division    1.0230 974
130 #     division    1.5020 1202
131 #   outer_grid    974
132   outer_grid      434

```

```
133 #####
134 #
135 # Definition of "minimal" basis
136 #
137 #####
138 #   valence basis states
139   valence      2 s  2.
140   valence      2 p  2.
141 #   ion occupancy
142   ion_occ      2 s  1.
143   ion_occ      2 p  1.
144 #####
145 #
146 # Suggested additional basis functions. For production calculations,
147 # uncomment them one after another (the most important basis
148 # functions are
149 # listed first).
150 # Constructed for dimers: 1.0 A, 1.25 A, 1.5 A, 2.0 A, 3.0 A
151 #
152 #####
153 # "First tier" - improvements: -1214.57 meV to -155.61 meV
154   hydro 2 p 1.7
155   hydro 3 d 6
156   hydro 2 s 4.9
157 # "Second tier" - improvements: -67.75 meV to -5.23 meV
158   hydro 4 f 9.8
159   hydro 3 p 5.2
160   hydro 3 s 4.3
161   hydro 5 g 14.4
162   hydro 3 d 6.2
163 # "Third tier" - improvements: -2.43 meV to -0.60 meV
164 #   hydro 2 p 5.6
165 #   hydro 2 s 1.4
166 #   hydro 3 d 4.9
167 #   hydro 4 f 11.2
168 # "Fourth tier" - improvements: -0.39 meV to -0.18 meV
169 #   hydro 2 p 2.1
170 #   hydro 5 g 16.4
171 #   hydro 4 d 13.2
172 #   hydro 3 s 13.6
173 #   hydro 4 f 17.6
174 # Further basis functions - improvements: -0.08 meV and below
175 #   hydro 3 s 2
176 #   hydro 3 p 6
177 #   hydro 4 d 20
178 #####
179 #
180 # FHI-aims code project
181 # Volker Blum, Fritz Haber Institute Berlin, 2009
182 #
```

```
183 # Suggested "tight" defaults for H atom (to be pasted into
    # control.in file)
184 #
185 #####
186 species      H
187 #   global species definitions
188   nucleus      1
189   mass         1.00794
190 #
191   l_hartree    6
192 #
193   cut_pot      4.0  2.0  1.0
194   basis_dep_cutoff 1e-4
195 #
196   radial_base  24 7.0
197   radial_multiplier 2
198   angular_grids  specified
199     division  0.1930  50
200     division  0.3175  110
201     division  0.4293  194
202     division  0.5066  302
203     division  0.5626  434
204 #   division  0.5922  590
205 #   division  0.6227  974
206 #   division  0.6868 1202
207 #   outer_grid 770
208     outer_grid 434
209 #####
210 #
211 # Definition of "minimal" basis
212 #
213 #####
214 #   valence basis states
215   valence      1 s  1.
216 #   ion occupancy
217   ion_occ      1 s  0.5
218 #####
219 #
220 # Suggested additional basis functions. For production calculations,
221 # uncomment them one after another (the most important basis
    # functions are
222 # listed first).
223 #
224 # Basis constructed for dimers: 0.5 A, 0.7 A, 1.0 A, 1.5 A, 2.5 A
225 #
226 #####
227 # "First tier" - improvements: -1014.90 meV to -62.69 meV
228   hydro 2 s 2.1
229   hydro 2 p 3.5
230 # "Second tier" - improvements: -12.89 meV to -1.83 meV
231   hydro 1 s 0.85
```

```
232     hydro 2 p 3.7
233     hydro 2 s 1.2
234     hydro 3 d 7
235 # "Third tier" - improvements: -0.25 meV to -0.12 meV
236 #     hydro 4 f 11.2
237 #     hydro 3 p 4.8
238 #     hydro 4 d 9
239 #     hydro 3 s 3.2
240 #####
241 #
242 # FHI-aims code project
243 # Volker Blum, Fritz Haber Institute Berlin, 2009
244 #
245 # Suggested "tight" defaults for F atom (to be pasted into
    control.in file)
246 #
247 #####
248 species      F
249 #   global species definitions
250     nucleus      9
251     mass         18.9984032
252 #
253     l_hartree    6
254 #
255     cut_pot      4.0  2.0  1.0
256     basis_dep_cutoff 1e-4
257 #
258     radial_base  37 7.0
259     radial_multiplier 2
260     angular_grids specified
261         division  0.4014 110
262         division  0.5291 194
263         division  0.6019 302
264         division  0.6814 434
265 #     division  0.7989 590
266 #     division  0.8965 770
267 #     division  1.3427 974
268 #     outer_grid  974
269     outer_grid  434
270 #####
271 #
272 # Definition of "minimal" basis
273 #
274 #####
275 #   valence basis states
276     valence      2 s  2.
277     valence      2 p  5.
278 #   ion occupancy
279     ion_occ      2 s  1.
280     ion_occ      2 p  4.
281 #####
```

```

282 #
283 # Suggested additional basis functions. For production calculations,
284 # uncomment them one after another (the most important basis
      functions are
285 # listed first).
286 #
287 # Constructed for dimers: 1.2 A, 1.418 A, 1.75 A, 2.25 A, 3.25 A
288 #
289 #####
290 # "First tier" - improvements: -149.44 meV to -45.88 meV
291     hydro 2 p 1.7
292     hydro 3 d 7.4
293     hydro 3 s 6.8
294 # "Second tier" - improvements: -12.96 meV to -1.56 meV
295     hydro 4 f 11.2
296     ionic 2 p auto
297     hydro 1 s 0.75
298     hydro 4 d 8.8
299     hydro 5 g 16.8
300 # "Third tier" - improvements: -0.58 meV to -0.05 meV
301 #     hydro 3 p 6.2
302 #     hydro 3 s 3.2
303 #     hydro 4 f 9.6
304 #     hydro 3 s 19.6
305 #     hydro 4 d 8.6
306 #     hydro 5 g 14.4
307 # Further basis functions: -0.05 meV and below
308 #     hydro 3 p 4.2
309 #####
310 #
311 # FHI-aims code project
312 # Volker Blum, Fritz Haber Institute Berlin, 2009
313 #
314 # Suggested "tight" defaults for Au atom (to be pasted into
      control.in file)
315 #
316 #####
317 species      Au
318 #   global species definitions
319     nucleus      79
320     mass         196.966569
321 #
322     l_hartree    6
323 #
324     cut_pot     4.0  2.0  1.0
325     basis_dep_cutoff 1e-4
326 #
327     radial_base  73 7.0
328     radial_multiplier 2
329     angular_grids specified
330     division    0.3416  50

```

```

331     division    0.7206  110
332     division    1.1171  194
333     division    1.2821  302
334     division    1.5560  434
335 #     division    2.1046  590
336 #     division    2.2363  770
337 #     division    2.2710  974
338 #     division    2.8078 1202
339 #     outer_grid 1202
340     outer_grid  434
341 #####
342 #
343 # Definition of "minimal" basis
344 #
345 #####
346 #     valence basis states
347     valence      6  s   1.
348     valence      5  p   6.
349     valence      5  d  10.
350     valence      4  f  14.
351 #     ion occupancy
352     ion_occ      6  s   0.
353     ion_occ      5  p   6.
354     ion_occ      5  d   9.
355     ion_occ      4  f  14.
356 #####
357 #
358 # Suggested additional basis functions. For production calculations,
359 # uncomment them one after another (the most important basis
360 # functions are
361 # listed first).
362 #
362 # Constructed for dimers: 2.10, 2.45, 3.00, 4.00 AA
363 #
364 #####
365 # "First tier" - max. impr. -161.60 meV, min. impr. -4.53 meV
366     ionic 6 p auto
367     hydro 4 f 7.4
368     ionic 6 s auto
369     hydro 5 g 10
370     hydro 6 h 12.8
371     hydro 3 d 2.5
372 # "Second tier" - max. impr. -2.46 meV, min. impr. -0.28 meV
373 #     hydro 5 f 14.8
374 #     hydro 4 d 3.9
375 #     hydro 3 p 3.3
376 #     hydro 1 s 0.45
377 #     hydro 5 g 16.4
378 #     hydro 6 h 13.6
379 # "Third tier" - max. impr. -0.49 meV, min. impr. -0.09 meV
380 #     hydro 4 f 5.2

```

```
381 # hydro 4 d 5
382 # hydro 5 g 8
383 # hydro 5 p 8.2
384 # hydro 6 d 12.4
385 # hydro 6 s 14.8
386 # Further basis functions: -0.08 meV and below
387 # hydro 5 f 18.8
388 # hydro 5 g 20
389 # hydro 5 g 15.2
```

SOFTWARE USED FOR THIS WORK

Here the software packages are listed which were used in the course of this work.

First of all, [VASP](#) should be named, with which almost all [DFT](#)-calculations were done. The exact versions are 5.3.2 and 5.3.3-*tomas_extension*. The second [DFT](#)-code used was [FHI-AIMS](#), although it was utilized primarily for testing and validating results obtained with [VASP](#). Furthermore, GADGET version 0.98 was used in conjunction with [VASP](#).

For creating the unit cell substrate the ASE-package [111] version 3.8.1.3440 was used, which provides a handy tool for this task.

The chemical formulas were typeset with MarvinSketch version 6.2.1. For doing all the 3D plots either OVITO [120] version 2.7.1 or VESTA [121] version 3.3.8 was used. All of the plots were done using either QtiPlot¹ version 0.9.8.8 svn 2255 or python 3 with its matplotlib version 1.5.2 and, subsequently, stitched together using gimp version 2.8.18.

This very document was edited in T_EXstudio version 2.10.2 and typeset by L^AT_EX utilizing the amazing (and slightly modified) *Classic Thesis Style v4.2* by André Miede².

¹ www.qtiplot.com

² www.miede.de

BIBLIOGRAPHY

1. G. Kresse and J. Furthmüller. “Efficient Iterative Schemes for Ab Initio Total-Energy Calculations Using a Plane-Wave Basis Set”. *Physical Review B* **54**, 11169 (15, 1996) (see p. 2).
2. G. Kresse and J. Hafner. “Ab Initio Molecular Dynamics for Liquid Metals”. *Physical Review B* **47**, 558 (1, 1993) (see p. 2).
3. G. Kresse and J. Furthmüller. “Efficiency of Ab-Initio Total Energy Calculations for Metals and Semiconductors Using a Plane-Wave Basis Set”. *Computational Materials Science* **6**, 15 (1996) (see p. 2).
4. R. G. Nuzzo and D. L. Allara. “Adsorption of Bifunctional Organic Disulfides on Gold Surfaces”. *Journal of the American Chemical Society* **105**, 4481 (1983) (see p. 2).
5. A. Ulman. *An Introduction to Ultrathin Organic Films: From Langmuir-Blodgett to Self-Assembly* 442 pp. (Academic Press, Boston, 1991) (see p. 2).
6. J. C. Love, L. A. Estroff, J. K. Kriebel, R. G. Nuzzo, and G. M. Whitesides. “Self-Assembled Monolayers of Thiolates on Metals as a Form of Nanotechnology”. *Chemical Reviews* **105**, 1103 (2005) (see p. 2).
7. X. J. Feng and L. Jiang. “Design and Creation of Superwetting/Antiwetting Surfaces”. *Advanced Materials* **18**, 3063 (4, 2006) (see p. 2).
8. S. L. Gras, T. Mahmud, G. Rosengarten, A. Mitchell, and K. Kalantar-zadeh. “Intelligent Control of Surface Hydrophobicity”. *ChemPhysChem* **8**, 2036 (8, 2007) (see p. 2).
9. N. Ballav, A. Shaporenko, A. Terfort, and M. Zharnikov. “A Flexible Approach to the Fabrication of Chemical Gradients”. *Advanced Materials* **19**, 998 (6, 2007) (see p. 2).
10. B. de Boer, A. Hadipour, M. M. Mandoc, T. van Woudenberg, and P. W. M. Blom. “Tuning of Metal Work Functions with Self-Assembled Monolayers”. *Advanced Materials* **17**, 621 (8, 2005) (see p. 2).
11. I. Lange, S. Reiter, M. Pätzelt, A. Zykov, A. Nefedov, J. Hildebrandt, S. Hecht, S. Kowarik, C. Wöll, G. Heimel, and D. Neher. “Tuning the Work Function of Polar Zinc Oxide Surfaces Using Modified Phosphonic Acid Self-Assembled Monolayers”. *Advanced Functional Materials* **24**, 7014 (2014) (see p. 2).
12. I. H. Campbell, S. Rubin, T. A. Zawodzinski, J. D. Kress, R. L. Martin, D. L. Smith, N. N. Barashkov, and J. P. Ferraris. “Controlling Schottky Energy Barriers in Organic Electronic Devices Using Self-Assembled Monolayers”. *Physical Review B* **54**, R14321 (15, 1996) (see p. 2).

13. I. H. Campbell, J. D. Kress, R. L. Martin, D. L. Smith, N. N. Barashkov, and J. P. Ferraris. "Controlling Charge Injection in Organic Electronic Devices Using Self-Assembled Monolayers". *Applied Physics Letters* **71**, 3528 (1997) (see p. 2).
14. S. Kobayashi, T. Nishikawa, T. Takenobu, S. Mori, T. Shimoda, T. Mitani, H. Shimotani, N. Yoshimoto, S. Ogawa, and Y. Iwasa. "Control of Carrier Density by Self-Assembled Monolayers in Organic Field-Effect Transistors". *Nature Materials* **3**, 317 (2004) (see p. 2).
15. H. Ishii, K. Sugiyama, E. Ito, and K. Seki. "Energy Level Alignment and Interfacial Electronic Structures at Organic/Metal and Organic/Organic Interfaces". *Advanced Materials* **11**, 605 (1999) (see p. 2).
16. G. Heimel, L. Romaner, J.-L. Brédas, and E. Zojer. "Interface Energetics and Level Alignment at Covalent Metal-Molecule Junctions: π -Conjugated Thiols on Gold". *Physical Review Letters* **96**, 196806 (2006) (see pp. 2, 3).
17. C. Schmidt, A. Witt, and G. Witte. "Tailoring the Cu(100) Work Function by Substituted Benzenethiolate Self-Assembled Monolayers". *The Journal of Physical Chemistry A* **115**, 7234 (30, 2011) (see p. 2).
18. N. Crivillers, S. Osella, C. Van Dyck, G. M. Lazzerini, D. Cornil, A. Liscio, F. Di Stasio, S. Mian, O. Fenwick, F. Reinders, M. Neuburger, E. Treossi, M. Mayor, V. Palermo, F. Cacialli, J. Cornil, and P. Samori. "Large Work Function Shift of Gold Induced by a Novel Perfluorinated Azobenzene-Based Self-Assembled Monolayer". *Advanced Materials* **25**, 432 (18, 2013) (see p. 2).
19. J. Kim, Y. S. Rim, Y. Liu, A. C. Serino, J. C. Thomas, H. Chen, Y. Yang, and P. S. Weiss. "Interface Control in Organic Electronics Using Mixed Monolayers of Carboranethiol Isomers". *Nano Letters* **14**, 2946 (14, 2014) (see p. 2).
20. O. M. Cabarcos, A. Shaporenko, T. Weidner, S. Uppili, L. S. Dake, M. Zharnikov, and D. L. Allara. "Physical and Electronic Structure Effects of Embedded Dipoles in Self-Assembled Monolayers: Characterization of Mid-Chain Ester Functionalized Alkanethiols on Au{111}". *The Journal of Physical Chemistry C* **112**, 10842 (2008) (see pp. 2, 3).
21. D. A. Egger, F. Rissner, G. M. Rangger, O. T. Hofmann, L. Wittwer, G. Heimel, and E. Zojer. "Self-Assembled Monolayers of Polar Molecules on Au(111) Surfaces: Distributing the Dipoles". *Physical Chemistry Chemical Physics* **12**, 4291 (2010) (see pp. 2, 3).
22. B. Kretz, D. A. Egger, and E. Zojer. "A Toolbox for Controlling the Energetics and Localization of Electronic States in Self-Assembled Organic Monolayers". *Advanced Science* **2**, 1400016 (2015) (see pp. 2, 3).
23. A. Kovalchuk, T. Abu-Husein, D. Fracasso, D. A. Egger, E. Zojer, M. Zharnikov, A. Terfort, and R. C. Chiechi. "Transition Voltages Respond to Synthetic Reorientation of Embedded Dipoles in Self-Assembled Monolayers". *Chem. Sci.* **7**, 781 (2016) (see p. 2).

24. X. Crispin. "Interface Dipole at Organic/Metal Interfaces and Organic Solar Cells". *Solar Energy Materials and Solar Cells* **83**, 147 (2-3 2004) (see p. 2).
25. B. H. Hamadani, D. A. Corley, J. W. Ciszek, J. M. Tour, and D. Natelson. "Controlling Charge Injection in Organic Field-Effect Transistors Using Self-Assembled Monolayers". *Nano Letters* **6**, 1303 (2006) (see p. 2).
26. C. Bock, D. V. Pham, U. Kunze, D. Käfer, G. Witte, and C. Wöll. "Improved Morphology and Charge Carrier Injection in Pentacene Field-Effect Transistors with Thiol-Treated Electrodes". *Journal of Applied Physics* **100**, 114517 (2006) (see p. 2).
27. M. Salinas, C. M. Jäger, A. Y. Amin, P. O. Dral, T. Meyer-Friedrichsen, A. Hirsch, T. Clark, and M. Halik. "The Relationship between Threshold Voltage and Dipolar Character of Self-Assembled Monolayers in Organic Thin-Film Transistors". *Journal of the American Chemical Society* **134**, 12648 (2012) (see p. 2).
28. M. Halik, H. Klauk, U. Zschieschang, G. Schmid, C. Dehm, M. Schütz, S. Maisch, F. Effenberger, M. Brunnbauer, and F. Stellacci. "Low-Voltage Organic Transistors with an Amorphous Molecular Gate Dielectric". *Nature* **431**, 963 (21, 2004) (see p. 2).
29. H. Klauk, U. Zschieschang, J. Pflaum, and M. Halik. "Ultralow-Power Organic Complementary Circuits". *Nature* **445**, 745 (15, 2007) (see p. 2).
30. E. C. P. Smits, S. G. J. Mathijssen, P. A. van Hal, S. Setayesh, T. C. T. Geuns, K. A. H. A. Mutsaers, E. Cantatore, H. J. Wondergem, O. Werzer, R. Resel, M. Kemerink, S. Kirchmeyer, A. M. Muzafarov, S. A. Ponomarenko, B. de Boer, P. W. M. Blom, and D. M. de Leeuw. "Bottom-up Organic Integrated Circuits". *Nature* **455**, 956 (16, 2008) (see p. 2).
31. L. Srisombat, A. C. Jamison, and T. R. Lee. "Stability: A Key Issue for Self-Assembled Monolayers on Gold as Thin-Film Coatings and Nanoparticle Protectants". *Colloids and Surfaces A: Physicochemical and Engineering Aspects* **390**, 1 (1-3 2011) (see p. 2).
32. P. M. Mendes. "Stimuli-Responsive Surfaces for Bio-Applications". *Chemical Society Reviews* **37**, 2512 (2008) (see p. 2).
33. D. G. Wu, D. Cahen, P. Graf, R. Naaman, A. Nitzan, and D. Shvarts. "Direct Detection of Low-Concentration NO in Physiological Solutions by a New GaAs-Based Sensor". *Chemistry-A European Journal* **7**, 1743 (2001) (see p. 2).
34. G. Ashkenasy, D. Cahen, R. Cohen, A. Shanzer, and A. Vilan. "Molecular Engineering of Semiconductor Surfaces and Devices". *Accounts of Chemical Research* **35**, 121 (2002) (see p. 2).
35. N. Ballav, S. Schilp, and M. Zharnikov. "Electron-Beam Chemical Lithography with Aliphatic Self-Assembled Monolayers". *Angewandte Chemie International Edition* **47**, 1421 (8, 2008) (see p. 2).

36. J. Adams, G. Tizazu, S. Janusz, S. R. J. Brueck, G. P. Lopez, and G. J. Leggett. "Large-Area Nanopatterning of Self-Assembled Monolayers of Alkanethiolates by Interferometric Lithography". *Langmuir* **26**, 13600 (17, 2010) (see p. 2).
37. O. El Zubir, I. Barlow, G. J. Leggett, and N. H. Williams. "Fabrication of Molecular Nanopatterns at Aluminium Oxide Surfaces by Nanoshaving of Self-Assembled Monolayers of Alkylphosphonates". *Nanoscale* **5**, 11125 (2013) (see p. 2).
38. B. D. Ratner and D. G. Castner. *Surface Analysis: The Principal Techniques* (ed J. C. Vickerman) 457 pp. (John Wiley, New York, 1997) (see pp. 2, 50).
39. S. Hüfner. *Photoelectron Spectroscopy Principles and Applications* (Springer Berlin Heidelberg, Berlin, Heidelberg, 2003) (see p. 2).
40. M. Zharnikov. "High-Resolution X-Ray Photoelectron Spectroscopy in Studies of Self-Assembled Organic Monolayers". *Journal of Electron Spectroscopy and Related Phenomena* **178-179**, 380 (2010) (see p. 2).
41. T. Abu-Husein, S. Schuster, D. A. Egger, M. Kind, T. Santowski, A. Wiesner, R. Chiechi, E. Zojer, A. Terfort, and M. Zharnikov. "The Effects of Embedded Dipoles in Aromatic Self-Assembled Monolayers". *Advanced Functional Materials* **25**, 3943 (2015) (see p. 3).
42. H. Ahn, M. Zharnikov, and J. E. Whitten. "Abnormal Pinning of the Fermi and Vacuum Levels in Monomolecular Self-Assembled Films". *Chemical Physics Letters* **428**, 283 (4-6 2006) (see p. 3).
43. Y. Ge, T. Weidner, H. Ahn, J. E. Whitten, and M. Zharnikov. "Energy Level Pinning in Self-Assembled Alkanethiol Monolayers". *The Journal of Physical Chemistry C* **113**, 4575 (19, 2009) (see p. 3).
44. N. V. Venkataraman, S. Zürcher, A. Rossi, S. Lee, N. Naujoks, and N. D. Spencer. "Spatial Tuning of the Metal Work Function by Means of Alkanethiol and Fluorinated Alkanethiol Gradients". *The Journal of Physical Chemistry C* **113**, 5620 (9, 2009) (see p. 3).
45. P. S. Bagus, G. Pacchioni, C. Sousa, T. Minerva, and F. Parmigiani. "Chemical Shifts of the Core-Level Binding Energies for the Alkaline-Earth Oxides". *Chemical physics letters* **196**, 641 (1992) (see pp. 3, 35).
46. P. S. Bagus, E. S. Ilton, and C. J. Nelin. "The Interpretation of XPS Spectra: Insights into Materials Properties". *Surface Science Reports* **68**, 273 (2013) (see pp. 3, 11, 13).
47. A. Natan, L. Kronik, H. Haick, and R. T. Tung. "Electrostatic Properties of Ideal and Non-Ideal Polar Organic Monolayers: Implications for Electronic Devices". *Advanced Materials* **19**, 4103 (3, 2007) (see pp. 3, 13, 14).
48. G. Heimel, F. Rissner, and E. Zojer. "Modeling the Electronic Properties of π -Conjugated Self-Assembled Monolayers". *Advanced Materials* **22**, 2494 (22, 2010) (see pp. 3, 15).

49. O. L. A. Monti. “Understanding Interfacial Electronic Structure and Charge Transfer: An Electrostatic Perspective”. *The Journal of Physical Chemistry Letters* **3**, 2342 (6, 2012) (see p. 3).
50. D. Cahen, R. Naaman, and Z. Vager. “The Cooperative Molecular Field Effect”. *Advanced Functional Materials* **15**, 1571 (2005) (see p. 3).
51. A. Natan, Y. Zidon, Y. Shapira, and L. Kronik. “Cooperative Effects and Dipole Formation at Semiconductor and Self-Assembled-Monolayer Interfaces”. *Physical Review B* **73**, 193310 (18, 2006) (see p. 3).
52. T. C. Taucher, I. Hehn, O. T. Hofmann, M. Zharnikov, and E. Zojer. “Understanding Chemical versus Electrostatic Shifts in X-Ray Photoelectron Spectra of Organic Self-Assembled Monolayers”. *The Journal of Physical Chemistry C* **120**, 3428 (18, 2016) (see pp. 3, 17, 31, 36, 49, 50).
53. H. Lu, D. Zeysing, M. Kind, A. Terfort, and M. Zharnikov. “Structure of Self-Assembled Monolayers of Partially Fluorinated Alkanethiols with a Fluorocarbon Part of Variable Length on Gold Substrate”. *The Journal of Physical Chemistry C* **117**, 18967 (19, 2013) (see pp. 3, 26–29, 36, 43, 45, 47).
54. R. G. Parr. *Density-Functional Theory of Atoms and Molecules* OCLC: 908078652 (Oxford University Press, USA, Oxford, 1989) (see p. 4).
55. F. Jensen. *Introduction to Computational Chemistry* 2nd ed. OCLC: ocm70707839. 599 pp. (John Wiley & Sons, Chichester, England ; Hoboken, NJ, 2007) (see p. 4).
56. R. M. Martin. *Electronic Structure: Basic Theory and Practical Methods* 1st pbk. ed. with corrections. 624 pp. (Cambridge University Press, Cambridge, UK ; New York, 2008) (see p. 4).
57. M. Born and R. Oppenheimer. “Zur Quantentheorie Der Molekeln”. *Annalen der Physik* **389**, 457 (1927) (see p. 4).
58. W. Pauli. *Exclusion Principle and Quantum Mechanics* (Springer, 1994) (see pp. 5, 7).
59. P. Hohenberg and W. Kohn. “Inhomogeneous Electron Gas”. *Physical Review* **136**, B864 (3B 9, 1964) (see p. 5).
60. L. H. Thomas. “The Calculation of Atomic Fields”. *Mathematical Proceedings of the Cambridge Philosophical Society* **23**, 542 (05 1927) (see p. 5).
61. E. Fermi. “Un Metodo Statistico per La Determinazione Di Alcune Priorieta Dell’atome”. *Rend. Accad. Naz. Lincei* **6**, 32 (602-607 1927) (see p. 5).
62. W. Ritz. “Über Eine Neue Methode Zur Lösung Gewisser Variationsprobleme Der Mathematischen Physik.” *Journal für die reine und angewandte Mathematik (Crelle’s Journal)* **1909**, 1 (1909) (see p. 6).
63. J. C. Slater. “The Theory of Complex Spectra”. *Physical Review* **34**, 1293 (15, 1929) (see p. 7).
64. R. O. Jones and O. Gunnarsson. “The Density Functional Formalism, Its Applications and Prospects”. *Reviews of Modern Physics* **61**, 689 (1, 1989) (see pp. 7, 12).

65. J. P. Perdew, K. Burke, and M. Ernzerhof. “Generalized Gradient Approximation Made Simple”. *Physical Review Letters* **77**, 3865 (28, 1996) (see p. 7).
66. P. Ziesche, S. Kurth, and J. P. Perdew. “Density Functionals from LDA to GGA”. *Computational Materials Science* **11**, 122 (1998) (see p. 8).
67. J. Hafner. “Ab-Initio Simulations of Materials Using VASP: Density-Functional Theory and beyond”. *Journal of Computational Chemistry* **29**, 2044 (2008) (see p. 8).
68. A. D. Becke. “A New Mixing of Hartree–Fock and Local Density-Functional Theories”. *The Journal of Chemical Physics* **98**, 1372 (1993) (see p. 8).
69. J. P. Perdew, M. Ernzerhof, and K. Burke. “Rationale for Mixing Exact Exchange with Density Functional Approximations”. *The Journal of Chemical Physics* **105**, 9982 (1996) (see p. 8).
70. R. M. Martin. *Electronic Structure: Basic Theory and Practical Methods* (Cambridge university press, 2004) (see pp. 8, 9).
71. H. J. Monkhorst and J. D. Pack. “Special Points for Brillouin-Zone Integrations”. *Phys. Rev. B* **13**, 5188 (1976) (see p. 9).
72. P. E. Blöchl. “Projector Augmented-Wave Method”. *Physical Review B* **50**, 17953 (15, 1994) (see p. 10).
73. G. Kresse and D. Joubert. “From Ultrasoft Pseudopotentials to the Projector Augmented-Wave Method”. *Physical Review B* **59**, 1758 (15, 1999) (see p. 10).
74. W. Kohn and L. J. Sham. “Self-Consistent Equations Including Exchange and Correlation Effects”. *Physical Review* **140**, A1133 (4A 15, 1965) (see p. 10).
75. E. J. Baerends, O. V. Gritsenko, and R. van Meer. “The Kohn–Sham Gap, the Fundamental Gap and the Optical Gap: The Physical Meaning of Occupied and Virtual Kohn–Sham Orbital Energies”. *Physical Chemistry Chemical Physics* **15**, 16408 (2013) (see p. 11).
76. N. Pueyo Bellafont, P. S. Bagus, and F. Illas. “Prediction of Core Level Binding Energies in Density Functional Theory: Rigorous Definition of Initial and Final State Contributions and Implications on the Physical Meaning of Kohn-Sham Energies”. *The Journal of Chemical Physics* **142**, 214102 (7, 2015) (see p. 11).
77. R. Stowasser and R. Hoffmann. “What Do the Kohn-Sham Orbitals and Eigenvalues Mean?” *Journal of the American Chemical Society* **121**, 3414 (1999) (see p. 11).
78. N. Pueyo Bellafont, F. Illas, and P. S. Bagus. “Validation of Koopmans’ Theorem for Density Functional Theory Binding Energies”. *Phys. Chem. Chem. Phys.* **17**, 4015 (2015) (see p. 11).
79. C.-O. Almbladh and U. von Barth. “Exact Results for the Charge and Spin Densities, Exchange-Correlation Potentials, and Density-Functional Eigenvalues”. *Physical Review B* **31**, 3231 (15, 1985) (see p. 11).

80. T. Koopmans. “Über die Zuordnung von Wellenfunktionen und Eigenwerten zu den Einzelnen Elektronen Eines Atoms”. *Physica* **1**, 104 (1-6 1934) (see p. 11).
81. J. F. Janak. “Proof That $\partial E / \partial N_i = \mu$ in Density-Functional Theory”. *Physical Review B* **18**, 7165 (15, 1978) (see p. 11).
82. M. M. Valiev and G. W. Fernando. “Occupation Numbers in Density-Functional Calculations”. *Physical Review B* **52**, 10697 (15, 1995) (see p. 12).
83. C. Göransson, W. Olovsson, and I. A. Abrikosov. “Numerical Investigation of the Validity of the Slater-Janak Transition-State Model in Metallic Systems”. *Physical Review B* **72**. doi:10.1103/PhysRevB.72.134203. (19, 2005) (see pp. 12, 13).
84. M. Methfessel, V. Fiorentini, and S. Oppo. “Connection between Charge Transfer and Alloying Core-Level Shifts Based on Density-Functional Calculations”. *Physical Review B* **61**, 5229 (15, 2000) (see pp. 12, 35).
85. M. V. Ganduglia-Pirovano, M. Scheffler, A. Baraldi, S. Lizzit, G. Comelli, G. Paolucci, and R. Rosei. “Oxygen-Induced Rh 3 D 5 / 2 Surface Core-Level Shifts on Rh(111)”. *Physical Review B* **63**. doi:10.1103/PhysRevB.63.205415. (1, 2001) (see p. 12).
86. L. Köhler and G. Kresse. “Density Functional Study of CO on Rh(111)”. *Physical Review B* **70**, 165405 (11, 2004) (see p. 13).
87. J. C. Slater. *Quantum Theory of Molecules and Solids. Vol. 4* (McGraw-Hill, 1974) (see p. 13).
88. M. Methfessel, D. Hennig, and M. Scheffler. “Ab-Initio Calculations of the Initial- and Final-State Effects on the Surface Core-Level Shift of Transition Metals”. *Surface Science* **287-288**, 785 (1993) (see p. 13).
89. E. Pehlke and M. Scheffler. “Evidence for Site-Sensitive Screening of Core Holes at the Si and Ge (001) Surface”. *Physical Review Letters* **71**, 2338 (4, 1993) (see p. 13).
90. S. Lizzit, A. Baraldi, A. Groso, K. Reuter, M. V. Ganduglia-Pirovano, C. Stampfl, M. Scheffler, M. Stichler, C. Keller, W. Wurth, and D. Menzel. “Surface Core-Level Shifts of Clean and Oxygen-Covered Ru(0001)”. *Physical Review B* **63**. doi:10.1103/PhysRevB.63.205419. (3, 2001) (see p. 13).
91. V. Blum, R. Gehrke, F. Hanke, P. Havu, V. Havu, X. Ren, K. Reuter, and M. Scheffler. “Ab Initio Molecular Simulations with Numeric Atom-Centered Orbitals”. *Computer Physics Communications* **180**, 2175 (2009) (see p. 17).
92. T. Bučko, J. Hafner, and J. G. Ángyán. “Geometry Optimization of Periodic Systems Using Internal Coordinates”. *The Journal of Chemical Physics* **122**, 124508 (2005) (see p. 18).
93. T. H. Fischer and J. Almlof. “General Methods for Geometry and Wave Function Optimization”. *The Journal of Physical Chemistry* **96**, 9768 (1992) (see p. 18).

94. E. Wruß. *Influence of van Der Waals Interactions on the Adsorption of Flatlying Organic Molecules on Metallic Surfaces* Master Thesis (Graz University of Technology, Graz, 2014). 139 pp. (see p. 19).
95. P. Haas, F. Tran, and P. Blaha. "Calculation of the Lattice Constant of Solids with Semilocal Functionals". *Physical Review B* **79**. doi:10.1103/PhysRevB.79.085104. (10, 2009) (see p. 21).
96. T. Hayashi and M. Hara. "Nonfouling Self-Assembled Monolayers: Mechanisms Underlying Protein and Cell Resistance". *Current Physical Chemistry* **1**, 90 (1, 2011) (see p. 23).
97. Y. Li, D. Lu, and G. Galli. "Calculation of Quasi-Particle Energies of Aromatic Self-Assembled Monolayers on Au(111)". *Journal of Chemical Theory and Computation* **5**, 881 (14, 2009) (see p. 23).
98. D. A. Egger, Z.-F. Liu, J. B. Neaton, and L. Kronik. "Reliable Energy Level Alignment at Physisorbed Molecule–Metal Interfaces from Density Functional Theory". *Nano Letters* **15**, 2448 (8, 2015) (see p. 23).
99. J. Pitha and R. N. Jones. "A Comparison of Optimization Methods for Fitting Curves to Infrared Band Envelops". *Canadian Journal of Chemistry* **44**, 3031 (15, 1966) (see p. 24).
100. J. Olivero and R. Longbothum. "Empirical Fits to the Voigt Line Width: A Brief Review". *Journal of Quantitative Spectroscopy and Radiative Transfer* **17**, 233 (1977) (see p. 24).
101. C. L. Lamont and J. Wilkes. "Attenuation Length of Electrons in Self-Assembled Monolayers of N-Alkanethiols on Gold". *Langmuir* **15**, 2037 (1999) (see p. 25).
102. J. Hwang, E.-G. Kim, J. Liu, J.-L. Brédas, A. Duggal, and A. Kahn. "Photoelectron Spectroscopic Study of the Electronic Band Structure of Polyfluorene and Fluorene-Arylamine Copolymers at Interfaces". *The Journal of Physical Chemistry C* **111**, 1378 (2007) (see p. 27).
103. N. Ballav, A. Terfort, and M. Zharnikov. "Mixing of Nonsubstituted and Partly Fluorinated Alkanethiols in a Binary Self-Assembled Monolayer". *The Journal of Physical Chemistry C* **113**, 3697 (5, 2009) (see p. 32).
104. J. Vackář, M. Hyt'ha, and A. Šimůnek. "All-Electron Pseudopotentials". *Physical Review B* **58**, 12712 (15, 1998) (see p. 35).
105. Y. Morikawa, T. Hayashi, C. C. Liew, and H. Nozoye. "First-Principles Theoretical Study of Alkylthiolate Adsorption on Au (111)". *Surface science* **507**, 46 (2002) (see p. 35).
106. C. A. Alves and M. D. Porter. "Atomic Force Microscopic Characterization of a Fluorinated Alkanethiolate Monolayer at Gold and Correlations to Electrochemical and Infrared Reflection Spectroscopic Structural Descriptions". *Langmuir* **9**, 3507 (1993) (see p. 36).

107. G.-y. Liu, P. Fenter, C. E. D. Chidsey, D. F. Ogletree, P. Eisenberger, and M. Salmeron. "An Unexpected Packing of Fluorinated N-Alkane Thiols on Au(111): A Combined Atomic Force Microscopy and X-Ray Diffraction Study". *The Journal of Chemical Physics* **101**, 4301 (1994) (see p. 36).
108. K. Tamada, J. Nagasawa, F. Nakanishi, K. Abe, M. Hara, W. Knoll, T. Ishida, H. Fukushima, S. Miyashita, T. Usui, T. Koini, and T. R. Lee. "Structure of SAMs Generated from Functionalized Thiols on Gold". *Thin Solid Films* **327-329**, 150 (1998) (see p. 36).
109. K. Tamada, T. Ishida, W. Knoll, H. Fukushima, R. Colorado, M. Graupe, O. E. Shmakova, and T. R. Lee. "Molecular Packing of Semifluorinated Alkanethiol Self-Assembled Monolayers on Gold: Influence of Alkyl Spacer Length". *Langmuir* **17**, 1913 (2001) (see p. 36).
110. *Private Conversations*. in collab. with E. Zojer. 2014 (see p. 37).
111. S. Bahn and K. Jacobsen. "An Object-Oriented Scripting Interface to a Legacy Electronic Structure Code". *Computing in Science & Engineering* **4**, 56 (May-June/2002) (see pp. 38, 72).
112. C. Van Oss, D. Absolom, and A. Neumann. "Applications of Net Repulsive van Der Waals Forces between Different Particles, Macromolecules, or Biological Cells in Liquids". *Colloids and Surfaces* **1**, 45 (1980) (see p. 45).
113. V. G. Ruiz, W. Liu, E. Zojer, M. Scheffler, and A. Tkatchenko. "Density-Functional Theory with Screened van Der Waals Interactions for the Modeling of Hybrid Inorganic-Organic Systems". *Physical Review Letters* **108**, 146103 (6, 2012) (see p. 45).
114. A. Tkatchenko and M. Scheffler. "Accurate Molecular Van Der Waals Interactions from Ground-State Electron Density and Free-Atom Reference Data". *Physical Review Letters* **102**. doi:10.1103/PhysRevLett.102.073005. (20, 2009) (see p. 45).
115. O. Anatole von Lilienfeld and A. Tkatchenko. "Two- and Three-Body Interatomic Dispersion Energy Contributions to Binding in Molecules and Solids". *The Journal of Chemical Physics* **132**, 234109 (2010) (see p. 45).
116. E. M. Lifshitz. "The Theory of Molecular Attractive Forces between Solids". *Soviet Physics J. Exper. Theoret. Phys.* **2**, 73 (1956) (see p. 45).
117. E. Zaremba and W. Kohn. "Van Der Waals Interaction between an Atom and a Solid Surface". *Physical Review B* **13**, 2270 (15, 1976) (see p. 45).
118. W. A. Al-Saidi, V. K. Voora, and K. D. Jordan. "An Assessment of the vdW-TS Method for Extended Systems". *Journal of Chemical Theory and Computation* **8**, 1503 (10, 2012) (see p. 45).
119. D. M. Alloway, M. Hofmann, D. L. Smith, N. E. Gruhn, A. L. Graham, R. Colorado, V. H. Wycsocki, T. R. Lee, P. A. Lee, and N. R. Armstrong. "Interface Dipoles Arising from Self-Assembled Monolayers on Gold: UV-Photoemission Studies of Alkanethiols and Partially Fluorinated Alkanethiols". *The Journal of Physical Chemistry B* **107**, 11690 (2003) (see p. 49).

120. A. Stukowski. “Visualization and Analysis of Atomistic Simulation Data with **OVITO—the Open Visualization Tool**”. *Modelling and Simulation in Materials Science and Engineering* **18**, 015012 (1, 2010) (see p. 72).
121. K. Momma and F. Izumi. “**VESTA 3 for Three-Dimensional Visualization of Crystal, Volumetric and Morphology Data**”. *Journal of Applied Crystallography* **44**, 1272 (1, 2011) (see p. 72).